Limits on the masses of supersymmetric particles from the UA1 experiment at the CERN ~~proton-antiproton~~ $p\bar{p}$ collider

Afzal Khan

Imperial College
London

A thesis submitted to the University of London
for the degree of Doctor of Philosophy

ABSTRACT

An analysis is presented of a data sample with large missing transverse energy, recorded at the CERN proton-antiproton collider. The data were collected at the UA1 experiment and correspond to an integrated luminosity of 715 nb^{-1}. A description of the Monte-Carlo calculations is given, for processes contributing to this large E_T^{miss} data sample. The very good agreement between the data and the simulated Standard Model physics processes is then used to set mass limits on the existence of the supersymmetric partners of the intermediate vector bosons, quarks and gluons - with the assumption of a massless lightest supersymmetric particle(taken to be a photino).

Variation of the mass limits with a massive photino is also investigated.

ACKNOWLEDGEMENTS

Before I embark upon the impossible task of recognising all those who have contributed to the fabric of my existence as a postgraduate student, I must apologise to them , who, partly through the exigencies of space and mostly through the deficiency of my recollection, have remained unmentioned. I doubt, however, if such neglect should cause them too much uneasiness of mind.

I should like to give thanks to the Science and Engineering Research Council for the financial support with which I have been provided.

Many thanks are due to Dave Binnie for allowing me to join the HEP group and for providing the opportunity to spend a most fruitful time at CERN. To Jim Virdee, whose tenacious assiduity was surpassed only by his effusive criticism, I doff the proverbial hat. Without him the inclination of the path may have been more sorely felt. I should also like to express my unbounded gratitude to Chris Seez, who through a combination of eccentric humour and unquestionable competence, created an atmosphere not lacking of spice. His help with that of Tony Wildish, in the early days, was vital. My thanks go to Dave Robinson for his tranquillity, to Christos Markou for his companionship, to Roger Forty for revealing to me the possibility of a future in squash, to Lucas Taylor for his help with some histograms, to Steve Macmahon for providing me with the opportunity to lose his key and to Shaun Roe for sharing in the masochism of excessive physical exercise. I thank also Alan Watson, Marco Cattaneo, Gary Taylor, Julian Shulman, Sylvie Dugaey, James Gillies, Rob Edgecock, Nav Bains and Dave Francis for their camaraderie.

I am grateful to Steve Haywood for sharing with me the last bus and to Dave Charlton for rendering it unnecessary to take an axe to the machine.

I am indebted to Mohammad Mohammadi, Felicitas Pauss and Richard Batley, whose help with the missing energy analysis was invaluable.

Special thanks are due to Linda Jones, in whose foot I have been a constant thorn. Perhaps it was the use of this afflicted appendage that caused her to miss the penalty, which was as unlikely an event as the rising of the sun in the middle of the night, and thereby ensure that we achieved national notoriety by losing everything yet again. Thanks also to Betty Moynihan for fussing over the inexorable increase of entropy in my office, To Jim Gibb for ensuring that the greater part of humanity is acquainted with the 'rubber king' anecdote, to Diane, to Ash and also to Jane Ratcliffe for enduring when most had fallen by the wayside(part-timers). I thank, also, John Hassard for checking the spelling.

To Jeremy Dodd I express my gratitude for being such a work of art and for showing me that something does turn up. I thank Miles Blencowe for making the effort to descend, occasionally, into our four dimensions.

I thank Leslie Marshall for being an affectionate friend to me and quite probably to the rest of the world, Mike Huricane for giving me an appreciation of speed and Maria for possessing a caustic wit.

Davie Norman, that one-man show, is surely above appreciation. Watching him pursue a ball to the boundary is truly a sight to behold (beheld all to often, I may add, when playing for CERN). My thanks to Julian and Sian for providing the most delightful society and to Steve Hancock, to whom my advice must surely be to stay on the front foot.

Finally, I have the greatest pleasure to express my eternal gratitude to Alison Fowler, the gang and to my mother, Gulzar Begum. Without their love, support and unqualified commitment, the flowers would not blossom, the birds would not sing, the sun would not shine and, discord would reign supreme.

London
September 1989.

To my mother and the loving memory of my dear father.

CONTENTS

CHAPTER 1

THEORETICAL INTRODUCTION

1.1 INTRODUCTION

The current theoretical description of the physical world, which is often referred to as the Standard Model [14], has been very successful in its description of nearly all available data pertaining to the strong, weak and electromagnetic phenomena, and as yet there is no evidence of behaviour that violates this scheme. The Standard Model does not, however, represent a complete unified theory of all the interactions in nature. There are theoretical and aesthetic arguments which suggest that an extension of the Standard Model will be needed.

Supersymmetry is a recent theoretical idea which represents a potentially significant addition to our current understanding of the physical world. It offers many promising avenues in the attempt to construct a unified field theory of physics and alleviates some of the shortcomings of the Standard Model.

This chapter contains a brief history of particle physics and a qualitative description of the Standard Model. It ends with a discussion of the theoretical motivation for and the phenomenology of, supersymmetry.

1.2 STANDARD MODEL

The eighteenth century saw the maturation of classical mechanics, and the advent of the theory of classical electromagnetism. This was followed early in the twentieth century by two major new conceptual frameworks, quantum mechanics and relativity theory. These were brought together in 1928 by Dirac [15] and together with Maxwell's theory of electromagnetism, represent a body of knowledge sufficient to understand the interactions of atoms and molecules, which form the basis for all chemistry and ultimately biology. During the 1940's theorists such as Schwinger, Feynman and Tomonaga [16] created a complete quantum field theory of electrodynamics, QED. The central mathematical idea was that of a lagrangian, which together with Hamilton's least action principle yields the field equations of motion (from the Euler-Lagrange equations).

By the 1940's the existence of the four forces of nature, gravitation, electromagnetism, weak and strong, was known. These four forces are still considered fundamental today, although a connection between the weak and the electromagnetic forces has now been recognised. The 1940's also saw the set of known particles increase from the simple set of five known in the 1930's , i.e. protons, neutrons, electrons, photons and neutrinos. The proton, neutron and electron are known to be constituents of atoms, while the photon is known to transmit the electromagnetic force. The neutrinos, which are closely connected with radioactive decays via the weak force, were first predicted by Pauli. The discovery of two new particles, known as the muon and the pion, was a cause of great excitement. Yukawa had already predicted that the strong force was mediated by the exchange of a particle with the same characteristics as the pion. The muon appeared to be just a heavier version of the electron.

The 1950's and the 1960's saw an explosion of new particle discoveries in cosmic ray experiments at first and then in accelerators such as cyclotrons and synchrotrons. New quantum numbers like strangeness, which is now known to be carried by a new flavour of quark, were discovered during this period. In this period also, symmetry came to assume an important role in particle physics. The role of symmetry in quantum mechanics was fully formalised in the 1959 work of Wigner [17]. Soon after, Gell-Mann and Ne'eman proposed a symmetry scheme for the classification of baryons and mesons; the eight-fold way [18]. The eight-fold way served as a basis for the quark model, which was independently proposed by Zweig and Gell-Mann in the mid-1960's [19].

By the late 1970's gauge symmetry became a central underpinning to the understanding of the physical world. The great success of this idea is represented in the work of Glashow, Weinberg and Salam [20], for which they were awarded the nobel prize. Their work incorporated the weak force into a gauge theory, resulting in the unification of the electromagnetic and weak forces into the electroweak force. The discovery of neutral currents, in 1973, at CERN provided the initial experimental confirmation of this theory, followed later by parity violating experiments at SLAC, and culminating in the actual production and detection of the intermediate vector bosons, the W and the Z, at CERN's $Sp\bar{p}S$ facility [21].

The Standard Model was completed during the 1970's and the 1980's. Gauge symmetry now assumed its central role as the guiding principle for the form of particle interactions. The strong, weak and electromagnetic forces are embedded in an $SU(3)_C \times SU(2)_L \times U(1)_Y$ gauge group.

The theory of Quantum Chromodynamics (QCD) is the gauge theory of strong interactions, and is based on the SU(3) gauge group. The electromagnetic and the weak forces are embedded in a direct product of an $SU(2)_L$ weak isospin gauge group with a $U(1)_Y$ hypercharge gauge group. These gauge groups dictate the boson particle spectrum of the electroweak theory, with four spin 1 gauge bosons : γ, Z^0, $W^+$and W^- . These bosons are responsible for mediating the interactions between fermions. The non-Abelian nature of the $SU(3)_C$ and $SU(2)_L$ gauge groups implies that these bosons can have self interactions, unlike the photon. This is because the non-Abelian gauge bosons carry the same charge that they couple to, unlike Abelian gauge bosons such as the photon.

There is now overwhelming experimental evidence that hadrons are made from smaller particles called quarks. Historically, the idea of quarks dates back to the mid-1960's when Gell-Mann and Zweig proposed the underlying SU(3) symmetry whereby baryons are constructed from bound states of three quarks or antiquarks (qqq or $\bar{q}\bar{q}\bar{q}$) and mesons are made up from bound states of a quark and an antiquark ($q\bar{q}$). For example , the proton and the pion(π^+) are composed of the uud and $u\bar{d}$ bound states respectively, where u and d refer to the 'up' and the 'down' quark flavours. The additive quantum numbers of the quarks must match the conserved quantum numbers of the parent hadron, so the quarks have fractional charge (Q(u)=2/3, Q(d)=-1/3) and baryon number (B=1/3). Moreover, the hypothesis that quarks are fermions with J=1/2 accommodates the observed separation of hadrons into baryons (J=1/2 or 3/2 qqq fermion states) and mesons (J=0 or 1 $q\bar{q}$ boson states). However, the quark scheme ran into difficulties in the attempt to explain the Δ^{++} baryon, a uuu bound state, because the J=3/2 nature of the Δ^{++} forces the quark scheme to combine the three u quarks in a completely symmetric ground state, which is forbidden by Fermi-Dirac statistics. There did exist other discrepancies in the quark hypothesis: the quark scheme did not exclude bound states like qq or $q\bar{q}$, but these have never been observed by experiment. All these apparent discrepancies were resolved by the introduction of the new property called 'colour'. Each quarks comes in three colours, the primary colours. The Δ^{++} is then found to be a bound state of $u_R u_G u_B$, the three quarks are therefore distinguishable according to the rules of Fermi-Dirac statistics. The colour scheme excludes non-observed states like qq by asserting that all particles observable by experiment must be colourless or 'white'. Baryons are colourless because they contain a red, a blue and a green quark, and mesons carry both colour and anticolour.

The strong force is carried by eight gluons, which couple to particles that carry colour, such as the quarks. A consequence of the ability of gluons to interact with other gluons is that the colour lines between two quarks are squeezed into a tube-like shape (figure(1.1)). Separating the two quarks increases the strong coupling between them, and the potential energy between the two quarks will increase with separation. Quarks (and gluons) are therefore presumed to be confined, a phenomenon known as infra-red slavery. If two quarks are provided with sufficient energy to separate such that α_s, the strong coupling constant becomes large, the quarks can manifest themselves as experimentally observable sprays, or jets, of hadrons. This process can be seen in figure(1.2).

As the quarks separate, the increasing potential energy in the colour tube becomes sufficient to create a $q\bar{q}$ pair. The new $q\bar{q}$ pair effectively breaks the tube into two shorter tubes with a lower net energy. If there is sufficient energy, the colour lines are stretched further and more $q\bar{q}$ pairs are created . The net result is clusters of quarks and gluons, each with zero net colour, that can form jets of hadrons observable by experiment.

The strong force which acts between hadrons is seen to be a remnant of the strong force which is mediated by gluons. Because of confinement, coloured gluons cannot be exchanged over large distances between hadrons. Instead, colourless objects such as pions must be exchanged, and since these mesons are massive this remnant strong force is short ranged.

The weak force requires that fermions come in left-handed doublets, so that the left-handed electron and its neutrino belong to an isospin doublet. Since the right-handed electron is an isospin singlet it carries different quantum numbers than the left-handed electron. Therefore the left- and right-handed electrons have different couplings to the Z^0 . Similar statements apply to the muon and the tau particles. Quarks also come in left-handed doublets and right-handed singlets. Experimentally it has been observed that a quark doublet exists for every lepton doublet. The doublets are grouped together into what are called generations. There are three known generations (see figure(1.3)). Note, however, that the top quark has yet to be experimentally observed. Thus there are a total of 73 fundamental fields when all the degrees of freedom are counted. Even if nature only consisted of one generation there would still be 43 fundamental fields.

In this form the Standard Model has been tremendously successful. QED is the most accurate physical theory known; the weak bosons have been discovered and the quark model has been able to classify the vast number of meson and baryon states into a concise spectroscopy. The observation of two and three jet structure in hadronic events at both e^+e^- and $p\bar{p}$ colliders provides experimental evidence of the validity of QCD.

Despite all its accomplishments, the Standard Model is regarded as a stepping stone to a more complete theory of nature. It contains a large number of fields, many free parameters and does not predict the number of generations. The Standard Model also fails to unify all the four forces and the gravitational force does not yet have a successful quantum mechanical description. The Standard Model is therefore widely viewed as a low energy effective lagrangian of a more complete theory that is not yet known.

1.3 SUPERSYMMETRY

Supersymmetry is a very exciting new extension to the Standard Model. It postulates a symmetry between bosons and fermions, such that every ordinary boson has a supersymmetric fermionic partner, and every ordinary fermion has a supersymmetric bosonic partner. Supersymmetry was first formulated in 1971 by Y.A.Gelfand and E.P.Likhtman of the Lebedev Physical institute of Moscow [22]. It was independently developed in 1973 by D.V.Volkov and V.P.Akulov of the Physical institute in Kharkov [23]. The first Lagrangian displaying both supersymmetric and gauge invariance was published by J.Wess of Karlsruhe University, and B.Zumino of CERN in 1974 [24]. This work precipitated a more general interest in supersymmetry. In 1976, P.Fayet [25] presented the first model in which a realistic model of electroweak theory, incorporating the Higgs mechanism, was made supersymmetric.

The most frequently quoted motivations for supersymmetry are that it has fewer divergences, that it provides a possible mechanism for unifying gravity with the other interactions and thereby constructing a unified theory of everything (TOE). However, the only motivation for having light supersymmetric particles in an accessible mass range is as a solution to the naturalness or hierarchy problem [26]. This problem centres around the fact that radiative corrections to the masses of elementary scalar bosons, such as the Higgs boson of the Standard Model, are quadratically divergent,

$$\delta m_H^2 = O\left(\frac{\alpha}{\pi}\right)\Lambda^2 \qquad (1.1)$$

Where Λ is a loop momentum cut-off. It can be seen from equation (1.1) that if the physical mass of the Higgs is to be natural, i.e. $\delta m_H^2 \leq m_H^2$, where $m_H^2 \approx m_W^2$, Λ should be $\leq$ 1 Tev. However this problem is alleviated within supersymmetry by the fact that the quadratically divergent boson and fermion loop corrections to $m_H{}^2$ have opposite signs, and if bosons B and fermions F occur in pairs with identical couplings as in supersymmetry, these quadratically divergent corrections will cancel, leaving behind a residual

$$\delta m_H^2 = O(\frac{\alpha}{\pi}) \; | m_B^2 - m_F^2 | \qquad (1.2)$$

Therefore the role of the cut-off Λ in equation (1.1) is taken over by the boson-fermion mass difference. Then it follows that:

$$| m_B^2 - m_F^2 | \leq 1 \text{ TeV}/c^2 \qquad (1.3)$$

Hence one expects that the supersymmetric partners of the known particles should have masses less than about 1 TeV/c^2.

In supersymmetric theories the Lie algebra is extended to a graded Lie algebra i.e. with both commutation and anticommutation relations that connect the internal supersymmetry generators to the Poincare generators. In its simplest form the supersymmetric algebra has a self-conjugate spin-1/2 generator $Q\alpha$ with the property that it changes the total angular momentum by half a unit :

$$Q\alpha \; | \text{boson} > \; = \; | \text{fermion} >$$

$$Q\alpha \; | \text{fermion} > \; = \; | \text{boson} >$$

It changes boson fields to fermion fields and vice versa.

The supermultiplets of supersymmetry then contain particles of different spin as follows:

$$\begin{array}{cc} \text{chiral} & \text{gauge} \\ \begin{array}{c} f \\ \tilde{f} \end{array} \begin{pmatrix} \frac{1}{2} \\ 0 \end{pmatrix} & \begin{array}{c} g \\ \tilde{g} \end{array} \begin{pmatrix} 1 \\ \frac{1}{2} \end{pmatrix} \end{array}$$

In the spirit that all fundamental symmetries are local gauge symmetries, it is also possible to make supersymmetry local. A local supersymmetry is called supergravity (SUGRA).

Realistic models of supersymmetry, with a plethora of new phenomena, have been extensively developed in the last few years. The masses of the supersymmetric partners of the observed particles are unknown, and it has been found phenomenologically that no known particle can be the supersymmetric partner of any other known particle. Also, since m(fermion)=m(boson) is never observed in nature supersymmetry must be a broken symmetry. Therefore, the minimal supersymmetric extension of the Standard Model leads to a doubling of the number of fundamental fields, see table(1.1) . Note the Higgs sector has been enlarged to include two Higgs doublets. This is necessary since one Higgs doublet can only generate masses for down-like quarks, i.e. those with charge -1/3 e, without destroying supersymmetry. It should be pointed out that table(1.1) lists the particle spectrum before supersymmetry is broken. This means that the final mass eigenstates will in general involve mixing between the original weak eigenstates. Because such mixing involves details of the model used to generate symmetry breaking , few general statements can be made.

Most phenomenological models of supersymmetry introduce a new quantum number, R-parity, which is multiplicatively conserved. All ordinary particles have R=+1, while their superpartners have R=-1. It is possible to relate R-parity to other quantum numbers conserved in the Standard Model:

$$R = (-1)^{3B+3L+2S} \qquad (1.4)$$

Where B is baryon number, L is lepton number and S is spin.

R-parity conservation has several important phenomenological consequences :

(i) supersymmetric particles are always produced in pairs. Thus accelerator experiments must have energies large enough to be able to produce at least two superpartners.

(ii) Once a supersymmetric particle is created it always decays to another lighter supersymmetric particle.

(iii) The lightest supersymmetric particle (LSP) is absolutely stable, since it has no legal decay mode.

Since the LSP is absolutely stable, it should be present in large numbers in the universe today as a cosmological relic from the Big Bang. If the lightest superpartner were charged or had strong interactions, its relics would have condensed out into galaxies in the form of heavy isotopes. These have not been seen [27], thus it is assumed that the lightest supersymmetric particle has no electromagnetic or strong interactions. The LSP can therefore escape experimental detection in much the same way that a neutrino can. This means that the signal of supersymmetry will be missing transverse energy, resulting from the escaping photinos that are the ultimate decay products .

There are many neutral weakly interacting supersymmetric particles which are candidates for being the LSP. They include the sneutrinos, the shiggs, photino and the zino. In popular models the sneutrinos are rather heavy, hence the LSP is likely to be some $\tilde{H}$ / $\tilde{\gamma}$ / $\tilde{Z}$ mixture [28]. In the model used in this thesis, it is assumed that the LSP is an almost pure photino state.

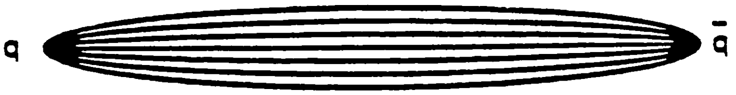

Figure (1.1) : *The field lines between two quarks.*

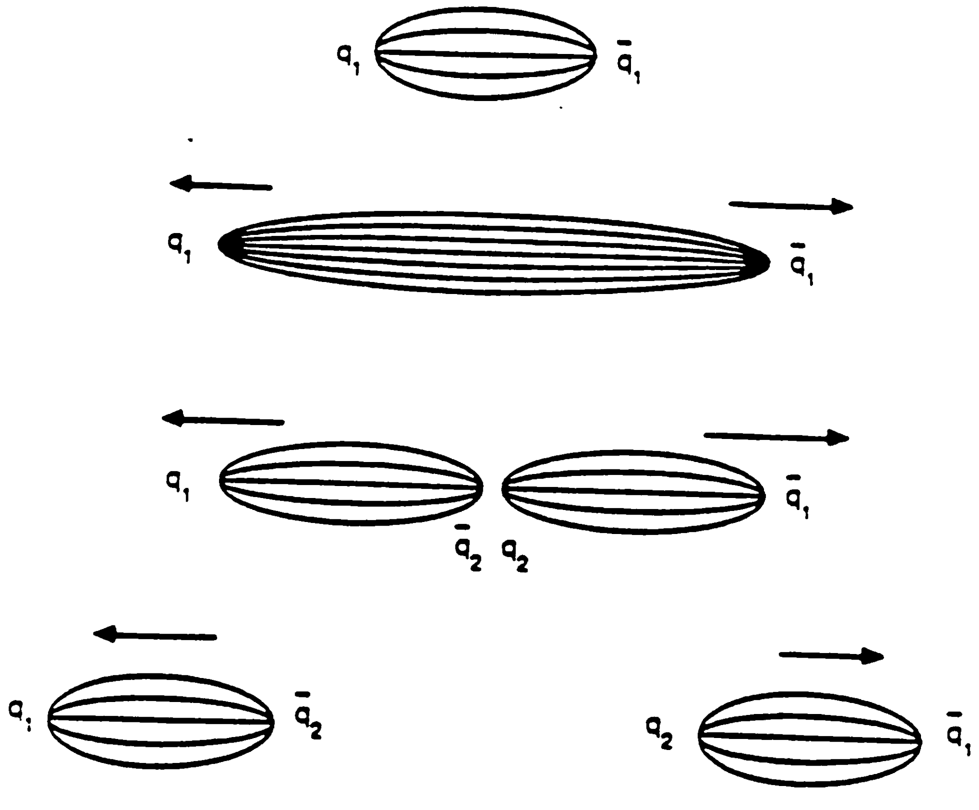

Figure (1.2) : *The quark confinement mechanism.*

$$\begin{array}{lcccccc} & \multicolumn{2}{c}{\text{Leptons}} & & \multicolumn{3}{c}{\text{Quarks}} \\ & (e)_R & \begin{pmatrix}\nu_e \\ e\end{pmatrix}_L & & (u_i)_R & (d'_i)_R & \begin{pmatrix}u_i \\ d'_i\end{pmatrix}_L \\ \text{Fermions} & (\mu)_R & \begin{pmatrix}\nu_\mu \\ \mu\end{pmatrix}_L & & (c_i)_R & (s'_i)_R & \begin{pmatrix}c_i \\ s'_i\end{pmatrix}_L \\ & (\tau)_R & \begin{pmatrix}\nu_\tau \\ \tau\end{pmatrix}_L & & (t_i)_R & (b'_i)_R & \begin{pmatrix}t_i \\ b'_i\end{pmatrix}_L \end{array}$$

	EM	Weak	Strong
Gauge Bosons	γ	Z° $W^\pm$	g_{ij}

Higgs Scalar H°

Generation	Quarks			Leptons		
	Type	Q	I^3	Type	Q	I^3
1	*u* (up) *d* (down)	+2/3 -1/3	+1/2 -1/2	ν_e e^-	0 -1	+1/2 -1/2
2	c (charm) s (strange)	+2/3 -1/3	+1/2 -1/2	ν_μ μ^-	0 -1	+1/2 -1/2
3	*t* (top)? *b* (bottom)	+2/3 -1/3	+1/2 -1/2	ν_τ τ^-	0 -1	+1/2 -1/2

Figure (1.3) : *The basic constituents of matter and the fundamental interactions.*

Particle		Spin	Supersymmetric Partner			Spin
quark	q	$\frac{1}{2}$	scalar-quark	$\tilde{q}_L$,	$\tilde{q}_R$	0
	u	$\frac{1}{2}$		$\tilde{u}_L$,	$\tilde{u}_R$	0
	d	$\frac{1}{2}$		$\tilde{d}_L$,	$\tilde{d}_R$	0
	$\vdots$			$\vdots$		
lepton	ℓ	$\frac{1}{2}$	scalar-lepton	$\tilde{\ell}_L$,	$\tilde{\ell}_R$	0
	e	$\frac{1}{2}$		$\tilde{e}_L$,	$\tilde{e}_R$	0
	μ	$\frac{1}{2}$		$\tilde{\mu}_L$,	$\tilde{\mu}_R$	0
	τ	$\frac{1}{2}$		$\tilde{\tau}_L$,	$\tilde{\tau}_R$	0
neutrino	ν_e	$\frac{1}{2}$	scalar-neutrino	$\tilde{\nu}_e$		0
	ν_μ	$\frac{1}{2}$		$\tilde{\nu}_\mu$		0
	ν_τ	$\frac{1}{2}$		$\tilde{\nu}_\tau$		0
gluon	g	1	gluino	$\tilde{g}$		$\frac{1}{2}$
photon	γ	1	photino	$\tilde{\gamma}$		$\frac{1}{2}$
Z	Z^o	1	Z-ino	$\tilde{Z}^o$		$\frac{1}{2}$
higgs	H_i^o	0	higgsino	$\tilde{H}_i^o$		$\frac{1}{2}$
W	$W^\pm$	1	W-ino	$\tilde{W}^\pm$		$\frac{1}{2}$
higgs	$H_i^\pm$	0	higgsino	$\tilde{H}_i^\pm$		$\frac{1}{2}$

Table (1.1) : *The particle spectrum of the minimal supersymmetric extension of the Standard Model. It should be noted that mass eigenstates will in general be mixtures of* $\tilde{\gamma}$, $\tilde{Z}^0$, $\tilde{H}_i^0$ *or of* $\tilde{W}^\pm$, $\tilde{H}_i^\pm$ *or of* $\tilde{q}_L$, $\tilde{q}_R$ *or of* $\tilde{l}_L$, $\tilde{l}_R$.

CHAPTER 2

EXPERIMENTAL INTRODUCTION

2.1 THE CERN PROTON-ANTIPROTON PROJECT

In the mid 1970s there already existed accelerators, both at CERN and at Fermilab in the US, that could accelerate protons up to energies of 450 GeV. But the high-energy protons from these machines are directed at stationary targets of nucleons, and much of the energy of the bombarding particles is used up in giving kinetic energy to particles of relatively low mass - protons, mesons etc. created in the collision. This reduces the amount of energy that can be used in the interaction between the high-energy particles and the nuclear constituents of the target - for creating new species of subatomic particle. However in head-on collisions between two particles that are both moving close to the speed of light, all the energy is available for the interaction. This principle had already been successfully implemented at CERN in the intersecting storage rings (ISR) - two interlaced rings of magnets which bring two oppositely directed beams of protons together at their cross-over points. But this meant essentially building two rings. An alternative and less expensive scheme was to accelerate particles of opposite electric charge in opposite directions, but in the same ring. This method has proved very successful with electrons and positrons, at laboratories at Hamburg, Cornell University and Stanford, California among others. A third still less expensive alternative was to convert a machine already used to accelerate one type of particle into one that collided oppositely directed beams.

At CERN the super proton synchrotron (SPS) uses magnetic fields to guide bunches of protons through a ring of tubing kept at an extremely good vacuum, to avoid unwanted collisions with stray air molecules. As the protons pass round the ring they pick up radio-frequency energy at specific points, gaining energy as they circulate but keeping the same path as the fields in the electromagnets around the ring are increased. Once the maximum energy for the machine is reached the protons are deflected along a tangential vacuum tube which guides the particles to experiments.

In 1976 Carlo Rubbia, David Cline, Peter McIntyre[29] suggested using the biggest available proton accelerators to accelerate antiprotons in the opposite direction. In this way one could achieve much higher collision energies than even CERN's ISR could produce, and at a fraction of the cost of a new accelerator.

Antiprotons have opposite electric charge (negative) to protons and so can travel in exactly the same path through magnetic fields as protons but in the opposite direction. So by sending bunches of antiprotons in the opposite direction to protons, one has a colliding-beam machine. Practically, however, this is not trivial. One of the main difficulties lies with ensuring that there will be sufficient collisions between protons and antiprotons to make the project worthwhile. Most of the particles will go straight past each other without colliding. Also, while protons are relatively easy to produce - by ionization of a hydrogen atom - antiprotons can be made only in high energy collisions of other particles. The usual technique is to direct a beam of protons from an accelerator to strike a target of Tungsten, for example, and to collect the antiprotons so created by using magnetic fields. Not many antiprotons are created in these collisions. A beam of 10^{13} protons with 26 GeV of energy creates only 2.5×10^7 antiprotons with an average energy of 3.5 GeV when it strikes a target of tungsten. However calculations reveal that to produce a useful number of interesting interactions in proton-antiproton collisions at the energy of the SPS one needs to collide bunches that each contain at least 10^{11} particles.

The rate at which interactions take place is measured by the luminosity, L:

$$\frac{dN}{dt} = L\,\sigma \qquad (2.1)$$

Where σ is the interaction cross-section for the process. In terms of the machine parameters (see table(2.1)) the luminosity is given by :

$$L = \frac{N_P N_{\bar{P}} f}{A} \qquad (2.2)$$

Where N_p and $N_{\bar{p}}$ are the numbers of protons and antiprotons per bunch; f is the bunch crossing frequency and A is the effective cross-sectional area of the beams. This area is reduced in the vicinity of UA1 by the use of quadrupole magnets. The lifetime of the beam is determined by beam-beam interactions and the scattering of beam particles by gas molecules within the beam pipe.

2.2 BEAM COOLING

The creation of enough antiparticles is not the only problem to be faced. On emerging from the target the antiprotons have a range of velocities. Viewed in their own reference frame the antiprotons form a gas, and their random motions are indicative of a temperature. If this temperature is too high some of the particles will strike the walls of the accelerator and the beam will be dissipated. Therefore some method is needed to 'cool' the antiproton beam, ie. to reduce its random motions, in order to keep it as concentrated as possible before it enters the accelerator ring.

One such beam-cooling technique, called electron cooling, operates by mixing a 'cool' beam of electrons (one in which all the particles have the same speed and direction) with the 'hot' antiproton beam for a short distance. In the process some of the random thermal energy of the antiprotons is transferred to the electrons. Mixing the antiproton beam repeatedly with fresh electron beams can cool the antiprotons significantly, provided their energy is not too high to start with. However the CERN scheme called for an antiproton beam whose energy was initially too high to be cooled effectively by this method. Another beam-cooling method, better suited to the requirements of the CERN proton-antiproton collider, was invented in 1968 by Simon van der Meer[1].

This method, called stochastic cooling (because it relies on a statistical process), utilizes a 'pickup', or sensing device, in one section of a storage ring to measure the average deviation of the particles from the ideal orbit. The measurement is converted into a correction signal, which is relayed across the ring to a 'Kicker' device on the other side. The Kicker applies an electric field to its section of the ring in time to nudge the centre of mass of the passing particles back toward the ideal orbit. Although the particles are moving very close to the speed of light, the correction signal can arrive in time because it takes the shorter path across a chord of the cooling ring.

At the CERN proton-antiproton collider the particles are directed through a complex sequence of interconnected beam-manipulating devices, see figure(2.1). First a beam of protons is accelerated to an energy of 26 GeV in the proton synchrotron(PS), the original accelerator ring at CERN, completed in 1959. The proton beam is then directed at a copper target producing a spray of particles, including a small fraction of antiprotons, with an average energy of 3.5 GeV. The antiprotons are collected and transferred to a wide aperture storage ring called the Antiproton Accumulator (AA), where they are first precooled by the stochastic method and then moved to a slightly smaller orbit, where they are stacked with the previously injected bunches and subjected to further cooling. After a few hundred billion antiprotons have been collected they are sent back to the PS ring, where they are accelerated to 26 GeV before being injected into the SPS. Meanwhile protons at 26 GeV from the PS ring are injected into the SPS ring in the opposite direction. The counterrotating beams are finally accelerated to 270 GeV each in the SPS ring. The beams collide at two interaction sites, where the detectors are placed, see figure(2.1).

2.3 PHYSICS ON UA1

The aim of the CERN proton-antiproton collider was to search for the W and the Z bosons. The first evidence for W production and subsequent decay came from the observation of electrons with large momenta transverse to the beam direction, accompanied by missing transverse energy [2]. The missing transverse energy was carried away by a neutrino, which cannot be detected directly, recoiling against the electron. The Z was identified by its decay to pairs of energetic high transverse momentum electrons [3]. Subsequently, the muonic decay modes were also seen [4], [3].

In addition to the discovery of the W and the Z, the UA1 Collaboration has produced work on :

- B-physics: in 1986, the UA1 Collaboration reported the first observation of B^0-$\overline{B}^0$ oscillations [5]

- Jet physics: for the first time, jets were unambiguously seen in the collisions of hadrons [6], and QCD has been extensively tested

- Missing transverse energy: in addition to significant missing transverse energy arising from decays of Ws to electrons and muons, the decays into tau leptons have also been seen [7].

  Further, the agreement between the data and the theoretical predictions for known contributions has enabled limits to be placed on other possible sources of missing transverse energy, see chapter 6.

- Top quark: while it is expected that there should be a sixth quark, to complete the three generations in the Standard Model (see chapter 1), there is at present no evidence for it, and UA1 has set limits on its mass [8].

2.4 MISSING TRANSVERSE ENERGY

An analysis of high-energy proton-antiproton interactions containing a large amount of missing transverse energy, owing to the production of one or more energetic neutrinos or new weakly interacting neutral particles, can extend our understanding of the Standard Model(see chapter 1), and is a sensitive way to search for new phenomena such as supersymmetry.

In the Standard Model of electroweak interactions, high transverse momentum prompt neutrinos are produced in the leptonic decays of W and Z bosons (eg. $W \rightarrow e\bar{\nu}$ or $Z \rightarrow \nu\bar{\nu}$) and in the semileptonic decays of heavy quarks (eg. $b \rightarrow ce\bar{\nu}$). A summary of the missing transverse energy event topologies expected from these standard sources is shown in figure(2.2).

We shall be interested, in this thesis, in events in which a large missing transverse energy is produced in association with one (monojet) or more (multijet) hadronic jets, and in which the missing transverse energy is isolated, ie. well separated from the jets. The isolation requirement is necessary to remove the large background due to jet events (with no genuine missing transverse energy) in which the finite detector resolution leads to an apparent missing transverse energy aligned with one of the jets in the event, see figure(1.2). Isolated missing transverse energy events containing an electron or muon are dominated by $W \rightarrow e\nu$[9] and $W \rightarrow \mu\nu$[10] decays. These events have been well studied at the CERN $p\bar{p}$ collider and will be considered as background. The dominant sources of isolated missing energy plus jet events are expected to be (i) the decay of a W into a τ lepton with subsequent hadronic decay of the τ:

$$p\bar{p} \rightarrow W + X,$$
$$W \rightarrow \tau\,\nu \rightarrow \text{hadrons} + \nu\,\nu$$

and (ii) the production of a high transverse momentum Z^0 recoiling against a quark or gluon jet followed by the decay of the Z^0 into two neutrinos:

$$p\bar{p} \rightarrow Z^0 + \text{jet} + X,$$
$$Z^0 \rightarrow \nu\,\nu$$

The observation [11] of six monojet events in an earlier analysis of UA1 data from the 1983 collider run stimulated intense interest in missing transverse energy as a signal for new physics such as additional generations of quarks and leptons[12] and supersymmetry[13]. A fourth generation of quarks and leptons, for example, would contain a charged heavy lepton L which, if light enough, could be produced in decays of the W:

$$
\begin{aligned}
p\bar{p} &\to W + X, \\
&\quad W \to L\nu_l, \\
&\qquad\quad L \to q\,q\,\nu_l
\end{aligned}
$$

giving rise to events with missing transverse energy and one or more jets. Similarly, the rate of events from the process $p\bar{p} \to Z^0 + X$, $(Z^0 \to \nu\nu)$ discussed above is proportional to the number of light neutrinos coupling to the Z^0, and the missing transverse energy events can therefore be used to constrain the total number of generations allowed in the Standard Model.

Supersymmetric models contain a rich spectrum of new particles(see chapter 1). Associated with each quark, lepton, gauge boson, or Higgs boson of the Standard Model is a new particle differing by 1/2 unit of spin. In most models, the lightest supersymmetric particle (often the photino, the partner of the photon) has a small interaction cross-section and will consequently escape detection, ie. will produce missing transverse energy. We will be able to set lower limits on the masses of some of these supersymmetric particles.

AA stacking rate	7×10^9 P h^{-1}
Transfer efficiency	75%
N_p	2×10^{11}
$N_{\bar{p}}$	2×10^{10}
Max initial L	5×10^{29} cm^{-2} s^{-1}
Lifetime (luminosity)	24 h
Gas pressure at UA1	10^{-8} Pa

Table(2.1): *Approximate values for the parameters of the SPS*

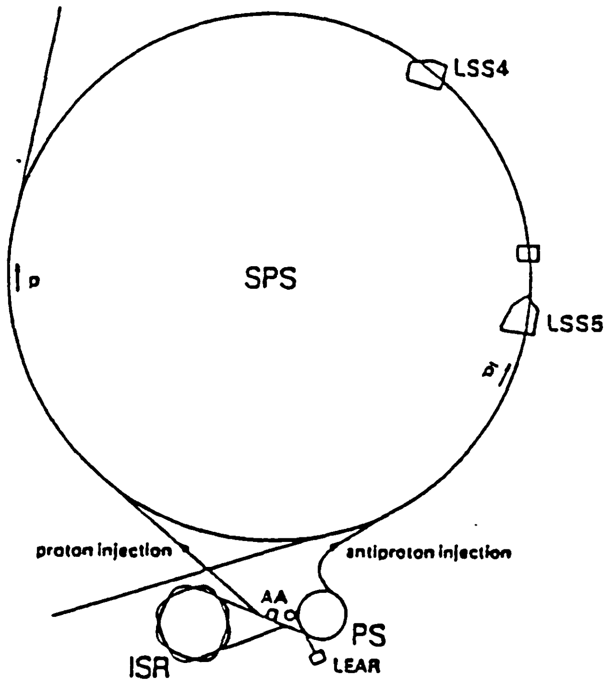

Figure (2.1): *Top view of the CERN proton-antiproton accelerator complex.*

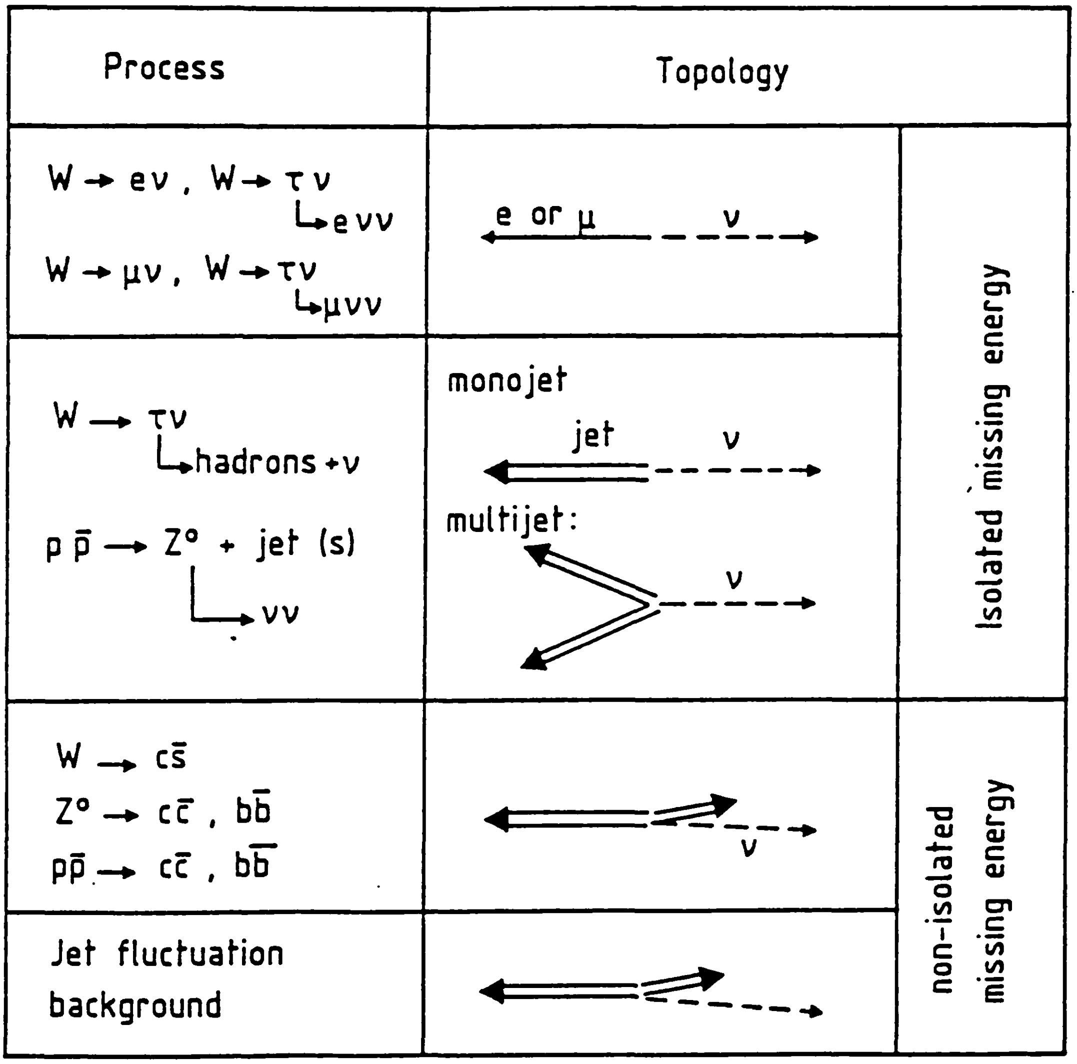

Figure (2.2) : *Schematic representation of the topologies of large transverse energy events expected from Standard Model processes and from jet-fluctuation background.*

CHAPTER 3

THE UA1 APPARATUS

3.1 INTRODUCTION

In 1976 Rubbia, McIntyre and Cline [29] proposed a scheme to increase the energy of the CERN super proton synchrotron (SPS) by converting it into a colliding beam machine. The proposal for the UA1 experiment was presented in 1978 [30] among another series of proposals [31]. It was the most complete and largest detector, situated on one of the straight sections of the SPS ring (see figure(2.1)). The apparatus was installed twenty metres below ground. Part of the testing and construction of the detector was carried out at the location while other parts were built at participating laboratories. During the construction, the SPS was still accelerating protons for fixed target experiments. In addition the SPS had to be kept operational for machine development, since turning it into a collider had to be achieved in parallel with the construction of the new experiments. This led to the design of removable shielding between the SPS tunnel and the so-called 'Garage' where the detector was assembled. Apart from a shut-down period in order to perform the excavations needed, the new developments did not disturb the scientific program of CERN too much. Cabling, gas connections etc. were designed in such a way that the detector could be operational in both the garage and the SPS-ring. The complete apparatus is on a rail system so that it can be moved between the two locations. Figure(3.1) gives an artist's view of the opened detector, while figure(3.2) shows a cross-section along the beam.

The almost 4π solid angle coverage (polar angle from the beam direction $\theta=0.2^{\circ}$) of the apparatus makes it possible to 'detect' escaping particles. Non-interacting particles will leave an imbalance in the energy measured after the full event is reconstructed ('missing energy'). By this method, for example, the transverse momentum of the neutrino from the semi-leptonic decay of the W can be determined.

The Beam crossings in the SPS tunnel occur at intervals of 7.6 μs, whereas data can only be written to tape at a few events per second. This means that a reliable trigger needs to be included in the data acquisition, which can give an on-line decision of the importance of an event and either reject or record the whole event.

In the following sections we will briefly discuss the main features of the apparatus. Starting from the interaction region in the very centre of the detector, the measurement of the momenta of charged particles is achieved by the 'central detector (CD)', which will be described in section(3.2). Section(3.3) contains a description of the 'electromagnetic calorimeter', situated just outside the CD. It absorbs electrons, photons etc. and measures the energy deposited by these particles. The energy of all the hadrons (Kaons etc.) that are not completely stopped by the material of the electromagnetic calorimeter is measured by the 'hadronic calorimeter' (section(3.4)). A 'minimum ionizing' muon will pass all this material provided it has sufficiently large energy. It will be detected in 'muon chambers', at the very outside of the apparatus. Between the muon chambers and the Hadron calorimeter there is additional shielding against high energy hadrons that leak through the calorimeters. This drastically decreases the probability of mis-identification of a charged hadron in the muon chambers. The muon chambers are described in section(3.5). There is a combination of image chambers, electromagnetic and hadronic calorimeters along the beam pipe on either side of the central portion of the detector, providing further coverage of the solid angle. These instruments are collectively referred to as the 'forward detector' and will be briefly described in section(3.6) . The remaining sections discuss the trigger, Data acquisition and Reconstruction. The UA1 coordinates and angles are defined in figure(3.3).

3.2 THE CENTRAL DETECTOR

The central detector (CD) [32] is a large cylindrical drift chamber, see figure(3.4). Six half-cylindrical chambers form a large cylinder 6m long and 2.2m in diameter, filled with a mixture of 40% Argon and 60% Ethane at atmospheric pressure. It is a multi-wire drift chamber consisting of alternating anode and cathode planes aligned parallel to the z direction, immersed in a uniform horizontal magnetic field of 0.7 Tesla.The sense wires in each anode plane are in two layers separated by field shaping wires, to avoid ambiguities in the drift direction.

On passing through the CD, charged particles liberate electrons from the argon which then drift in the electric field towards the sense wires. Close to the wires the gradient increases significantly and the drifting electrons will further ionize the gas, giving rise to an avalanche effect, providing multiplication of the signal. For further detail see ref[33]. The charge collected in this way is read-out and the signal is amplified. Since the magnetic field is oriented parallel to the wires the charged particles are only bent in the xy plane.

Measurement of the drift time, charge on and position of the wire provide an excellent position determination in the xy plane. The position along the wire is obtained by charge division. For this the sense wire is read-out at both ends. The relative amount of charge seen at the two ends provides the position of the track along the wire. The drift volumes are constructed in such a way that a maximum drift time of 3.5μs is achieved, which is less than the 3.8 μs bunch crossing interval when the collider is operating with the maximum of six proton and six anti-proton bunches.

The momentum of a track in the CD is found from its measured curvature according to the formula:

$$p = \frac{0.3\,Q\,B\,R}{\cos\lambda} \qquad (3.1)$$

Where P is the momentum (GeV/c), Q the charge (units of electrostatic charge), B the magnetic field (Tesla), R the radius of curvature in the bending plane (m) and λ the angle of the track out of the plane perpendicular to the field. The momentum resolution is therefore related to the position resolution of points on the track. Typically the error on the momentum is:

$$\frac{\Delta p}{p} = 0.005\,p \qquad (3.2)$$

(P in GeV/c), but it is dependent on the track length and track orientation in the chambers.

3.3 THE ELECTROMAGNETIC CALORIMETERS

Identification of electrons and photons is the main task of the electromagnetic calorimeters, which completely enclose the CD. Figure(3.5) contains a diagram of two sections of the so-called 'gondolas' [34], the central part of the electromagnetic calorimeters. The gondolas are on either side of the CD. Each module covers the azimuthal angle of ~180^0, while the width along the beam direction corresponds to ~0.1 units of rapidity. The complete central part of this calorimeter is formed from 48 units, 24 on each side. The inner diameter is 2.72 metres, while the total length amounts to 6 metres ($25^0 \leq \theta \leq 155^0$), and covers a pseudorapidity range of $|\eta|$=1.5. These calorimeters are sampling detectors, a dense material(Lead) is used to generate the electromagnetic shower and a transparent scintillating medium (plastic scintillator) samples the shower.

Photons and electrons originating from the interaction vertex (and electromagnetically interacting), will give rise to electromagnetic showers in the calorimeter. Ultra-Violet light produced in the scintillator material by the ionizing particles of the shower, is converted to blue light by a fluorescing chemical. This blue light, which has a longer attenuation length, travels into a bar or sheet of acrylic doped with a wavelength shifting chemical (BBQ). The BBQ absorbs the blue light and re-emits it in the green part of the spectrum. The green light travels along the bar by internal reflection into conventional light guides and then to the photomultiplier tubes (PMs).

Each gondola is made from of layers of 1.2 mm thick lead sandwiched by 1.5 mm thick scintillator sheets. The shower is sampled at four depths corresponding to 3.3, 6.6, 9.9 and 6.6 radiation lengths (at normal incidence). Each scintillator section is read-out by four photomultipliers. Thus in total, sixteen phototubes are attached to one gondola, eight at the top and eight at the bottom side. An electron or photon can then traverse a minimum of 26.3 radiation lengths (1.1 interaction lengths). This will under normal circumstances ensure that the electromagnetic shower generated by a photon or an electron is completely absorbed. In this way the energy profile over the four samplings provides information about the nature of the particle.

The behaviour and energy resolution of the gondolas have been studied in detail in beam tests.

The energy dependent resolution for electrons can be parametrized as follows:

$$\frac{\sigma(E)}{E}=\frac{0.15}{\sqrt{E}} \qquad (3.3)$$

with E in GeV.

The x-coordinate of the shower is roughly determined by the narrow width of the gondola. However by using the relative intensities of the four PMs of the sampling, one can measure x with a resolution:

$$\sigma(x)=\frac{0.063}{\sqrt{E}} \quad (m) \qquad (3.4)$$

with E in GeV.

This method of light-division is also used to determine the ϕ coordinate (azimuth about the x axis). The angular resolution, defined in the plane perpendicular to the beam (y-z), reads:

$$\sigma(\phi)=\frac{0.24}{\sqrt{E}} \quad \text{radians} \qquad (3.5)$$

E in GeV.

The disadvantage of this technique is that only an 'average shower position' can be determined in the case when two or more particles hit the same gondola cell. similar problems occur when the shower in an adjacent cell gives rise to leakage. However, in many cases the charged tracks measured in the CD can resolve ambiguities.

The 'bouchons', the end-caps of the electromagnetic calorimeter are positioned at about 3m on either side of the interaction region. They cover the angular range of $5^0 < \theta < 25^0$ and $155^0 < \theta < 175^0$, thus extending calorimetry coverage out to pseudorapidities of 3.

A cross-section of the bouchons is given in figure(3.6) sixteen sectors (petals) of lead-scintillator form a complete end-cap with an inner radius of 30 cm and an outer radius of 150 cm. The read-out is done at four samplings at the following depths: 3.6, 7.2, 8.7 and 7.2 radiation lengths (measured perpendicular to the petal), representing 26.7 radiation lengths (1.1 interaction lengths) in total.

Without going into further detail, the energy deposition is measured with a single phototube, while a separate position detector [35] locates the centre of the shower with a precision of 2 mm in space.

The resolution of the transverse energy (E_T=ESinθ) becomes (E_T in GeV):

$$\frac{\sigma(E_T)}{E_T} = \frac{0.12}{\sqrt{E_T}} \qquad (3.6)$$

3.4 THE HADRON CALORIMETERS

The electromagnetic calorimeters are surrounded by the hadron calorimeters[36]. The so-called 'C-modules' cover the gondolas, while the 'I-modules' are placed behind the bouchons. Figure(3.7) shows a C-module.

A magnet coil is sandwiched between the gondolas and the hadron calorimeter. The hadron calorimeter also acts as the magnet return yoke. The central part of this calorimeter is built out of sixteen of these rectangular C-shaped modules, eight on each side of the beam line. Each C-module is azimuthally segmented into 12 cells (both the Is and Cs are made of iron/scintillator sandwiches), with 5 cm of iron and 1 cm of scintillator for each sandwich. The read-out is again via BBQ wavelength shifter bars and light guides. Each cell is sampled at two roughly equal sections in depth, each about 2.5 interaction lengths thick. Two PMs view each sampling.

The end-cap hadron calorimeters, the Is, are similar to the Cs excepting that they are somewhat thicker and consequently can handle the higher particle energies in this region.

There are six I-modules at each end of the detector, see figure(3.8). Each I-module is divided into six cells, whereas the modules closest to the beam are again sub-divided into four smaller cells. Except for the difference in interaction lengths (3.5), the read-out of the Is is similar to that of the Cs.

The total absorption length of the gondolas plus the C-modules is 6.1 at normal incidence. The bouchons plus the Is add up to 9.6 absorption lengths.

The energy resolution of the hadron calorimeters is, with E in GeV:

$$\frac{\sigma(E)}{E} = \frac{0.80}{\sqrt{E}} \qquad (3.7)$$

Usually hadronic showers are completely contained in the active volume of these calorimeters. Only energetic muons(and neutrinos) can penetrate them. Thus these calorimeters effectively shield the muon chambers. There is, however, some hadron punch-through (leakage), which is a background to the muon detector signals and degrades the resolution of the hadron calorimeters.

3.5 THE MUON CHAMBERS

These are modular drift chambers constructed from aluminium drift tubes [37]. They form the outermost part of the UA1 detector and cover about on average 70% of the solid angle. They surround the hadron calorimeters on all sides. A muon passing through the calorimeters and the additional iron shielding reaches the muon chambers only if its momentum is greater than 2.5 GeV/c. It leaves a track in the CD, energy corresponding to a minimum ionizing particle in both calorimeters and a track in the muon chambers.

There are 12, 12 and 4 modules (each consisting of two chambers) in the forward, side and top regions respectively. Each chamber has tubes in both transverse directions. In the bottom region, because of space limitations, there are tubes parallel to the z direction only. Figure(3.9) shows a section of a muon chamber. These detectors were not used in this analysis.

3.6 THE FORWARD DETECTORS

These comprise the electromagnetic calorimeters, hadronic calorimeters and Image chambers in the forward regions to cover pseudorapidities greater than 3.

The forward calorimeters are important for the missing energy analysis. They are used to complete the total energy measurement of events and thereby veto backgrounds such as double interactions, which normally have a total energy larger than the centre of mass of the beams. The calorimeters are made of two sets of detectors known as the forward (or Calcom) and the very forward calorimeters. The Calcoms are in fact the compensating magnets (to compensate the effect of the UA1 magnetic field on the beams) instrumented to be used as calorimeters. The Calcom and the very forward calorimeters are of similar construction and read-out as the central calorimeters. They extend the calorimeter coverage to 6 units of pseudorapidity.

3.7 THE TRIGGER

Beam crossings occur at 1.3×10^5 Hz in the UA1 detector, while interactions occur at a rate which is an order of magnitude lower, depending on the actual luminosity. For a luminosity of 0.1 $\mu b^{-1} s^{-1}$ the interaction rate is about 5 KHz. The UA1 trigger was designed to reduce this rate by three orders of magnitude to about 5 Hz.

It is essential that the event rate is reduced because (i) the speed of the tape drives that record the events onto magnetic tape, for analysis, is limited to about 4 or 5 events per second, and (ii) most of the interactions are not sufficiently interesting to record.

The triggering system must decide which events to keep and to do so very fast ie. within 3.8 μs between beam crossings. This means that for its first level decision only calorimeter and some muon chamber information is available to the trigger.

The UA1 trigger [38] is made up of three parts: (i) the pretrigger, (ii) the calorimeter trigger, and (iii) the muon trigger.

The pretrigger consists of scintillation hodoscopes on both ends of the detector, covering angles extending down to 0.6^0 from the beam direction. For normal data taking, the pretrigger selects an event when at least one particle hit is recorded in any hodoscope element at each end of the detector. The hits must be consistent in time with a particle going outwards from the interaction point. Satisfying the pretrigger conditions is a prerequisite for all other triggers.

The calorimeter trigger adds all the individual signals from any cell to form a total signal for that cell. The results from neighbouring cells are then combined. These signals are then compared with look-up tables which allow for the pedestal and the geometric position of the corresponding cells when finding the transverse energy. Events can be selected on the basis of topology (e.g. two electromagnetic clusters on opposite sides of the detector), location of energy deposition (e.g. central or forward), nature of energy (electromagnetic or hadronic), and amount of energy (e.g. greater than a predetermined value). Any combination of these conditions can be used to form a calorimeter trigger to select a certain kind of event. Up to 24 (12 for the 1983 run) distinct types can be accepted simultaneously.

It is a very versatile trigger but has the time limit of 3.8 μs to make a decision, so the trigger information comes from 8 bit ADCs having a digitization time of about 500 μs as opposed to those used for the calorimeters (14 bit LeCroy ADCs with digitization times in the order of 4 ms). Since the trigger ADCs sum over many phototubes, they have degraded position resolutions and energy measurements compared to the measurements from the calorimeters.

The missing E_T trigger is an example of a calorimeter trigger, and is formed in the following way : The scalar sum of the transverse energy (E_T) is calculated from all calorimeter cells in the left half of the detector ($|E_T|_L$) and from all cells in the right half of the detector ($|E_T|_R$). If the difference $||E_T|_L - |E_T|_R|$ is greater than 17 GeV and there also exists a jets with E_T greater than 15 GeV, then the event is kept.

The muon trigger is based on information from the muon chambers, so the events should have muons with momentum greater than 2.5 GeV/c. It identifies candidate muon tracks in the muon detector. The trigger requires that candidate tracks point in the direction of the interaction point to within 150 mrads - this removes most of the cosmic rays, beam halo and low energy muons which are substantially deviated by multiple scattering. There must also be at least a minimum ionizing signal in the hadron calorimeter element through which the track must have passed.

The final trigger selection of an event is made by the final level logic unit. It analyzes the results of all triggers and accepts or rejects the event based on defined triggers of interest.

3.8 DATA ACQUISITION AND RECONSTRUCTION

On being selected by the trigger the read-out of the event begins. All signals from the various parts of the detector are digitized by units in CAMAC crates. The amount of digital data per event is typically 2 Mbytes. These data are then formatted by processors in the CAMAC crates to about 100 Kbytes per event and passed to the emulators. UA1 uses five emulators running in parallel. These execute Fortran code which performs a rapid and simple event reconstruction, using some CD information as well as the calorimeter and muon information, and perform the final on-line event selection. If the events are accepted they are written onto magnetic tapes.

During the run the selected raw data are written onto separate streams, normal tapes and express line tapes. The express line data set contains a copy of the events with special triggers selected by the emulators and is processed immediately during the run. This makes it possible to access interesting events such as W, Z or missing energy events for preliminary investigation. The processing of the express line data also helps to check the apparatus and can identify problems in the experiment within 24 hours of the data being written.

The reconstruction of the raw data, preformed off-line, proceeds in two steps. The first processing program (PREPRO) has three main functions: (i) it orders the data into HYDRA [39] format, a CERN memory management system; (ii) removes pedestals and applies calibration constants; (iii) removes the zeros from data channels which have not detected particles in the event.

The second stage is the reconstruction of the preprocessed data (BINGO), which essentially reconstructs the tracks through the whole detector. Final calibration of the measurements is applied and track finding in the drift chambers is preformed.

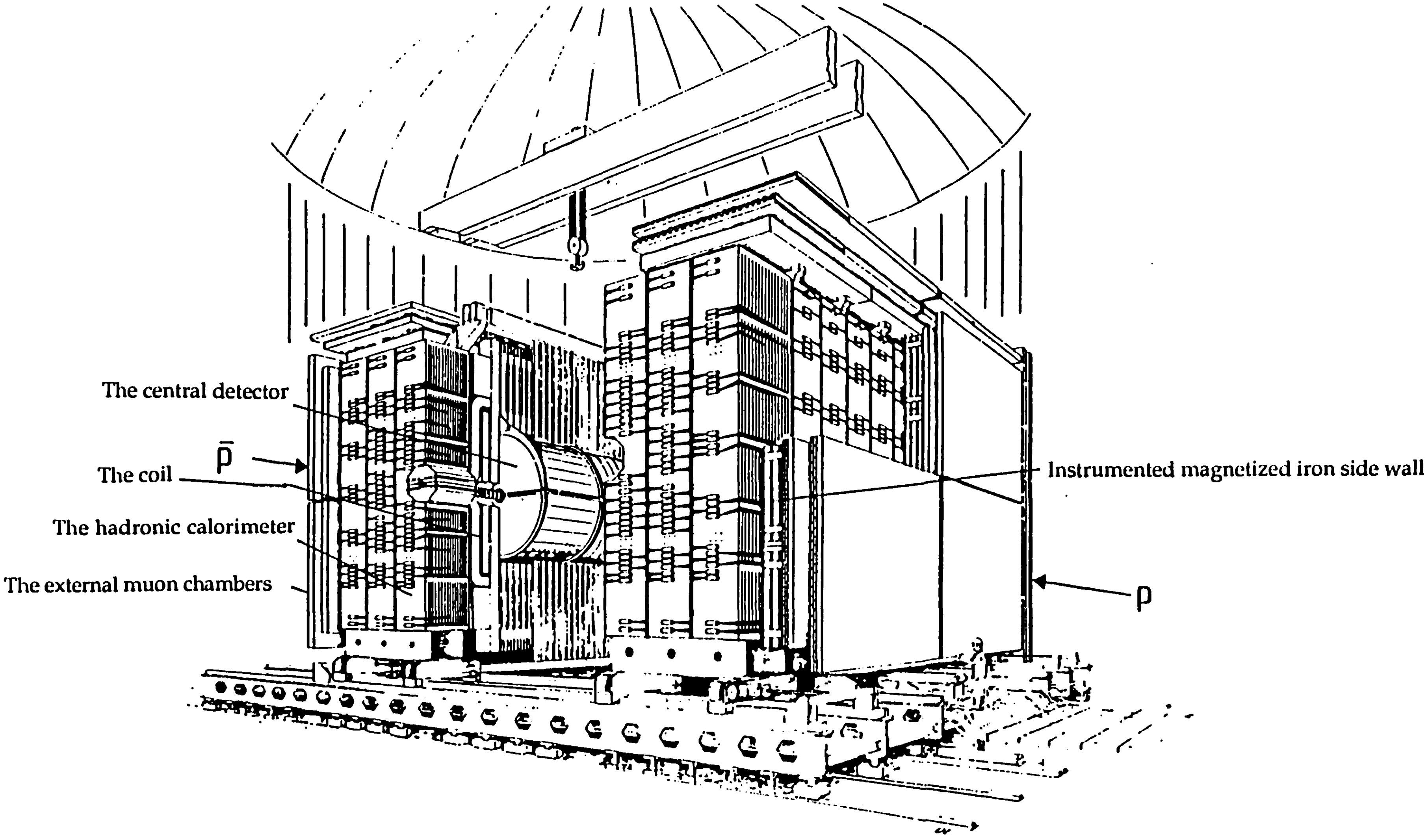

Figure (3.1) : *A general view of the UA1 experiment (the forward and very forward calorimeters are not shown). The two halves of the apparatus have been opened to show the CD.*

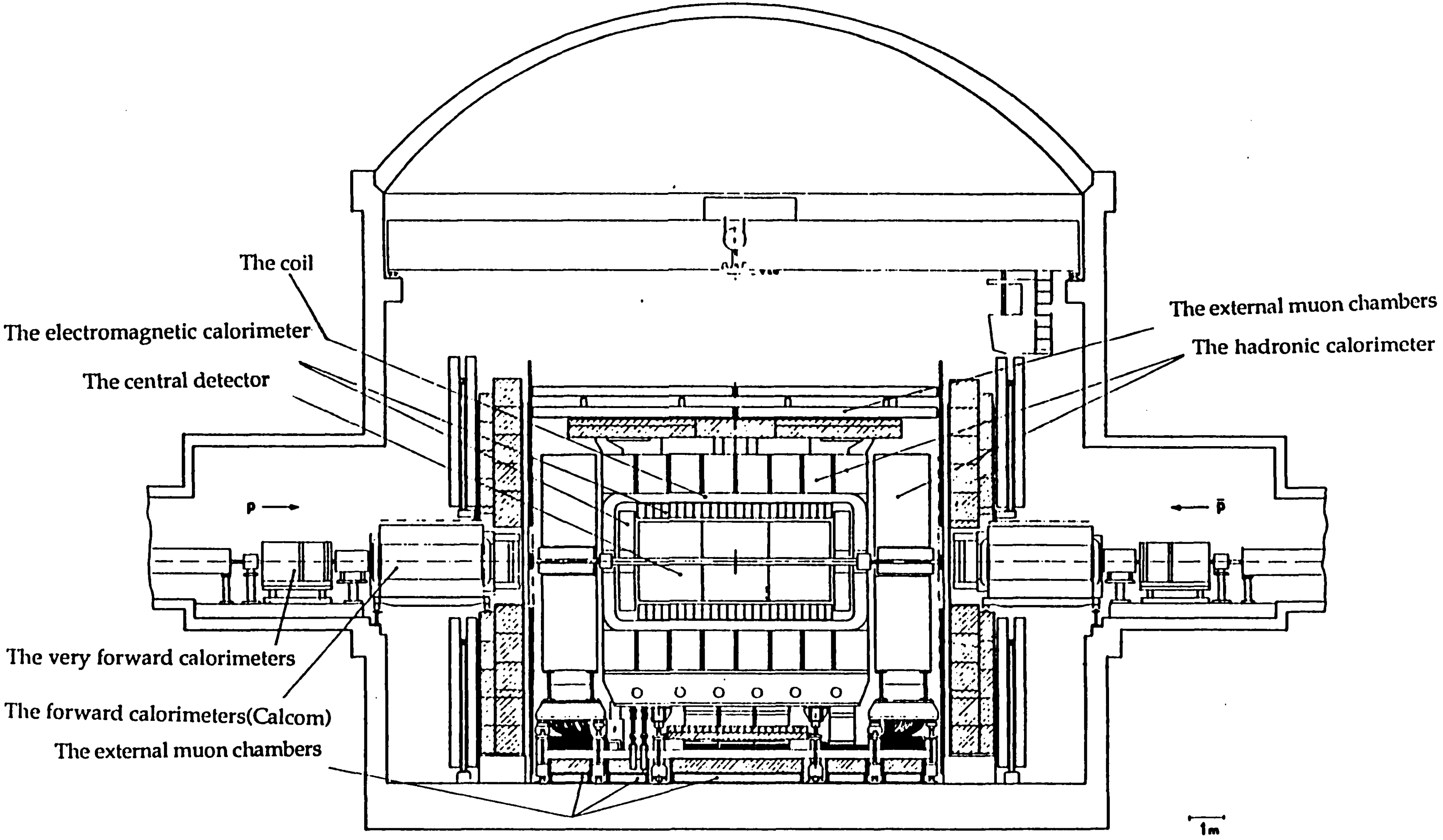

Figure (3.2) : *Cross-sectional view of the UA1 experiment along the beam.*

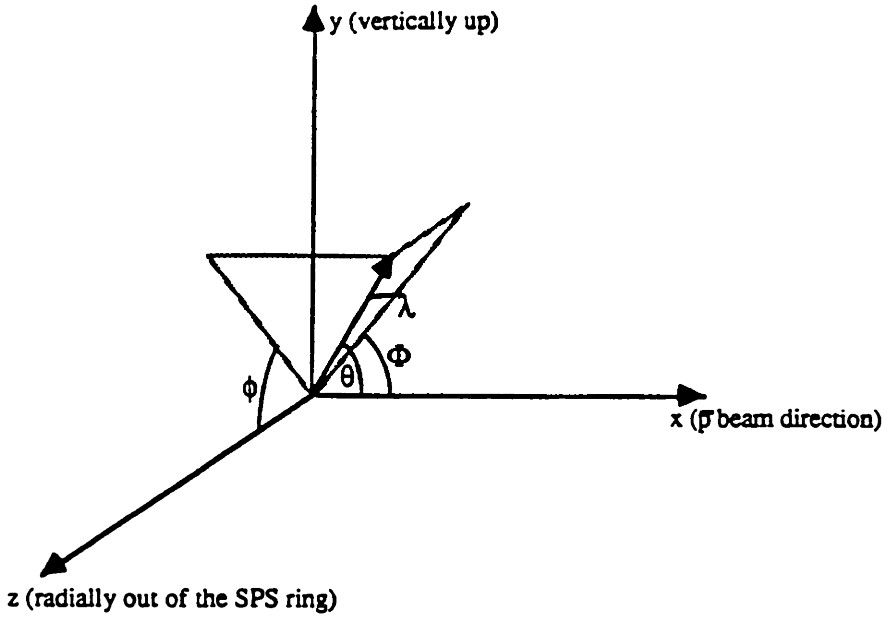

x — beam axis, $\bar{p}$ direction
y — vertically upwards
z — horizontally out of the SPS ring (B-field direction)
θ — polar angle from x-axis
ϕ — azimuthal angle around x-axis, +ve z-axis has $\phi = 0$
η — pseudorapidity : $\eta = -\ln(\tan(\theta/2))$
λ — dip angle out of the x-y plane, +ve z axis has $\lambda = \pi/2$
Φ — azimuthal angle around z-axis, +ve x-axis has $\Phi = 0$
(Φ is not used in this thesis, do not confuse with ϕ)

Note that 'transverse' always means transverse to the beam direction,
unless otherwise stated
(for example, p_t is defined by $p_t^2 = p_y^2 + p_z^2$)

Figure (3.3) : *The UA1 coordinates and angles.*

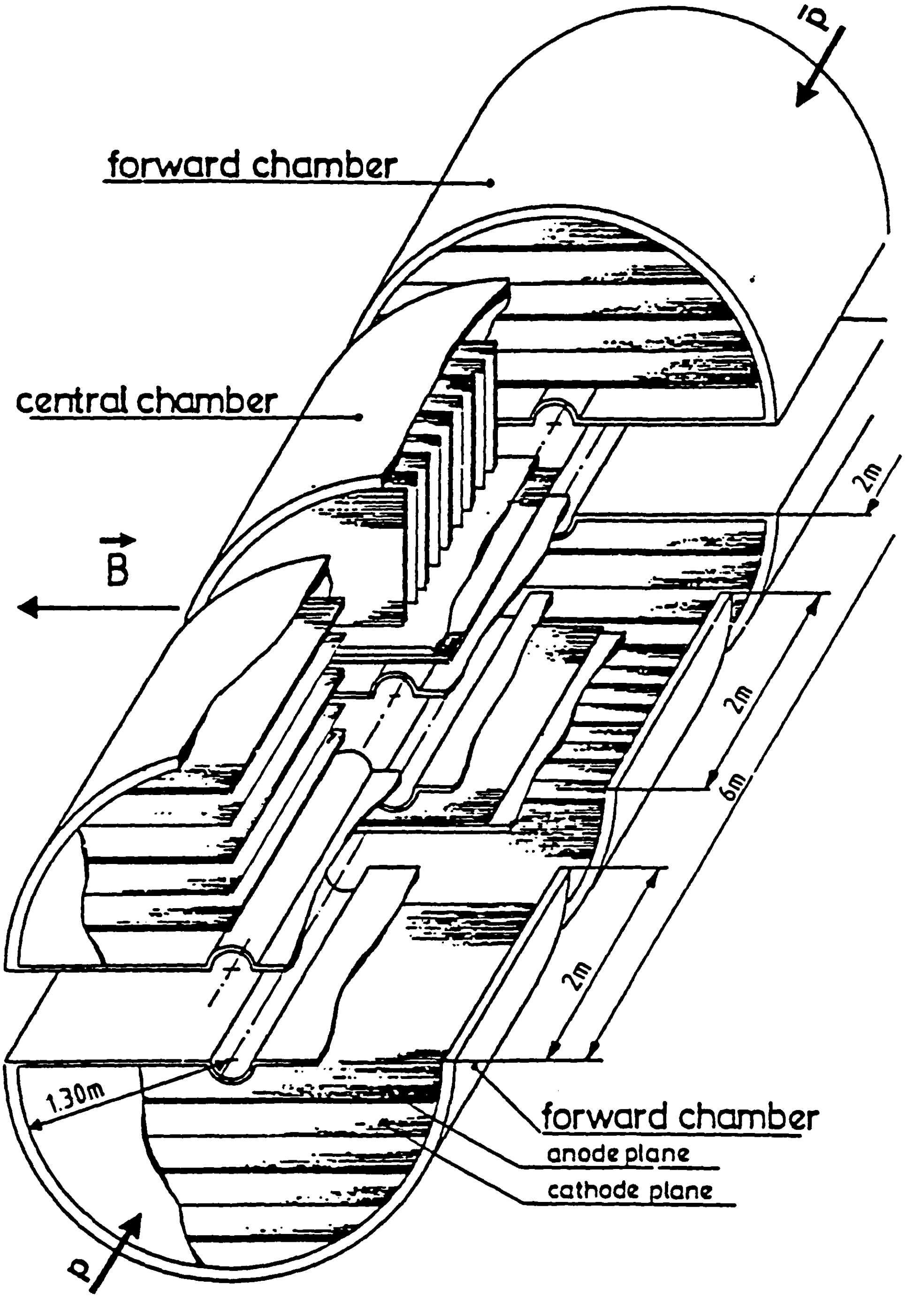

Figure (3.4) : *Cut-away diagram of the central detector.*

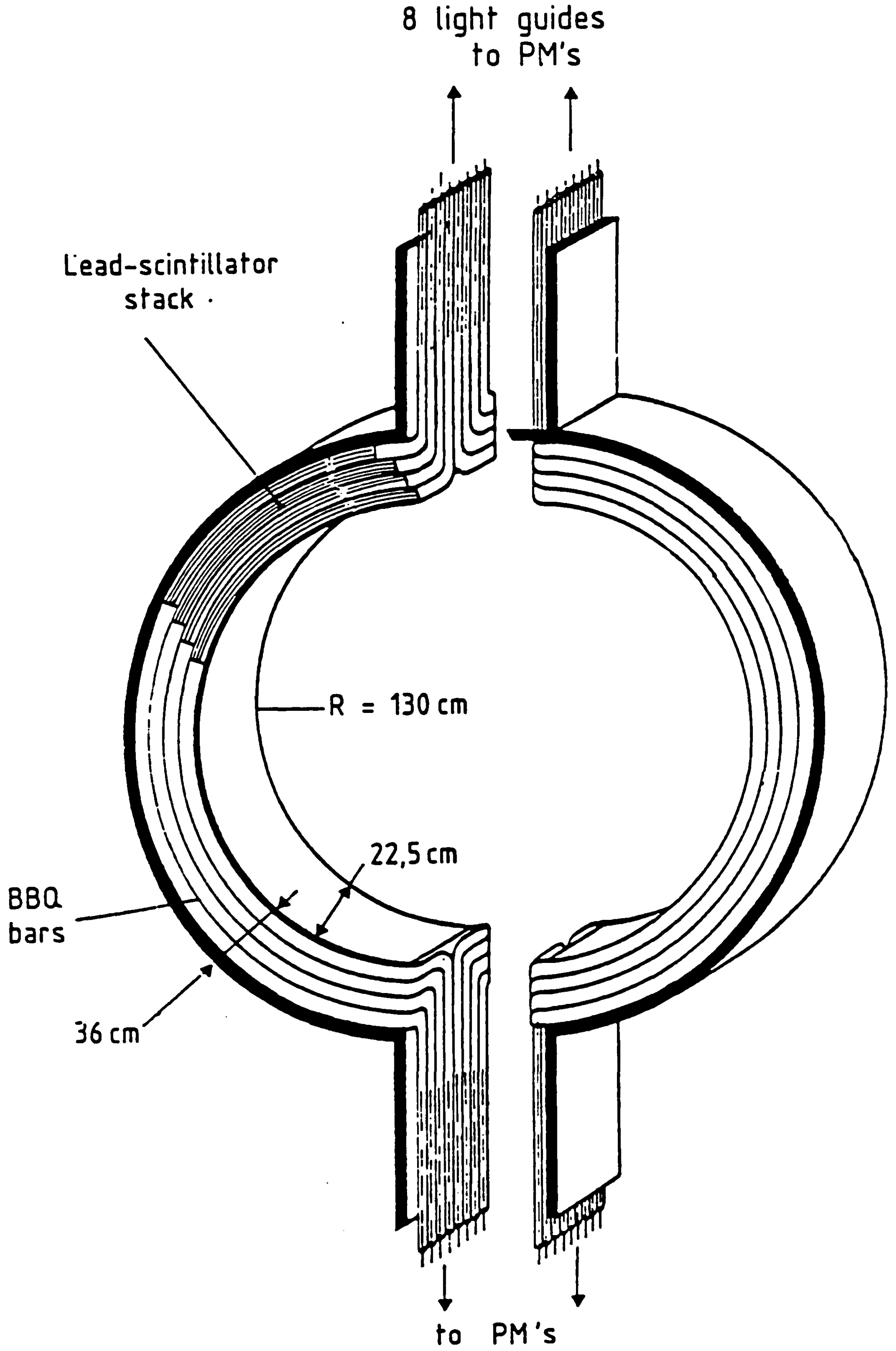

Figure (3.5) : *A schematic diagram of two gondolas.*

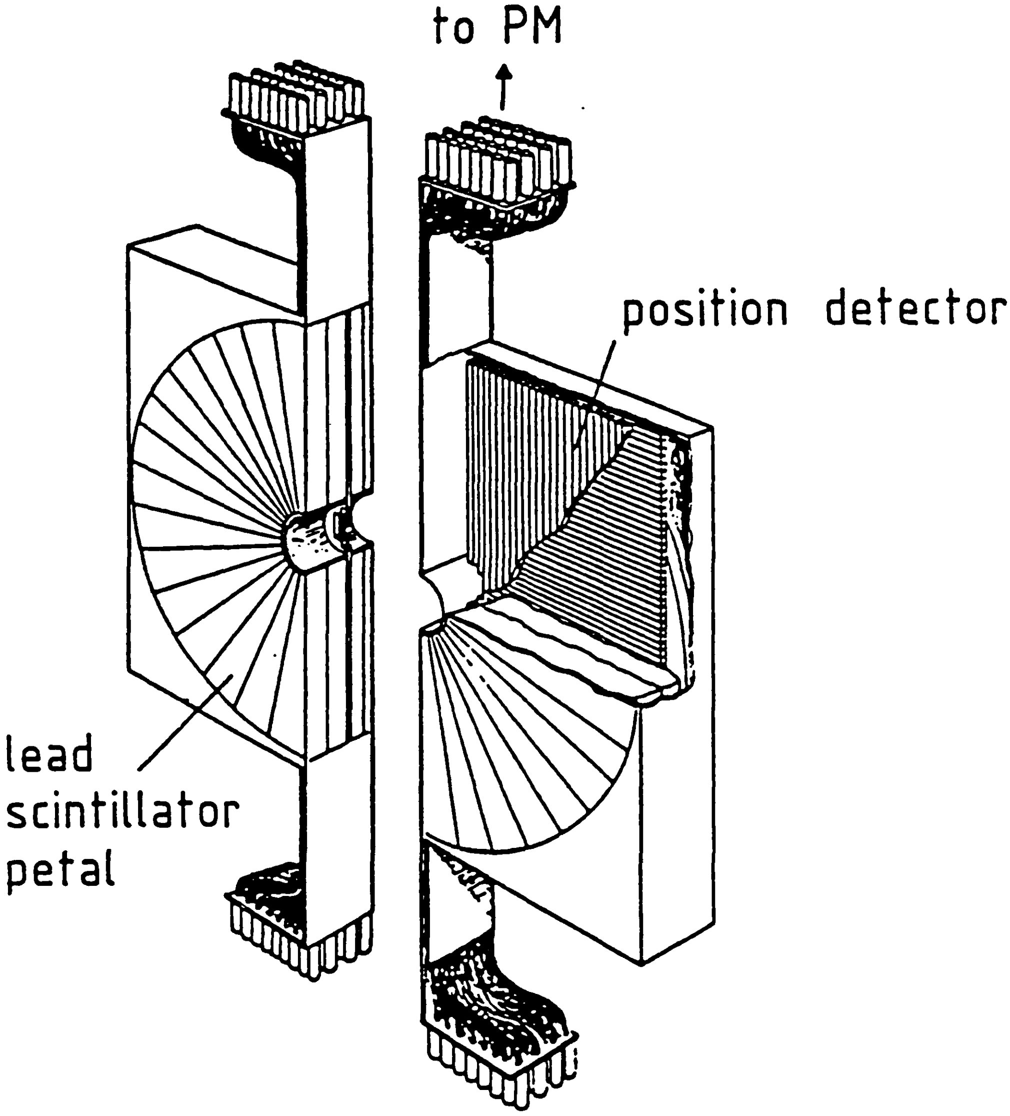

Figure (3.6) : *A schematic diagram of the bouchon petals and the position detector.*

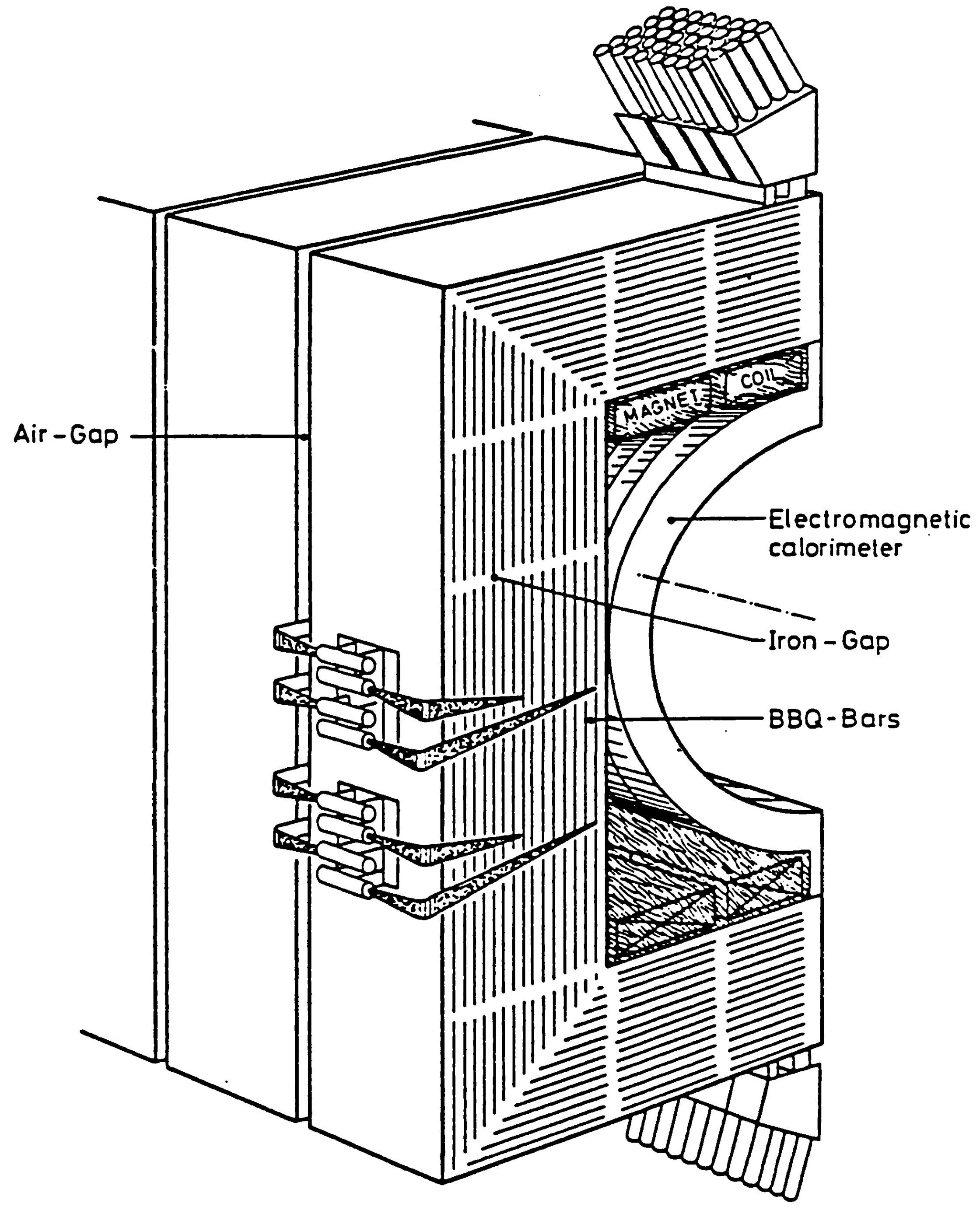

Figure (3.7) : *C-shaped modules for the central electromagnetic calorimeter.*

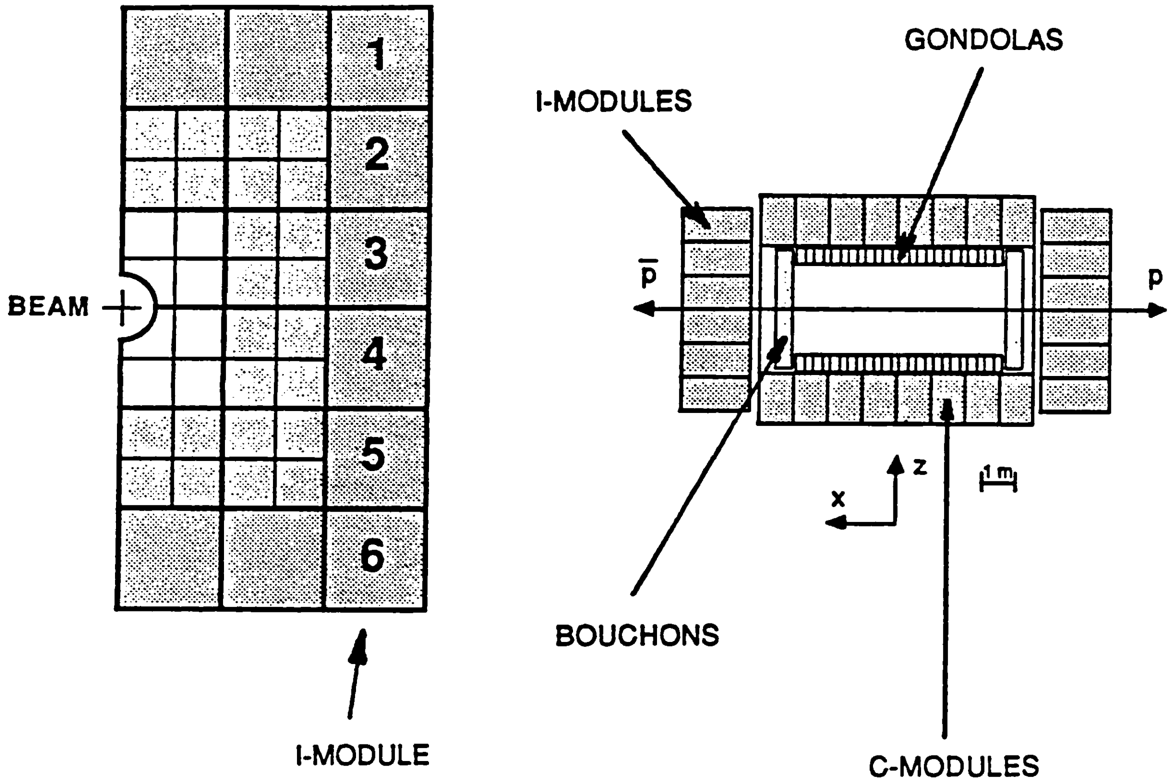

Figure (3.8) : *The stacks of a hadronic end-cap calorimeter(left) and a top view of the position of the I's with respect to the other calorimeters(right).*

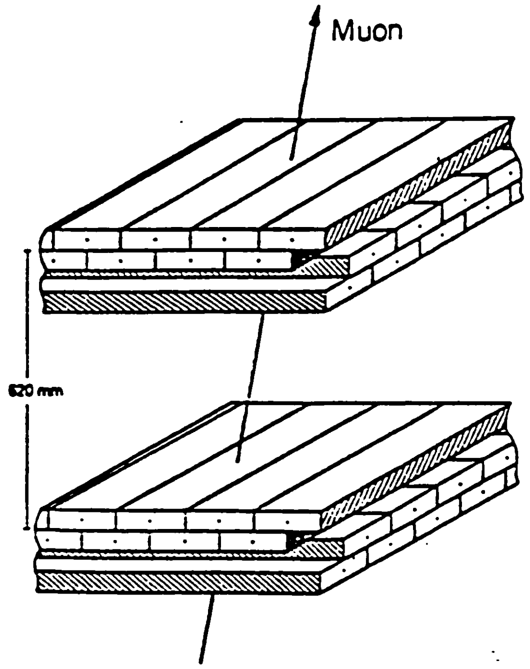

Figure (3.9) : *Schematic view of a section of the muon chambers.*

CHAPTER 4

JET FINDING AND THE MISSING ENERGY TECHNIQUE

4.1 INTRODUCTION

The purpose of the UA1 experiment was to study the physics of high energy hadron interactions. These interactions can lead to the production of prompt high energy leptons via the decays of the intermediate vector bosons (eg. $W \to e\ \nu$ or $Z \to e^+e^-$) or through the semi-leptonic decays of the heavy quarks (eg. $b \to c\tau\nu$). The detector is designed to detect and measure the properties of electrons, muons, photons and jets - but since the neutrinos do not interact in the detector their presence is inferred through the observation of an apparent transverse momentum imbalance in the event. The technique of measuring this momentum imbalance is called the missing energy technique. It has proved very effective in the selection of the $W \to e\nu$ events [40]. This is also a very useful technique in the search for any other conventional or new processes that produce neutral weakly interacting particles (eg. photinos of the supersymmetric theories) which escape detection by the apparatus.

The missing energy events (excluding $W \to e\nu$) are usually accompanied by jets. A jet is produced when a quark or a gluon fragments and hadronizes into a collection of particles. These particles then usually follow the direction of the quark or gluon and cluster in a collimated cone. Tau particles also give rise to jets through their semi-hadronic decay modes and $W \to \tau\nu$ events are one of the known sources of missing energy events.

The identification of a jet and the measurement of the jet energy is achieved by the use of a jet algorithm. It is the purpose of a jet algorithm to distinguish a cluster of particles that belong to a jet from the rather isotropic distribution of the underlying event. The standard UA1 jet algorithm was used for the identification of jets in the missing energy analysis. This algorithm is widely used in all analyses involving jets on UA1.

4.2 THE UA1 JET ALGORITHM

Jet finding is performed in two steps. The first step is to loop through all the calorimeter cells to construct energy vectors. An energy vector

$$\mathbf{E}_i = E_i \, \mathbf{u}_i \qquad (4.1)$$

is defined for each calorimeter cell with $E_T > 100$ MeV (the contribution of cells with $E_T < 100$ MeV to jets is negligible, so these cells are excluded from jet finding to reduce the time the algorithm takes). The unit vector $\mathbf{u}_i$ points from the interaction point to the centre of the shower (the centre of the cell for hadron calorimeters) in the cell i (see figure(4.1). The algorithm then searches through all the energy vectors and looks for those cells with $E_T > E_T^{min}$, these cells are called the initiators. E_T^{min} is the minimum transverse energy that a cell must have in order to initiate a jet (in the missing energy analysis, E_T^{min} was set to 1.5 GeV). Thus if a cell has $E_T > E_T^{min}$ it is expected that a cluster of energy (a jet) will be found consisting of that cell and some of the neighbouring cells. Upon being found the initiators are ordered according to the transverse energy deposition in each. The second step in the procedure is the merging of nearby initiators to construct jets. Each initiator (or energy vector) has associated with it a pseudorapidity (η) and an azimuthal angle about the x-axis (ϕ). The distance between two initiators in (η,ϕ) space, $\Delta R = (\Delta\eta^2 + \Delta\phi^2)^{1/2}$, is Lorentz invariant (for a boost along the beam axis) and is used to merge the energy vectors. Starting from the highest E_T initiator, all other initiators with $\Delta\eta$ and $\Delta\phi$ such that $\Delta R < \Delta R_{max}$ are added vectorially to the highest E_T initiator. A new jet axis (η and ϕ of the combined initiators) is defined after each such addition. Then the next unused highest E_T initiator is considered, and so on until all the initiators have been used. The parameter ΔR_{max} is the maximum distance allowed to merge cells. It can be seen from figure(4.2), which shows the distance ΔR of the calorimeter cells from the highest E_T jet for a sample of jet data(mainly two jets events), that the requirement $\Delta R_{max} = 1$ adequately separates the highest E_T jet from the other activity in the event. The second peak at $\Delta R \sim 3$ is due to the second jet in the events.

All the initiators having been merged into jets, the remaining energy vectors with $E_T < E_T^{min}$ are added to the nearest jet if ΔR (jet , cell) < ΔR_{max} =1. The jet finding in the calorimeters is then complete.

Jets can also be found in the central detector, where the charged energy flow is measured. The jet finding algorithm that is used in the central detector is similiar to the one used for calorimeter jet finding, except that it involves CD tracks as opposed to calorimeter cells. If any of these CD tracks has $P_T > P_T^{min}$ (P_T^{min} set to 1 GeV/c for the missing transverse energy analysis) then it is regarded as an initiator track. The algorithm constructs jets by merging these initiators (again ΔR_{max}= 1) and then adding the other tracks in the same way as the calorimeter reconstruction. As the the construction of the CD jets is totally independent of the construction of the calorimeter jets, they provide useful complementary information. In a missing transverse energy analysis this is highly desirable, since events in which a fake missing energy is generated by the the loss of a jet through the vertical cracks of the calorimeters can easily be spotted if a CD jet is pointing to the vertical crack (The CD has the best acceptance in the vertical regions).

4.3 THE JET ENERGY

The energy of a jet in the calorimeters is calculated by adding the measured energies in the cells comprising the jet. However a difficulty is associated with this measurement. There is a deposition of energy, by the jet, in both the electromagnetic and the hadronic calorimeters. The calorimeters are well calibrated, but for their respective types of particle. So when a jet (usually composed of a mixture of hadrons, primarily π^+ and π^-, and photons) passes through the electromagnetic calorimeters (gondolas and bouchons) its energy is underestimated. This is because the electromagnetic calorimeters are properly calibrated for electromagnetic showers and as a consequence underestimate the energy deposited by hadrons.

From Monte Carlo studies, a response factor has been calculated to correct the measurement of the jet energy. Then the correct jet energy is obtained by multiplication of this correction factor with the energy deposited in the electromagnetic calorimeters and addition of the result with the energy deposited in the hadronic calorimeters.

The response factor is shown as a function of shower composition in figure(4.3). Assuming a response factor of 1.0 for pure electromagnetic showers (contained completely in the gondolas or bouchons), the response factor increases to as much as 1.5 for a nearly pure hadronic shower.

It is known from jet data that on average about 80% (±10%) of the jet energy is contained in the electromagnetic calorimeters. This gives an average response factor of 1.13.

The measurement of the jet energy is also affected by some other effects:-

Particles belonging to a jet may be lost in cracks and insensitive areas where the instruments and supports of the calorimeters exist, leading to an underestimation of the jet energy. There are also other regions of poor detection capability eg. along the vertical edges of the gondolas, and the region of contact between gondolas and bouchons ($|\eta| \sim 1.4 - 1.5$). Another effect comes from the inefficiency of the jet algorithm which leads generally to an underestimation of the jet energy.

The above effects have been studied in detail and Monte Carlo methods yield results which show that the jet energy resolution is degraded and there is a systematic underestimation of the jet energy. From these studies a set of correction tables are produced which can be used to correct the energies of the jets as a function of η and E_T of each jet.

In the missing energy analysis presented here, unless stated otherwise, the jet energies, for the real and Monte Carlo events, are uncorrected and consequently so too are the missing transverse energies. The corrections are not necessary since the physics results derived at the end come from the data and Monte Carlo events processed with the same energy scale and jet construction. Therefore direct comparisons can be made without having to correct the jet energies. It should be noted that there is no experimental absolute calibration point in the UA1 experiment, so the precise jet energies are not known. So for any results coming from an analysis involving jet energies , this uncertainty must be taken into account as a systematic error. The systematic error in the absolute energy of jets, resulting from uncertainties in the calibration of the calorimeters, inefficiency of the jet algorithm, and in the composition of jets add up to ±10%. The energy and momentum of a jet can also be measured in the central detector, but since the neutral energy is not measured in the CD, these jets usually underestimate the jet energies.

4.4 THE MISSING TRANSVERSE ENERGY TECHNIQUE

Since the UA1 detector has nearly 4π calorimetry coverage, extending down to 0.2^0 with respect to the beam axis, with a small fraction of insensitive areas, the energy balance (equivalent to momentum balance at the energies of the collider) is governed only by the resolution of the calorimeters.

The calculation of the energy balance vector is performed as follows :
The energy E_i observed in cell i is summed over all the cells of the UA1 calorimeters. Then

$$\mathbf{E}_i^{\mathrm{bal}} = \sum_i E_i \mathbf{u}_i \qquad (4.2)$$

where $\mathbf{u}_i$ is the unit vector pointing from the interaction point to the centre of the shower observed in the calorimeter cell i (see figure(4.1)). the missing energy is then

$$\mathbf{E}^{\mathrm{miss}} = -\mathbf{E}^{\mathrm{bal}} = -\sum_i E_i \mathbf{u}_i \qquad (4.3)$$

A measurement of the longitudinal (along the x-axis) component of the missing energy cannot be made because of particles escaping down the beam pipe. The components transverse to the beam direction (the y and z components), however, can be measured quite well. So the important measurable quantity is the missing transverse energy vector, E_T^{miss}.

In figure(4.4) can be seen the distribution of the vertical component of the transverse energy for minimum bias events. In minimum bias events there should be no E_T^{miss} owing to weakly-interacting particles, as none are usually produced. The distributions of the transverse components, E_y and E_z, of E_T^{miss} are gaussians centred on zero with an rms width that can parameterised as $0.5 \sqrt{\Sigma E_T}$ (GeV), where

$$\sum E_T = \sum_i | E_i \mathbf{u}_{T_i} | \quad (\mathrm{GeV}), \qquad \text{Where } \mathbf{u}_{T_i} = \mathbf{u}_i - \mathbf{u}_{l_i} \qquad (4.4)$$

is the scalar sum of the transverse energies observed in all the calorimeter cells and is a measure of the activity in the event.

The resolution in missing transverse energy can be parameterised as a function of the activity of the event [44],

$$\sigma(E_T^{miss}) = 0.7\sqrt{\sum E_T} \quad \text{(GeV)} \qquad (4.5)$$

The variable

$$N_\sigma = \frac{E_T^{miss}}{\sigma(E_T^{miss})} = \frac{E_T^{miss}}{0.7\sqrt{\sum E_T}} \qquad (4.6)$$

is a measure of the significance of the missing transverse energy in an event and will be used extensively in this analysis.

4.5 OTHER SOURCES OF MISSING TRANSVERSE ENERGY

Muons, because they deposit a very small fraction of their energy in the calorimeters, also provide a source of missing transverse energy. However, by using the measurement of the muon momentum from the muon chambers and the central detector, the missing transverse energy can be corrected. In general, the missing transverse energy for muon events is the corrected one. But there are other sources of missing transverse energy.

(i) EXTERNAL BACKGROUNDS

Particles coming from outside the detector and not from the actual proton-antiproton interaction can deposit energy in the calorimeters thereby producing fake missing energy. Cosmic rays and beam halo events are two common sources of this background.

(ii) INSTRUMENTAL BACKGROUNDS

There can be a malfunction in part of the detector, eg. breakdown of photomultipliers, electronic noise. Apparent missing transverse energy may also be generated when particles are lost through cracks in the detector. hence if the missing transverse energy vector points to the vertical cracks in the calorimeters, the E_T^{miss} is probably fake. Problems in reconstruction of the event can also lead to apparent missing energy.

(iii) JET-FLUCTUATION BACKGROUND

Electromagnetic and hadronic shower energies can be measured by the calorimetry, because of its finite resolution, with large fluctuations about their actual values. This coupled with the fact that there are also regions of decreased sensitivity (eg. the vertical edges of the calorimeters, which affect the measurement of the jet energies) can lead to large amounts of anomalous missing energy. The direction of the E_T^{miss} vector is usually along one of the jets.

It is the objective of the missing transverse energy technique to select events with true missing transverse energy and to minimize the contamination from the above backgrounds.

4.6 THE JET-FLUCTUATION MONTE CARLO

Consider a two jet event, in which the two jets are back-to-back in the transverse plane. If the measured energy of one of the jets fluctuates to zero, an event with a monojet configuration will be observed. There will be a jet on one side of the detector balanced by missing transverse energy on the other. Events possessing this sort of topology are very difficult to separate from a sample of events with genuine missing energy, so one has to perform a Monte Carlo study to accurately calculate their contribution to the data sample.

It is possible, in principle, to generate a large sample of such events employing the ISAJET [42] Monte Carlo. Then the UA1 detector simulation and reconstruction programs will fluctuate the jet energies according to the known calorimeter response to jets. However because of the requirement of a very large sample of such events, the length of time required by the simulation and reconstruction programs proves prohibitive. So it is to another technique one that looks.

The alternative method is known as the jet-fluctuation Monte Carlo, which uses a sample of fully reconstructed UA1 jet data. It is necessary, in the first place, to select from these jet data those events that have well measured jet energies and are not due to external or instrumental backgrounds. This is achieved by requiring the events to have $N_\sigma < 1$ and for there to be at least two jets in the event, with $E_T^{jet1} > 15$ GeV, $E_T^{jet2} > 10$ GeV and $E_T^{jet1} + E_T^{jet2} > 30$ GeV. E_T^{jet1} is the highest energy jet in the event and E_T^{jet2} is the second highest.

The jet-fluctuation Monte Carlo performs the following two steps:

(i) It balances all the jets in the event

(ii) It randomly fluctuates the jet energies about their values from step (i), according to a known resolution function.

Step(ii) is repeated many times for each event, generating a large sample of fluctuated events. A sample of 3180 nb^{-1} was generated. The distribution of N_{σ}^{2} from the jet-fluctuation Monte Carlo (the solid curve in figure(4.5)) provides a good description of the N_{σ}^{2} distribution for the UA1 jet data sample. It is clear that as N_{σ}^{2} increases, the probability that the missing transverse energy is due to the finite resolution of the calorimeters decreases.

The reliability of the predictions of the Monte Carlo has been checked by the variation of the missing energy selection cuts and confirmation that the changes in the data sample, in terms of rates of events and various distributions, are correctly reproduced by the Monte Carlo events.

To evaluate the contribution of this jet-fluctuation background to the E_T^{miss} data sample one has to apply to the jet-fluctuation sample the same selection cuts as used in the definition of the E_T^{miss} data sample.

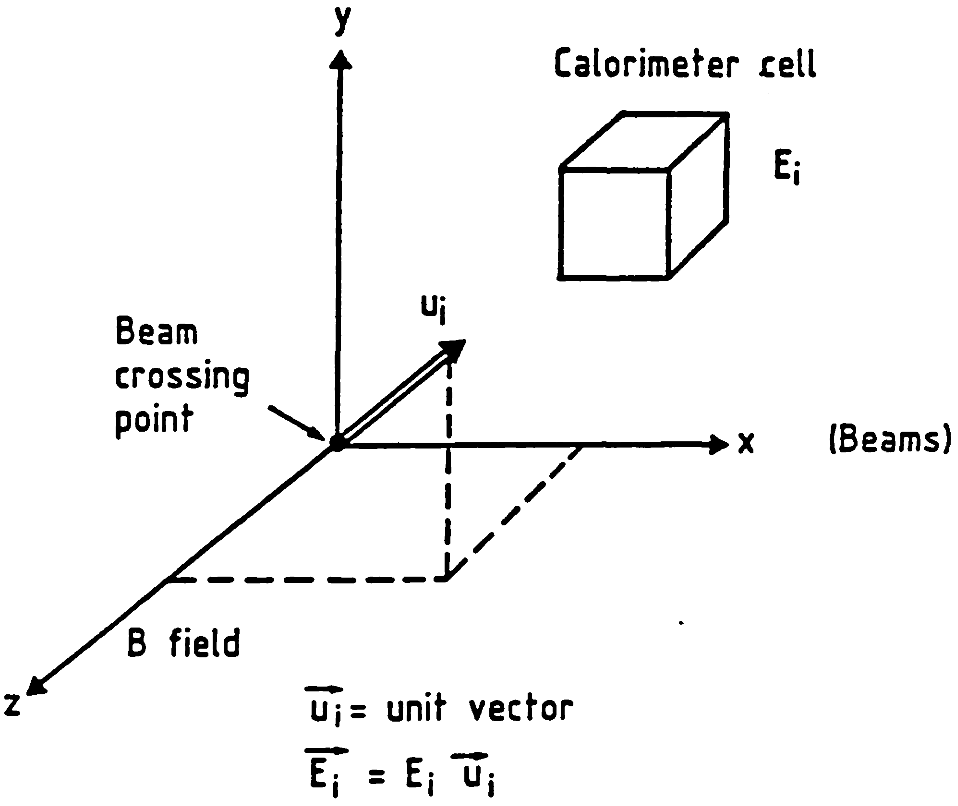

Figure (4.1) : *Construction of energy vectors.*

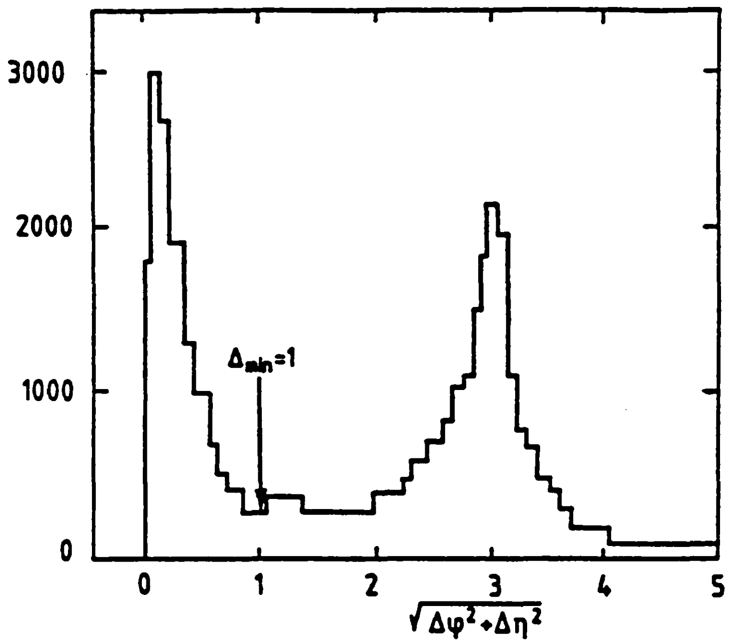

Figure (4.2) : *The distance in* (η,φ) *space of all calorimeter cells from the highest* E_T *jet.*

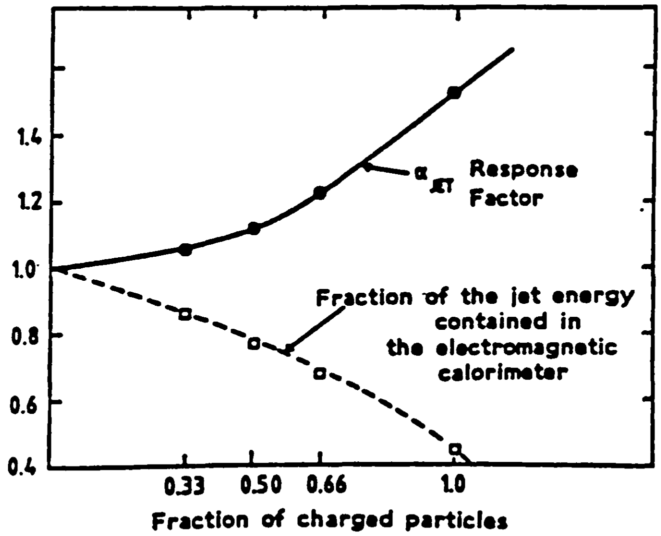

Figure (4.3) : *Response factor as a function of shower composition.*

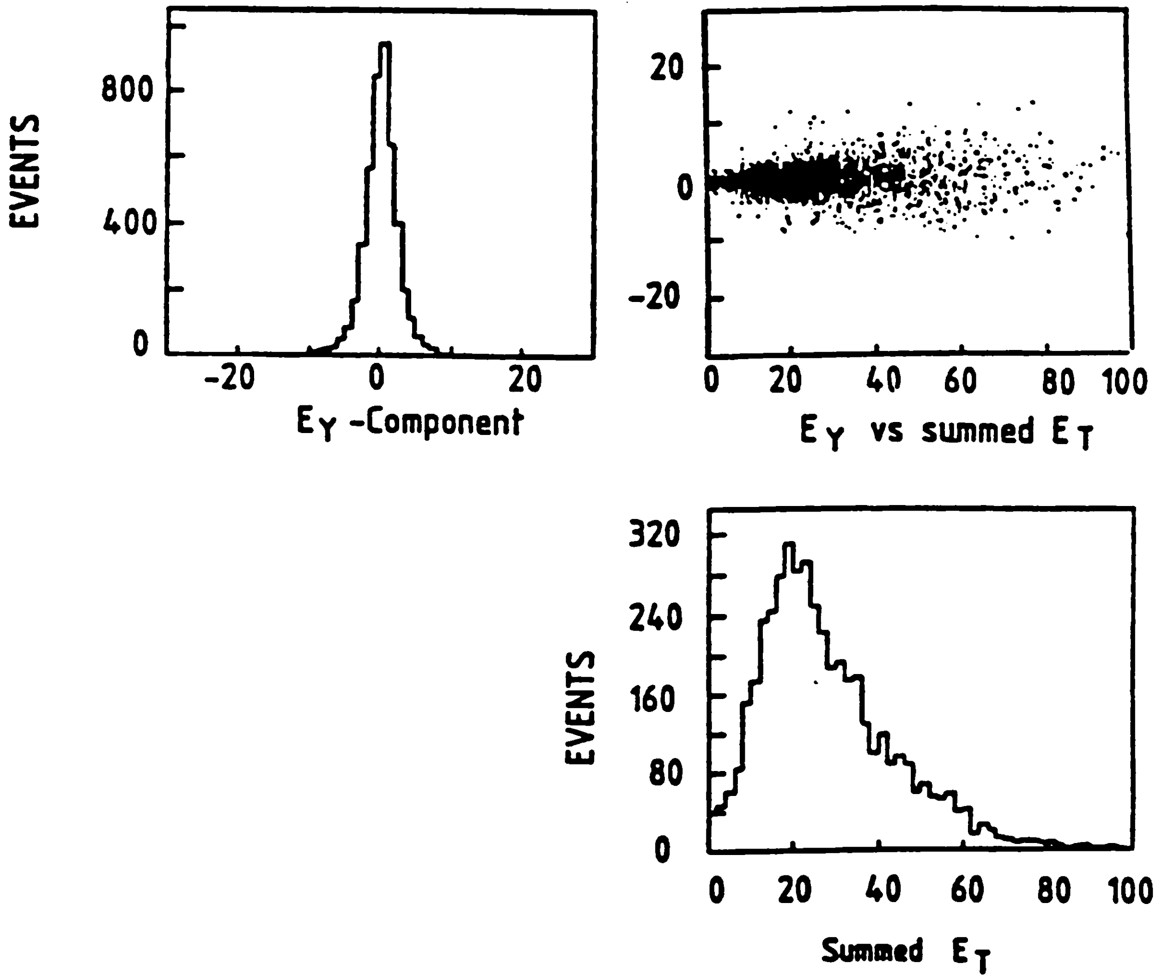

Figure (4.4) : *Scatter plot of the y-component of missing energy versus the total transverse energy observed in all calorimeter cells.*

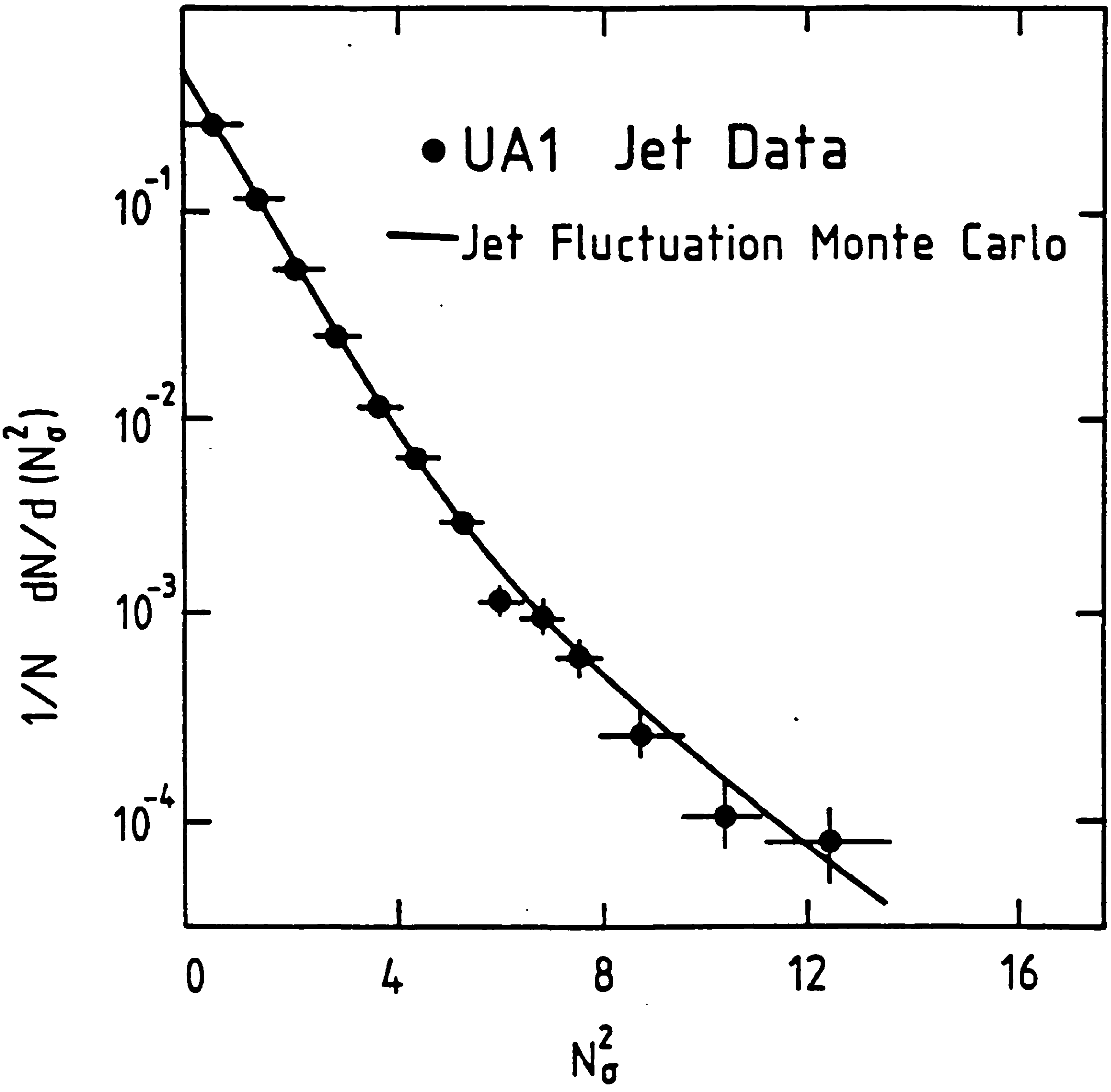

Figure (4.5) : *Jet fluctuation Monte Carlo predictions for* N_σ^2 *compared with a sample of UA1 jet events.*

CHAPTER 5

THE MISSING TRANSVERSE ENERGY DATA SAMPLE AND THE STANDARD MODEL CONTRIBUTIONS

5.1 INTRODUCTION

The selection of events containing a large amount of missing transverse energy is motivated by the search for new physics processes. These new processes would not be described by the Standard Model and would produce new weakly interacting particles carrying away momentum and thereby generating large missing transverse energy. The selection, which is devised to yield an inclusive sample of missing transverse energy events with a minimum contribution from those background processes discussed earlier, will however contain Standard Model contributions from events that produce a large missing transverse energy, eg.

$$W \longrightarrow \tau\nu$$
$$Z^0 + g \text{ or } q \longrightarrow \nu\nu + \text{jet}$$

These processes will be simulated and their contributions to the missing transverse energy data sample evaluated.

The data used in this thesis were recorded during the following three periods of data taking :

Year	1983	1984	1985
Integrated luminosity (nb^{-1})	118	263	334
$\sqrt{s}$ (GeV)	546	630	630

In total an integrated Luminosity of 715 nb^{-1} was recorded during these periods. These events were selected from approximately 3×10^{10} inelastic $P\overline{P}$ interactions observed in the UA1 detector.

5.2 THE HARDWARE TRIGGERS

Events were recorded by the data acquisition system if they satisfied one or more of the following hardware triggers [43],[58] :

- electromagnetic transverse energy trigger, requiring transverse energy greater than 10 GeV in two adjacent electromagnetic elements,

- Jet E_T trigger, requiring a jet with $E_T > 25$ GeV,

- Transverse energy imbalance trigger, requiring a jet with $E_T > 15$ GeV together with missing transverse energy exceeding 17 GeV. The energy imbalance trigger was added in 1984 and remained active in 1985 as well.

5.3 THE ON-LINE SELECTION

This selection was incorporated in the data reduction in 1984. All events that triggered the detector were taken as input to the 168/E emulators. These processors then kept only those events satisfying certain selection criteria based on information from the calorimetry or muon detectors. The events passing this selection were written onto special tapes (for express-line analysis) and normal tapes, or onto normal tapes only. This on-line selection was based on the calculation, by the processors, of missing transverse energy and N_σ. Then if the event had missing transverse energy less than 15 GeV it was rejected. If it had missing transverse energy greater than 15 GeV it was written onto normal tape and if in addition it had $N_\sigma > 3.5$ and was not obviously due to background, it was written to express tape too.

Approximately 30% of the missing energy triggers passed this on-line missing E_T selection, of which 5% were written to special tape. The rate of events out of the on-line selection was less than the maximum 4 Hz writing speed possible for the data acquisition system.

5.4 THE OFF-LINE SELECTION

Before the off-line selection could be applied to the events accumulated on tape, which were in raw data format, they had to be processed.

The first stage in this procedure, the preprocessing stage, carried out the transformation of the data format and the application of the calibration constants.

The second stage, the reconstruction stage, performed track finding, momentum measurement, and vertex reconstruction in the central detector; calculation of the position and energy of showers in the electromagnetic and hadronic calorimeters; track finding and muon measurement in the muon chambers. It also matched information from different parts of the detector.

After processing, the events on tape were passed through a missing E_T filter - which required the events to possess a significant amount of missing transverse energy by imposing the cuts: $E_T^{miss} > 15$ GeV and $N_\sigma > 2.5$ or $E_T^{miss} > 25$ GeV.

To define the starting missing transverse energy data sample the following minimium requirements, to remove events coming from the external and instrumental backgrounds, were made:

- Missing transverse energy $E_T^{miss} > 15$ GeV and $N_\sigma \geq 3$.
  This rejected a major portion of the jet-fluctuation background.

- Veto of vertical jets : Remove events having a jet in the central detector ($P_T > 7.5$ GeV/c) within $\pm 15^0$ or a jet observed in the calorimeters ($E_T > 12$ GeV) within $\pm 20^0$ in ϕ of the vertical cracks in the calorimeters.

- $N_{CD} = 0$ cut : remove events which had no tracks in the central detector with $P_T > 1$ GeV/c inside a cone $\Delta R = 0.4$ ($\Delta R^2 = \Delta\phi^2 + \Delta\eta^2$, where ϕ is the azimuthal angle and η is the pseudorapidity) around the axis of the highest E_T calorimeter jet. This removed beam halo and cosmic ray events. It also removed events that had reconstruction problems in the gondolas (The so called gondola-ϕ problem, This problem occurred when two clusters of energy in the top and bottom of the same gondola were reconstructed as one cluster in the middle with no high P_T track in the CD pointing to it (see figure (5.1)). An over-estimation in the energy of this fake cluster resulted in apparent missing E_T).

- A number of further technical cuts to reduce backgrounds coming from beam halo, cosmic ray and double interaction events.

After these loose cuts, 5% of the initial sample of events selected by the missing E_T filter is left. This yields a sample of 5973 events, with the $N_\sigma \geq 3$ cut accounting for the largest number of events that failed the cuts.
The N_σ distribution for the selected events is shown in figure(5.2).
An enhancement is seen at large N_σ. This indicates the possible existence of a signal in the region $N_\sigma \geq 5$ superimposed on a rapidly falling background. In figure(5.3) the distribution of E_T^{miss} versus the jet E_T for the highest E_T jet for the selected events is shown. The presence of events with low values of E_T^{jet} but significant E_T^{miss}, topologies not expected from Standard Model processes, suggested that a tighter selection would be needed to reduce residual backgrounds.

The selection was tightened by imposing [7],[8],[58]:

- The requirement of one or more jets observed in the calorimeters with $E_T > 12$ GeV.

- The isolation of the missing transverse energy vector, by rejecting events with a jet observed in the calorimeters (and/or in the central detector) with $E_T > 8$ GeV (and/or $P_T > 5$ GeV/c) within $\pm 30^0$ in azimuth of the missing transverse energy direction (see figure (5.4)).

- Veto on back-to-back jet activity, by rejecting events with a calorimeter jet of $E_T > 8$ GeV (and/or a central detector jet with $P_T > 5$ GeV/c) within 150-210^0 in ϕ of the direction of the highest E_T jet (see figure (5.5)).
- The vertical E_T^{miss} cut, removing those events in which the missing E_T vector pointed to within $\pm 20^0$ in ϕ of the vertical cracks of the calorimeters.
- Veto of events recognised as having an electron or a muon. This removed $W \rightarrow e\nu$ and $W \rightarrow \mu\nu$ decays which will contain large E_T^{miss}.

Additional technical cuts were applied to remove background events such as cosmic rays, beam halo and double interactions. At the end of this tight selection all the events were checked visually on a graphics display and any exhibiting clear evidence of external backgrounds were rejected.

From the 5973 events of the loose selection, 167 passed this tight selection. The largest fraction of events being rejected by the E_T^{miss} isolation requirements. The residual background contribution for instrumental and external backgrounds to this sample being estimated to be ~2 events.

Figure (5.6) shows the N_σ distribution for the 167 events.

The shaded region shows the expected contribution from jet-fluctuation background. In order to minimise the jet fluctuation and other backgrounds a cut of $N_\sigma \geq 4$ is made. This reduces the jet-fluctuation background to 3.8 events and the other backgrounds to « 1 event.

This 4σ cut yields a sample of 56 events, referred to as the '4σ data sample'.

Figure (5.7) shows a scatter plot of E_T^{jet} of the highest E_T jet in the event against E_T^{miss} for the 56 events.

This 4σ data sample contains 53 mono-jet events and 3 di-jet events.

Figures (5.8) and (5.9) show event displays of the mono-jet and di-jet with highest values of missing E_T.

5.5 STANDARD MODEL CONTRIBUTIONS

In order to be able to search effectively for new physics in the 4σ data sample, defined above, one needs to accurately evaluate the contribution to it from Standard Model physics.The Standard Model physics processes expected to contribute to the 4σ data sample are:

- W and Z^0 processes, these include

  (i) The leptonic decays of the intermediate vector bosons
  $W \to e\nu$
  $W \to \mu\nu$
  $W \to \tau\nu \to$ leptons
  $Z^0 \to \tau^+ \tau^- \to$ leptons
  However, most of these will be removed by the selection cuts.

  (ii) $Z^0 \to \tau^+ \tau^-$
  $W \to \bar{c}s / c\bar{s}$
  $Z^0 \to c\bar{c}$ or $b\bar{b}$
  With the tau particles or the quarks decaying semi-leptonically.

  (iii) $Z^0 \to \nu\bar{\nu}$, for three neutrino species. The Z^0 recoiling against gluon jets.

- $W \to \tau\nu \to \nu\nu$ + hadrons , the tau decaying semi-hadronically.

- Heavy flavour processes,
  $P\bar{P} \to c\bar{c}$ or $b\bar{b}$, with the subsequent semi-leptonic decay of one or both quarks.

All the above processes were generated using the ISAJET [42] Monte Carlo program. The ISAJET program generates a complete $P\bar{P}$ event including hadronisation both of the quarks and gluons from the hard scattering and of the spectator partons not involved in the hard collision (beam fragmentation). The hard-scattering process (W or Z production via the Drell-Yan mechanism, or high P_T jet production) is generated according to leading-order perturbative QCD calculations. Initial and final-state gluon bremsstrahlung is included.

The Monte Carlo generated events were passed through a complete simulation of the UA1 detector and hardware trigger, and then through the same chain of reconstruction and analysis programs as were used for the data. The detector simulation programs simulate the response of the various parts of the UA1 detector to the Monte Carlo particles and yield events that have the same format as the real raw data. After processing, the same cuts as used for the selection of real data can be applied directly to Monte Carlo events.

The generated Monte Carlo statistics correspond to an integrated luminosity of approximately ten times the actual recorded luminosity.

For the W --> $\tau\nu$ calculation, the decay matrix elements in ISAJET were modified to include the effects of tau polarisation[58]. The branching ratios for the leptonic and semileptonic decays of the tau were adjusted using the latest experimental values[44].

The normalisation for all processes involving W or Z production was taken from the cross-sections for σ.B(W-->eν) and σ.B(Z^0-->e^+e^-) measured by UA1[45]. For the direct production of heavy quarks ($P\bar{P}$--> $b\bar{b}$ or $c\bar{c}$), the normalisation was derived from the inclusive muon cross-section measured by UA1[46].

The beam fragmentation in ISAJET was carefully tuned to reproduce UA1 minimum bias, jet, and W --> eν data.

For processes involving W production, the W boson P_T distribution generated in ISAJET was modified to agree with the measured P_T spectrum. The P_T spectrum for Z^0 bosons was similarly modified in such a way as to leave the relative shapes of the W and Z^0 P_T spectra unchanged.

5.5.1 MONTE CARLO RESULTS

In figures(5.10) and (5.11) can be seen the distributions for the missing transverse energy and transverse energy of the highest E_T jet for the 56 4σ data sample events (histogram) , and the contributions of the various Standard Model sources. The first column of table(5.1) contains the breakdown of the various contributions of the Standard Model sources to the 4σ data sample. In total 52.2 events are predicted, to be compared with 56 observed. From the distributions it can be concluded that the Monte Carlo predictions provide a good description of the data.

5.5.2 SEPARATION OF THE W --> $\tau\nu$ SIGNAL

The Monte Carlo calculations of the contributions expected from W, Z^0 and heavy flavour production show that the 4σ data sample (56 events) is expected to be dominated by W --> $\tau\nu$ decays, where the tau then decays semi-hadronically (36.7 events out of a total prediction of 52.2 events). Since in searching for new physics this signal has to be treated as background, one needs to develop selection criteria which will enable the separation of this contribution. This criterion is based on variables by which hadronic jets from tau decays can be distinguished from typical quark or gluon jets

Semi-hadronic tau decays are dominated by low-mass final states containing either one or three charged hadrons. Together with the large Lorentz boost given to the tau from the W --> $\tau\nu$ decay, this produces isolated, collimated, low-charged multiplicity jets.

A comparison of tau jets generated by the tau Monte Carlo with jets in a sample of inclusive UA1 jet data identified three quantities that provide a useful separation for τ --> hadron decays.

- Narrowness of the calorimeter jet: the total scalar transverse energies contained within cones of half-angle $\Delta R = 0.4$ and $\Delta R = 1$ about the calorimeter jet axis are used to define the ratio

$$F = \Sigma E_T(\Delta R < 0.4) / \Sigma E_T(\Delta R < 1)$$

An isolated pencil jet will have $F = 1$, whilst a broad jet will have a smaller value of F: $0 < F < 1$.

- Matching between the CD and calorimeter jets : measured by the separation R between the calorimeter jet axis and the highest P_T track associated with the jet.

- Charged track multiplicity : defined as the number n of charged tracks with $P_T > 1$ GeV/c contained within a cone $\Delta R < 0.4$ about the calorimeter jet axis.

The distributions of F, R and n from the τ --> hadron Monte Carlo and from a sample of inclusive jet data are shown in figures(5.12a)-(5.12c). As is expected, the jets from the tau decay typically have larger values of F, smaller values of R, and lower multiplicities n than jets from the jet data sample.

The three variables F, R and n are now combined into a single variable, the τ log-likelihood L_τ defined as as follows :

$$L_\tau = \log_e(P_F P_R P_n) + \text{arbitrary constant}$$

Where P_F, P_R, P_n are the values of F, R and n distributions obtained from the τ --> hadron Monte Carlo for the measured variables F, R and n for the highest E_T jet in the event.

In figure(5.12d), the distribution of L_τ obtained from the W --> $\tau\nu$ Monte Carlo is compared with the same distribution from inclusive jet data. It was decided to define the τ sample by requiring the highest E_T jet in the event to possess a value of $L_\tau > 0$. This cut retains 78% of the jets from τ --> hadron decays and rejects 89% of ordinary jets. The L_τ distribution for the 56 4σ events is also shown in Figure(5.12d). The requirement $L_\tau > 0$ selects a sample of 32 τ candidates from the 4σ sample. A couple of examples of events with $L_\tau > 0$ (a one-prong and a three-prong τ candidate) are shown in figure(5.13).

The non-tau sample, for which $L_\tau < 0$, is used to search for new physics. Figure(5.14) shows a plot of E_T of the highest E_T jet in the event versus L_τ for the 56 events of the 4σ data sample. In the projections the shaded region shows the non-tau contributions, and the solid line shows the total contribution including the tau events.

There are 24 events below the $L_\tau = 0$ line. The contributions from all the other standard physics processes to this non-tau sample are shown in the second column of table(5.1). It can be seen that the total prediction of 20.8 ± 6.1 events is in good agreement with the 24 events observed and is dominated by two contributions : τ --> hadrons that are not cut by the $L_\tau > 0$ requirement (8.0 events), and the process PP --> Z^0 + jet (Z^0 --> $\nu\nu$) (7.1 events).

Before one makes a more detailed comparison of the data with the Standard Model expectations it is necessary to discuss the systematic uncertainties attached to the Monte Carlo calculations.

5.5.3 SYSTEMATIC ERRORS

A major uncertainty in the calculation of the contribution to the non-tau sample from W and Z^0 processes is the limited knowledge of the P_T spectrum of the produced W or Z^0 at high P_T. This mostly affects the process $Z^0 \rightarrow \nu\nu$.

The $P_T(W)$ spectrum has been measured by UA1 using the $W \rightarrow e\nu$ sample of 255 events and $W \rightarrow \mu\nu$ sample of 57 events. This distribution is shown in figure (5.15).

The $P_T(W)$ spectrum for the standard ISAJET Monte Carlo was adjusted to agree with the $P_T(W)$ distribution measured from the UA1 samples. This modified $P_T(W)$ distribution is consistent with the perturbative QCD calculation of Altarelli et al. [47] see figure(5.15).

The uncertainty on the $P_T(W)$ distribution has been accounted for by the computation of an error on the Monte Carlo contributions based on the statistics of the UA1 $W \rightarrow e\nu$ and $W \rightarrow \mu\nu$ samples for several bins of $P_T(W)$ [58]. Thus the limited $W \rightarrow e\nu$ and $W \rightarrow \mu\nu$ statistics available at large values of $P_T(W)$ are reflected in a correspondingly large error being assigned to that component of the Monte Carlo coming from the high- $P_T(W)$ tail. There are a number of other systematic errors on the Monte Carlo contributions :

- An uncertainty of $\pm 10\%$ in the overall energy scale for the calorimeters.
- Uncertainties in the tau branching ratios
- Systematic uncertainties in the predictions of the jet-fluctuation Monte Carlo ($\pm 20\%$)
- Uncertainties in the cross-sections for heavy flavour production

The combined systematic error from these uncertainties is 1.1 event and is small compared with the error of 4.6 events from the $P_T(W)$ uncertainty , for the Monte Carlo contribution to the non-tau sample (20.8 events) see table (5.1).

5.5.4 NON-TAU SAMPLE

The distributions of E_T^{miss} and E_T^{jet} for the non-tau sample are shown in figures(5.16) and (5.17) respectively. It can be seen that Monte Carlo predictions provide a good description of the data. The sensitivity to the shape of the W and Z^0 P_T distributions is largest at large values of E_T^{miss} or E_T^{jet}. For example, for $E_T^{jet} > 40$ GeV (7 events are observed), a total of $3.0 \pm 1.8 \pm 0.3$ events are predicted.

It can be concluded that within the presently available statistics, the large E_T^{miss} sample can be understood in terms of known Standard Model processes. The non-tau sample can now be used to place limits on new physics processes.

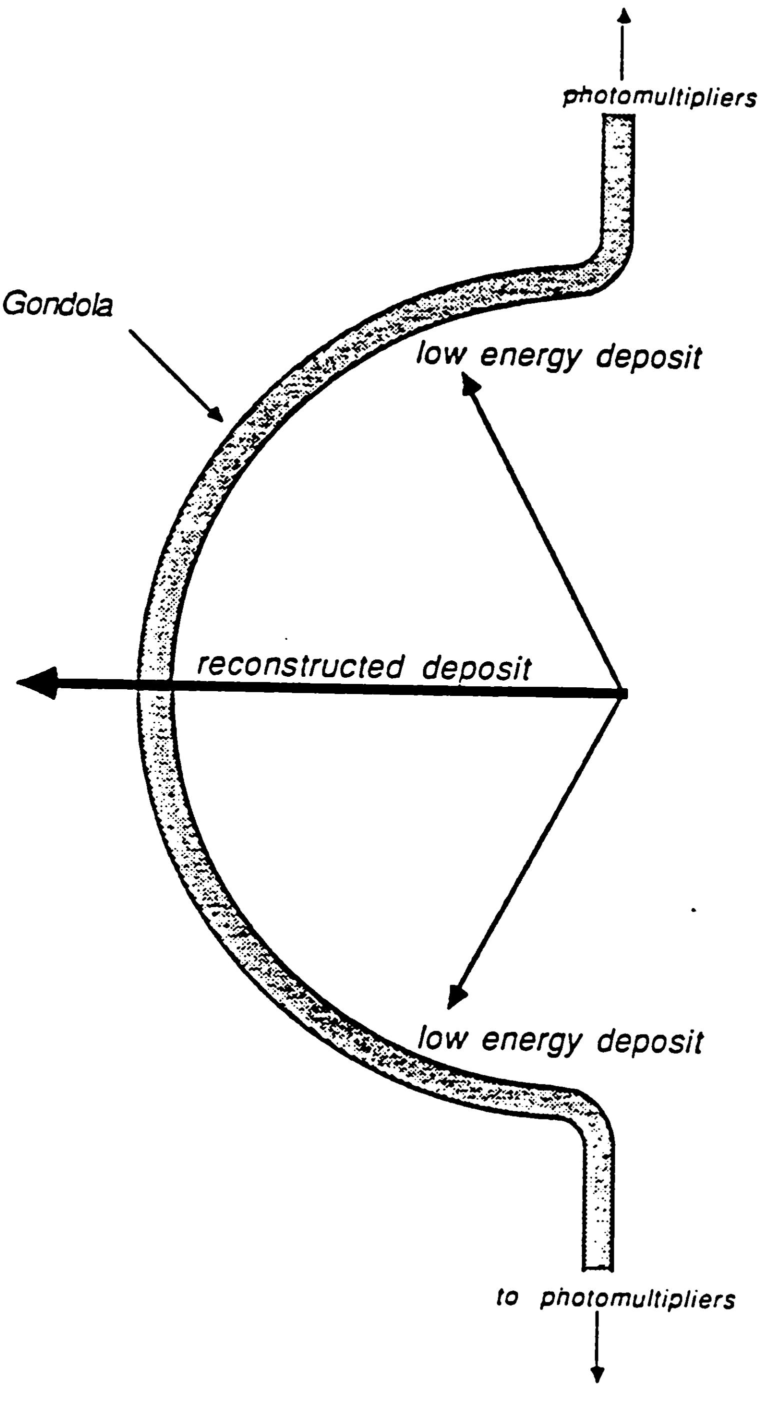

Figure (5.1) : *The gondola-φ reconstruction problem.*

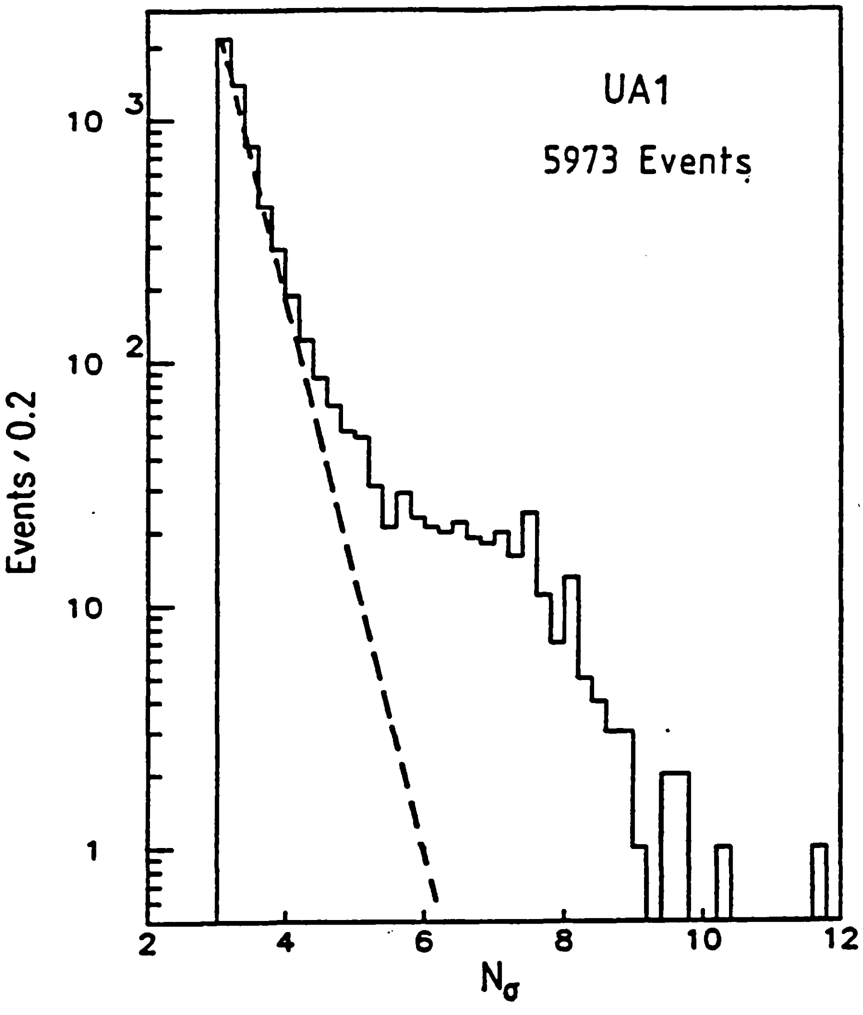

Figure (5.2) : *Distribution of* N_σ *for a loose* 3σ *selection of the data. The dashed curve shows the predicted jet fluctuation background.*

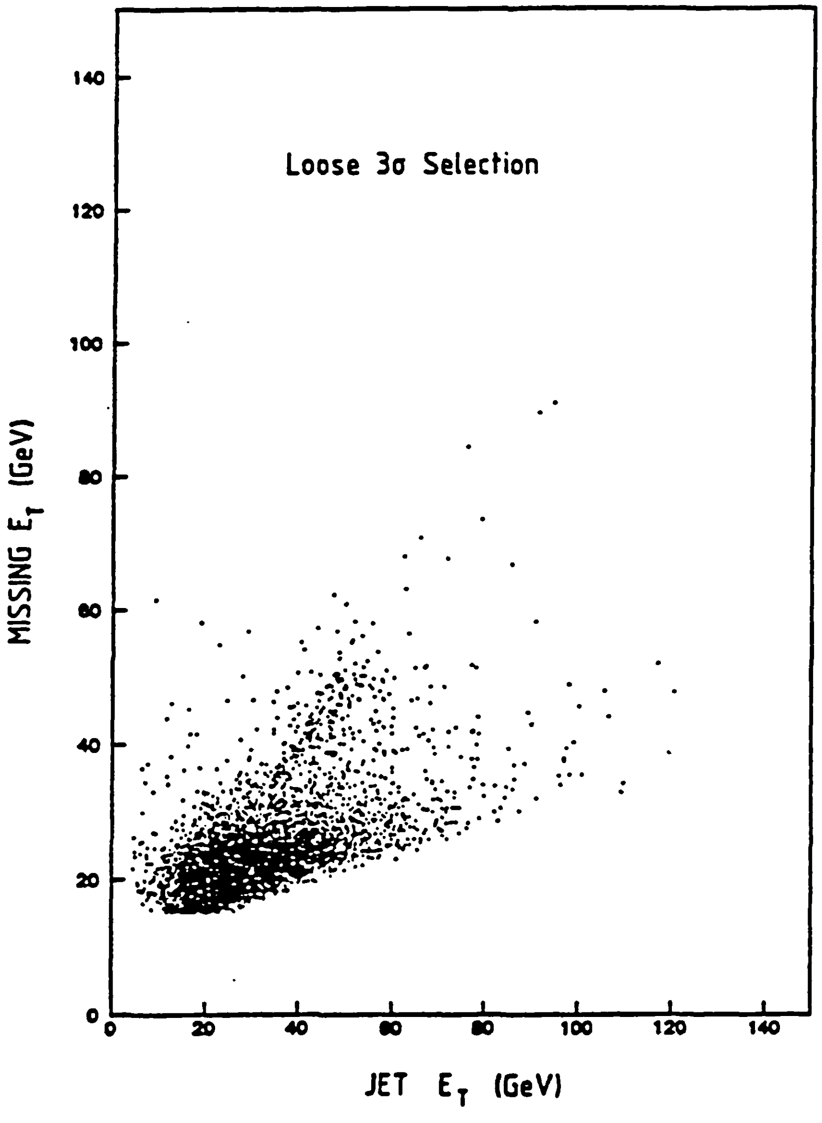

Figure (5.3) : *A scatter plot of missing transverse energy versus jet* E_T *for the highest jet in the event, for a loose* 3σ *selection.*

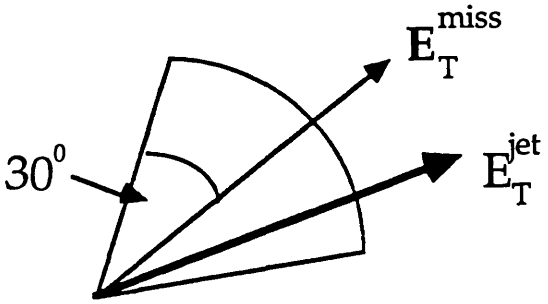

Figure (5.4) : *Isolation requirements of the missing transverse energy vector.*

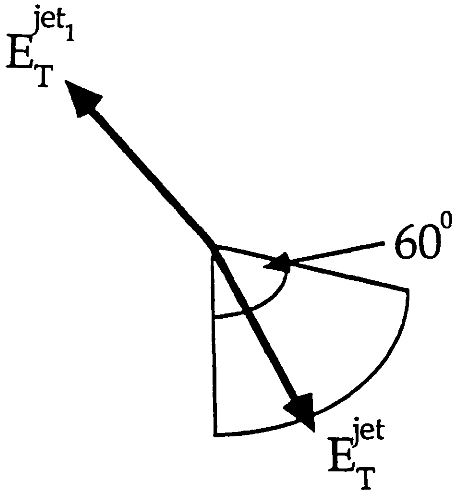

Figure (5.5) : *Veto of events with back-to-back activity.*

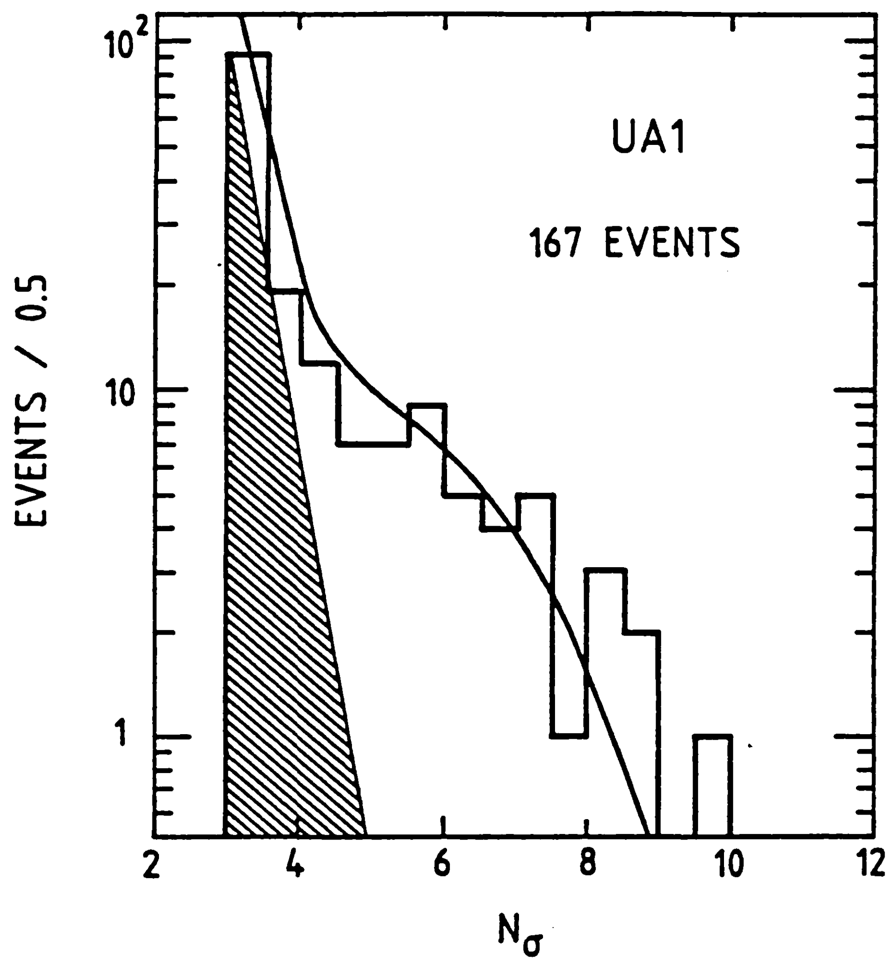

Figure (5.6) : *N_σ distribution for the tight 3σ selection of the data. The expected jet fluctuation background is shown as the shaded area.*

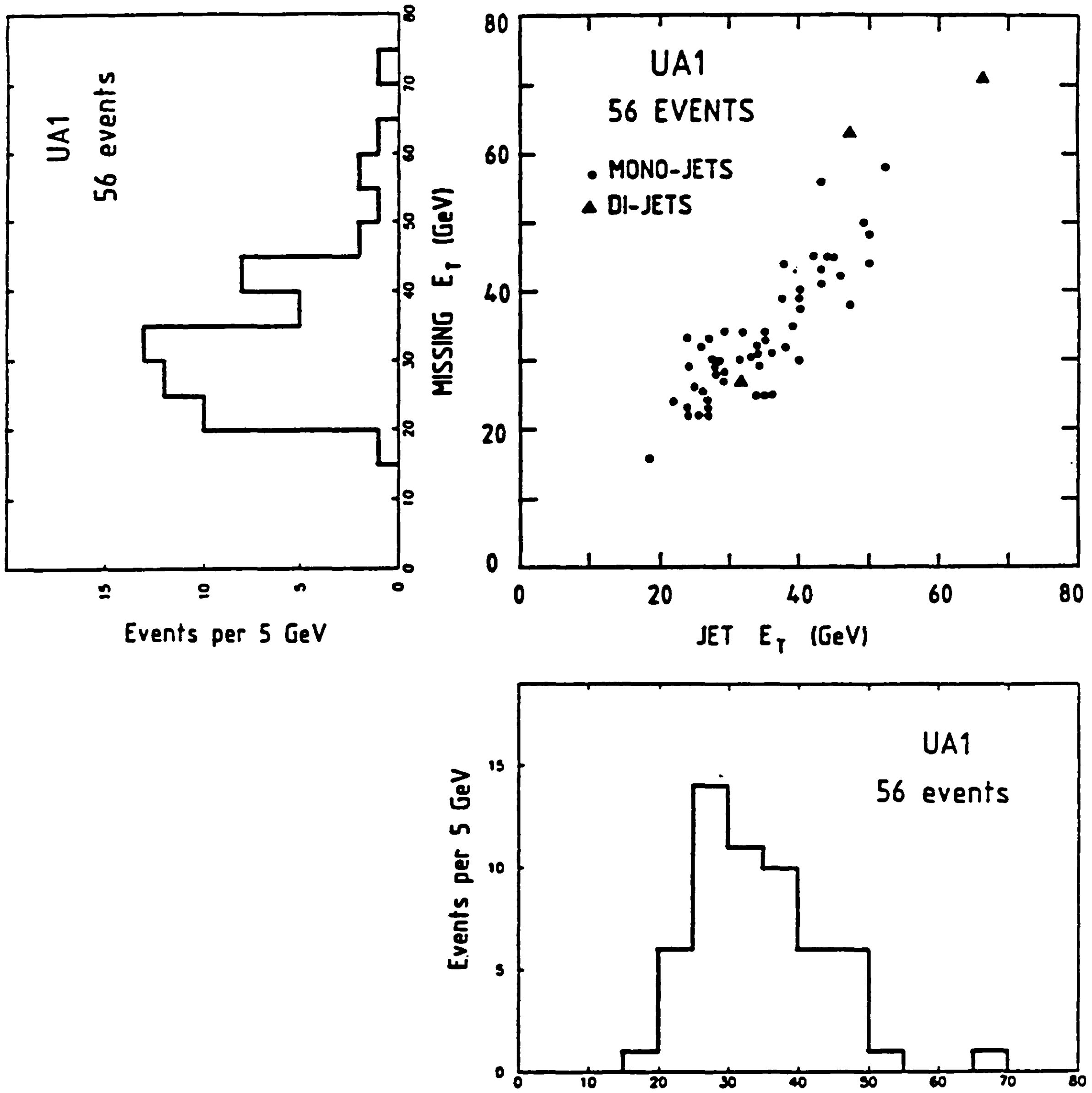

Figure (5.7) : *A scatter plot of the transverse energy of the highest* E_T *jet in the event versus the missing* E_T *of the event, for the* 4σ *data sample. Shown also are the projections.*

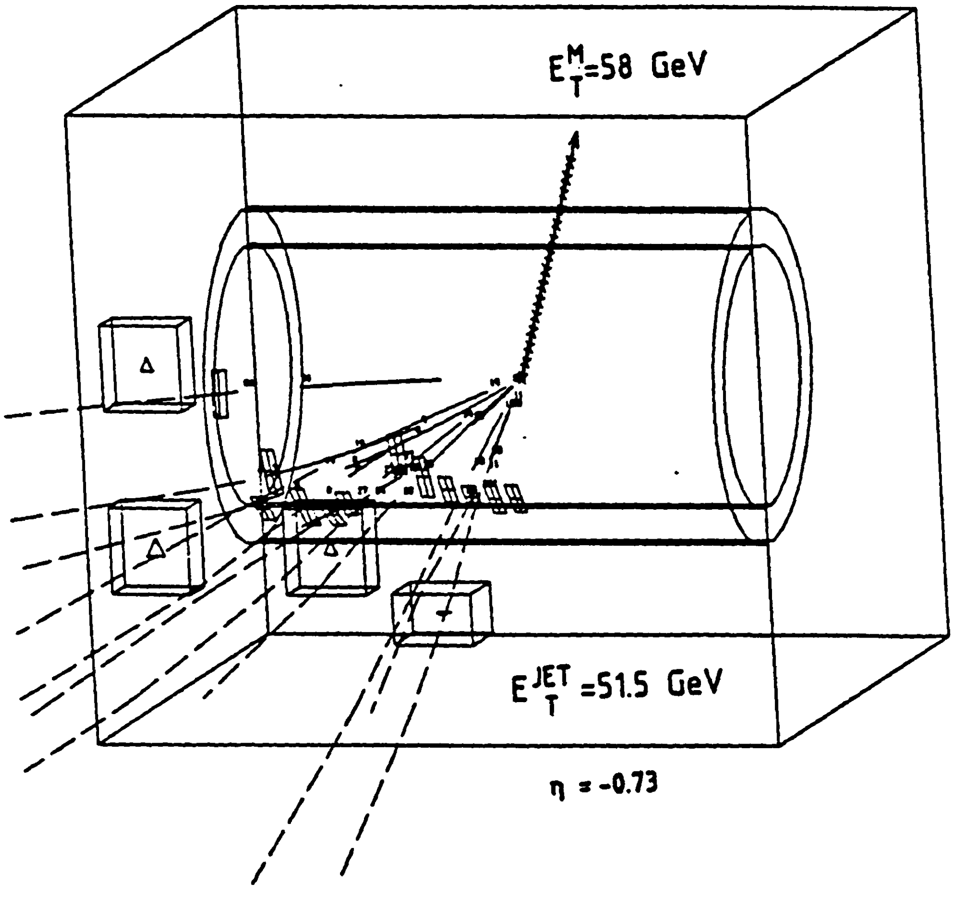

Figure (5.8) : *A display of the mono-jet event with the largest amount of missing transverse energy.*

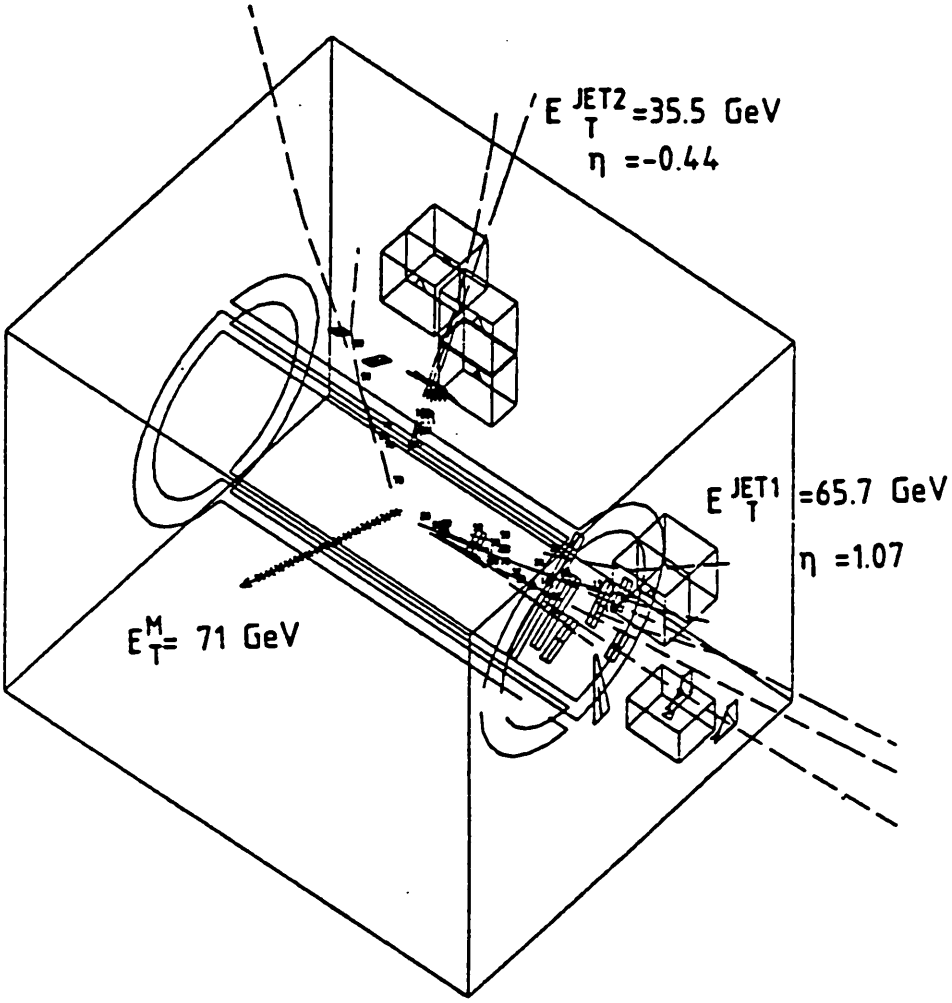

Figure (5.9) : *A display of the di-jet event with the largest amount of missing transverse energy.*

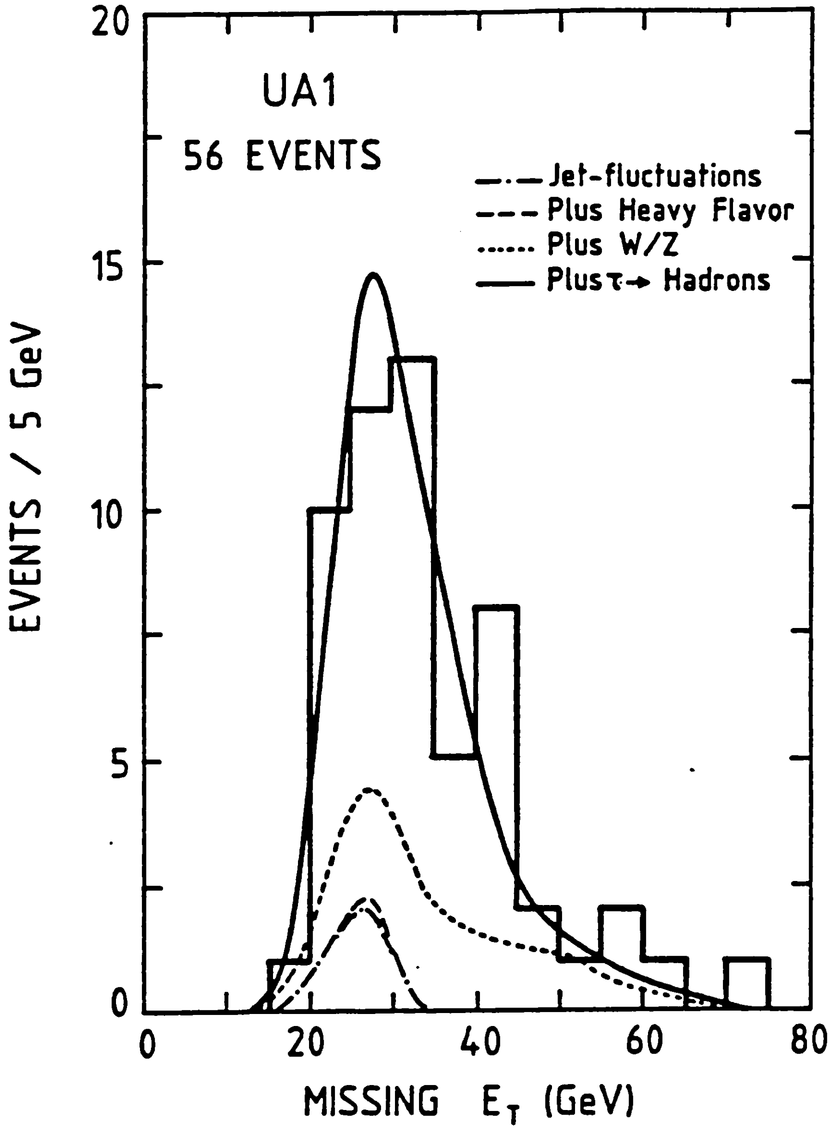

Figure (5.10) : *Distribution of the missing transverse energy for the 4σ data sample (histogram). Shown also (curves), cumulatively, are the contributions from the physics processes and jet fluctuation background.*

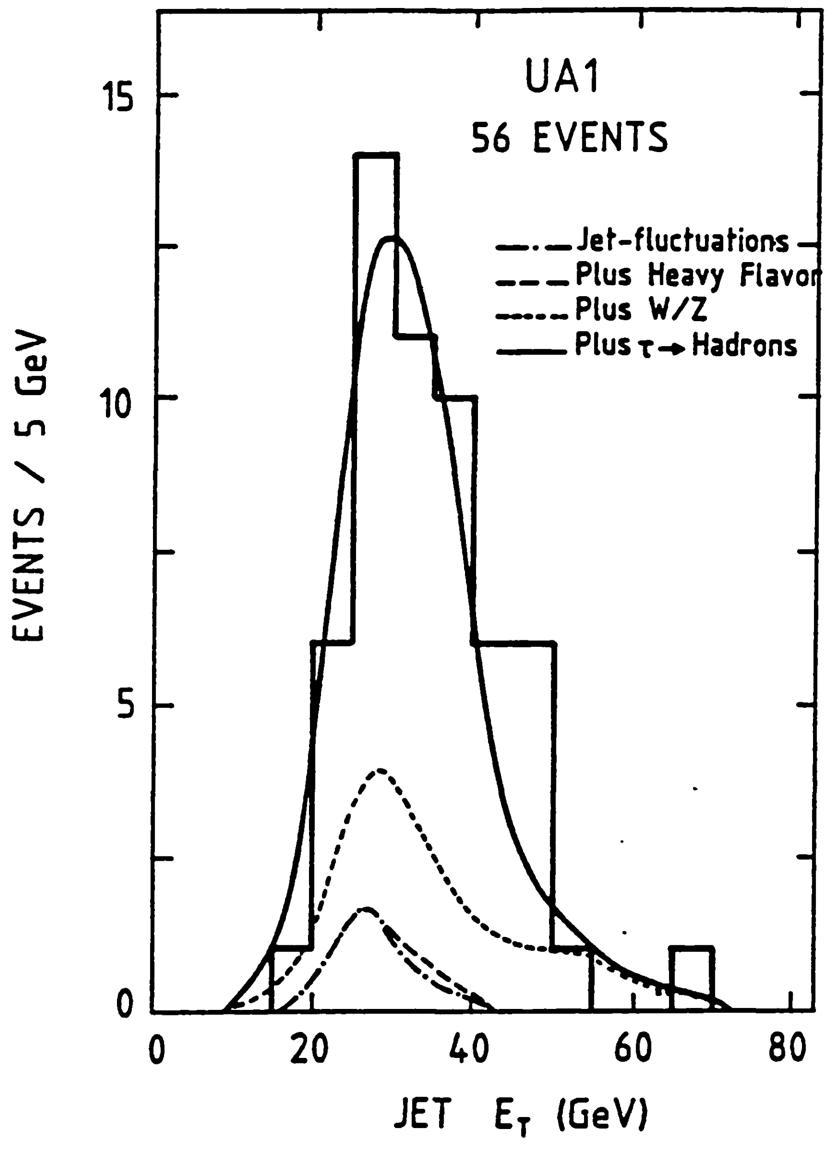

Figure (5.11) : *Distribution of the transverse energy of the highest E_T jet for the 4σ data sample. The curves show the cumulative contributions from physics and jet fluctuation backgrounds.*

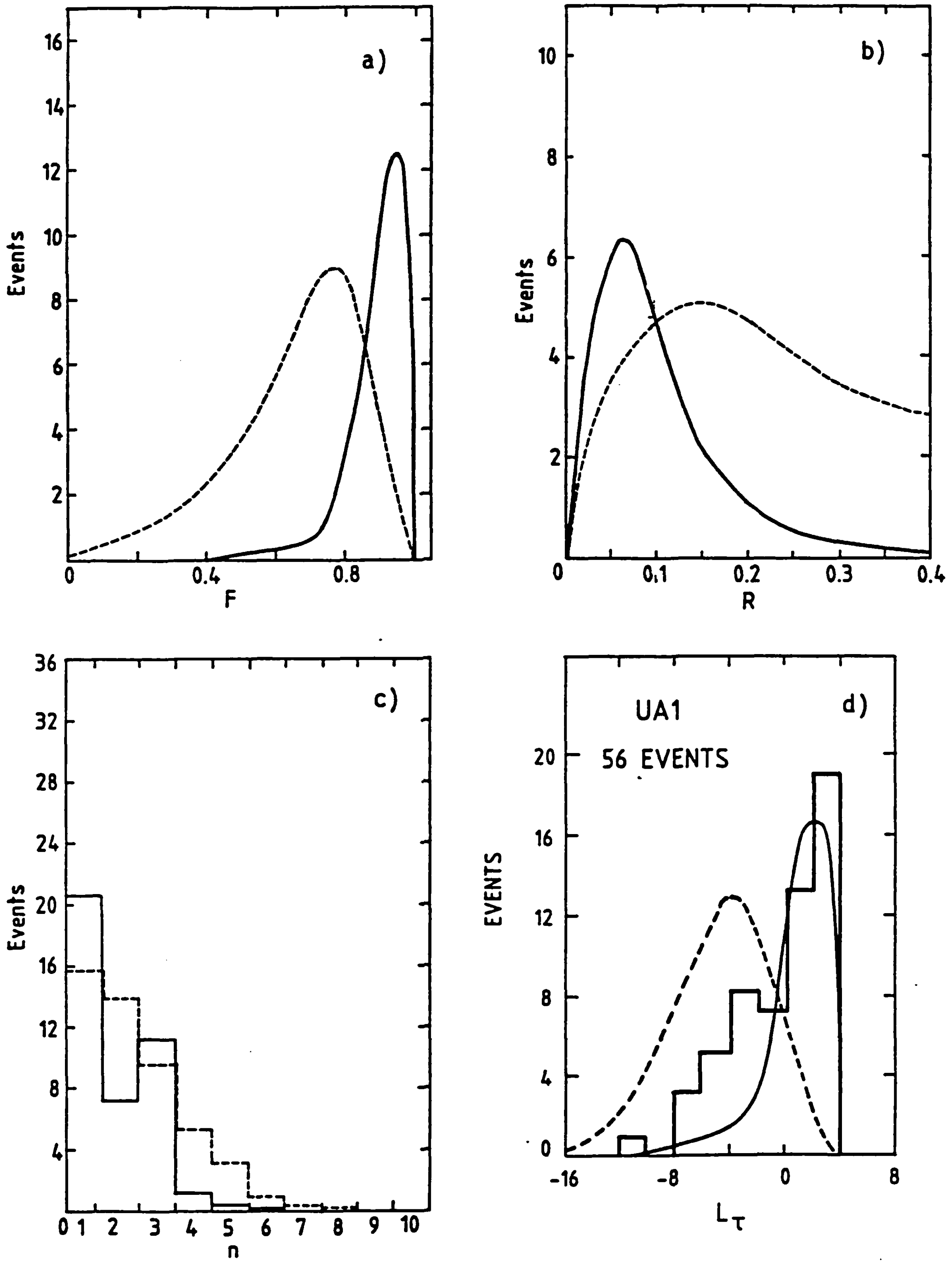

Figure (5.12) : *Distributions of the three variables : (a) F, (b) R, (c) n from the* τ *Monte Carlo (solid curve and full histogram). In (d) the* L_τ *distribution for the 56 events of the* 4σ *data sample(histogram) is compared with the* τ *--> hadrons Monte Carlo (solid curve) and also jet data(dashed curve).*

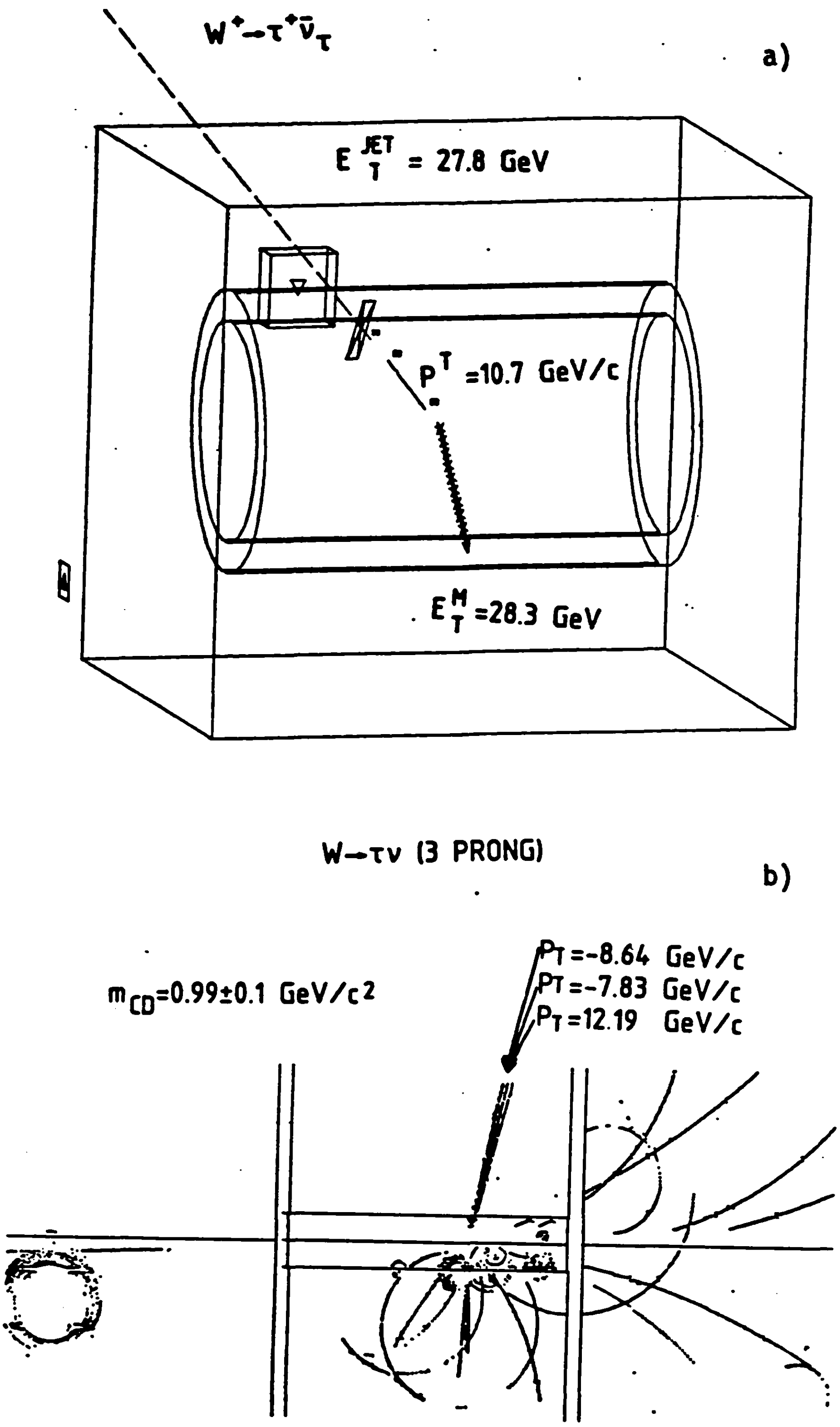

Figure (5.13) : *Graphics display of two events from the tau sample : (a) a one-prong and (b) a three-prong τ candidate. In (a) only charged tracks with $P_T > 1$ Gev/c and calorimeter cells with $E_T > 1$ Gev are displayed. In (b) all raw dizitisings recorded by the central drift chamber are shown.*

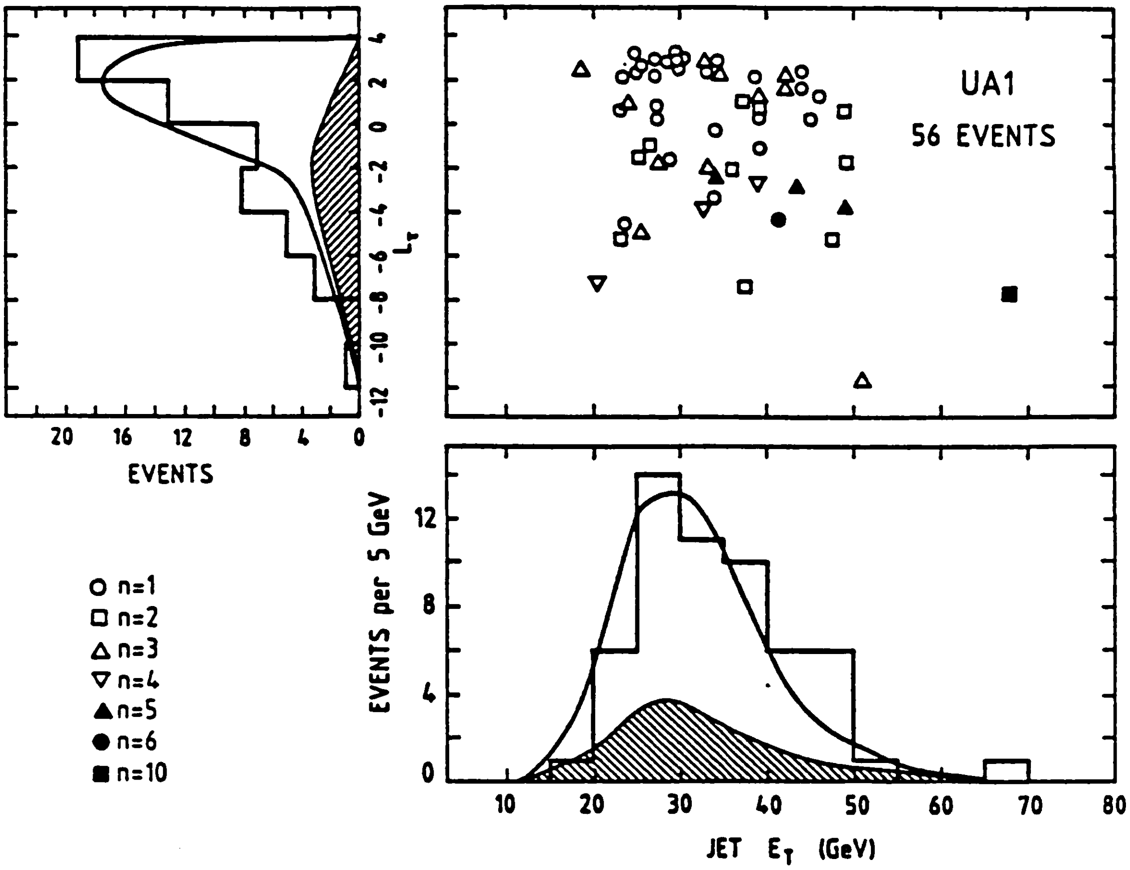

Figure (5.14) : *Scatter plot of* L_τ *versus* E_T^{jet} *(for the trigger jet) for the* 4σ *data sample. Charged track multiplicity of the jet is defined by the symbols shown. The total contribution (solid curve) and the non-*τ *contribution (shaded area) is shown in the projections.*

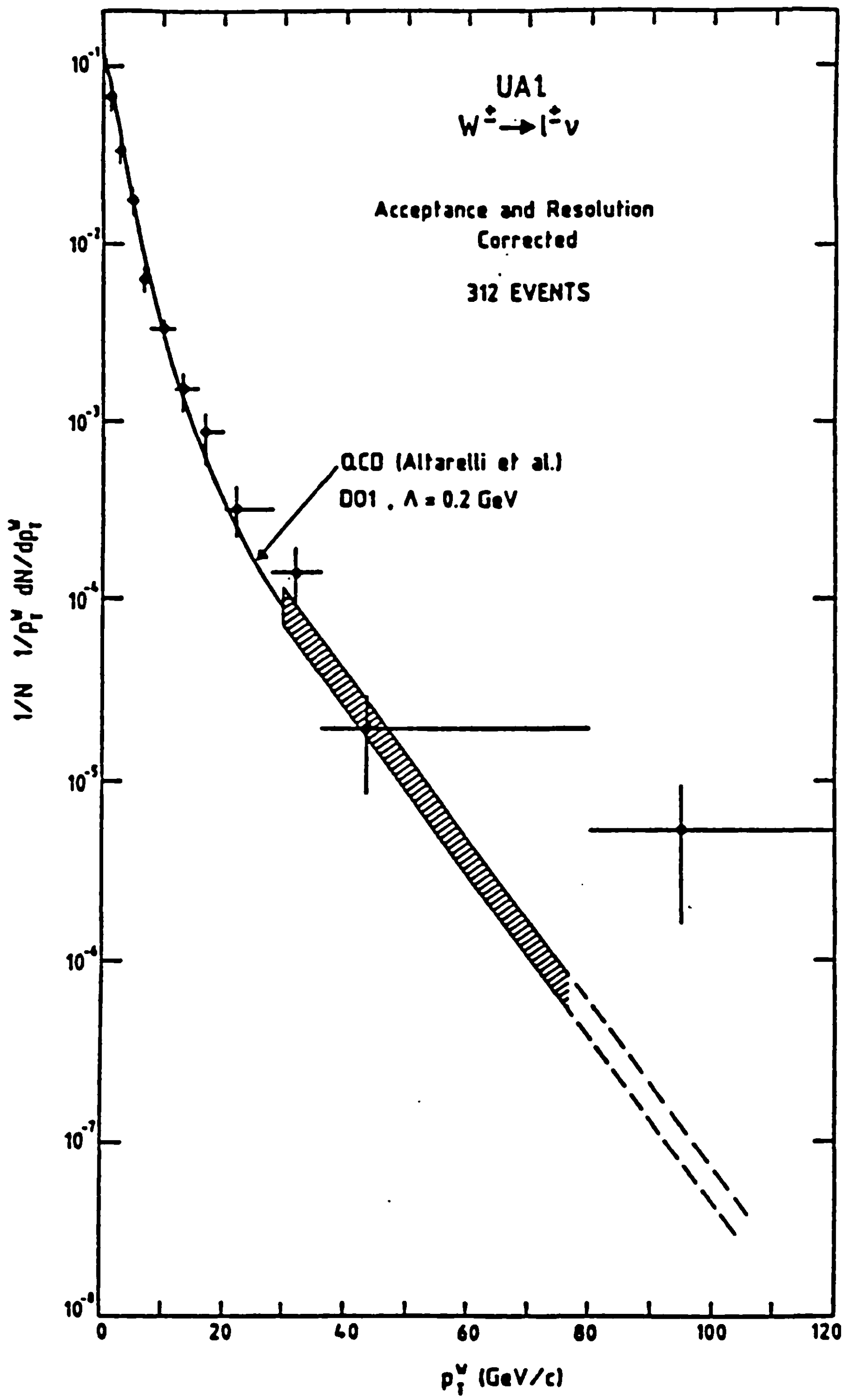

Figure (5.15) : *Transverse momentum distribution of W events. The curve is the QCD prediction of ref[47].*

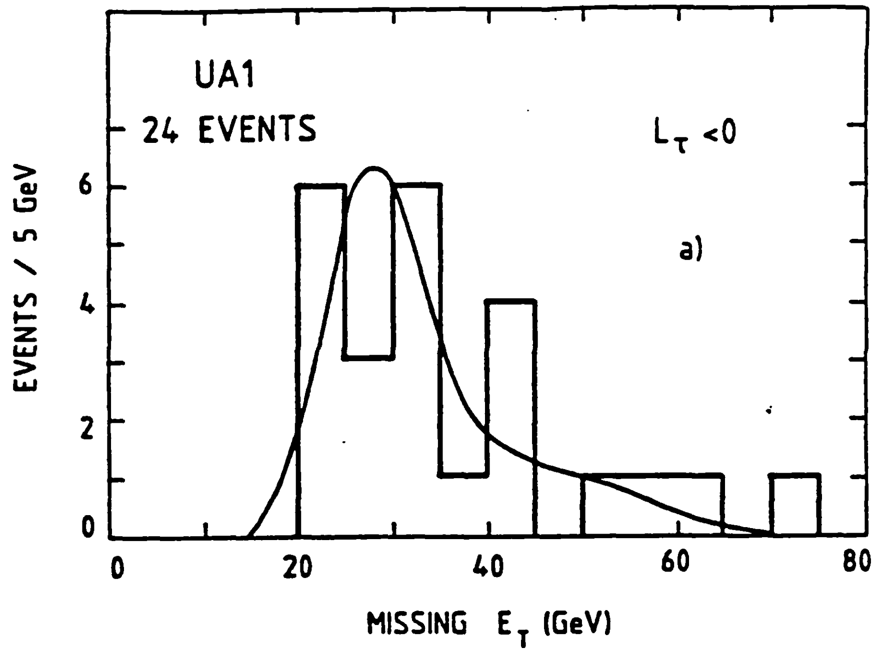

Figure (5.16) : *Missing transverse energy distribution for the non-τ data sample (histogram). The curve shows the Monta Carlo predictions.*

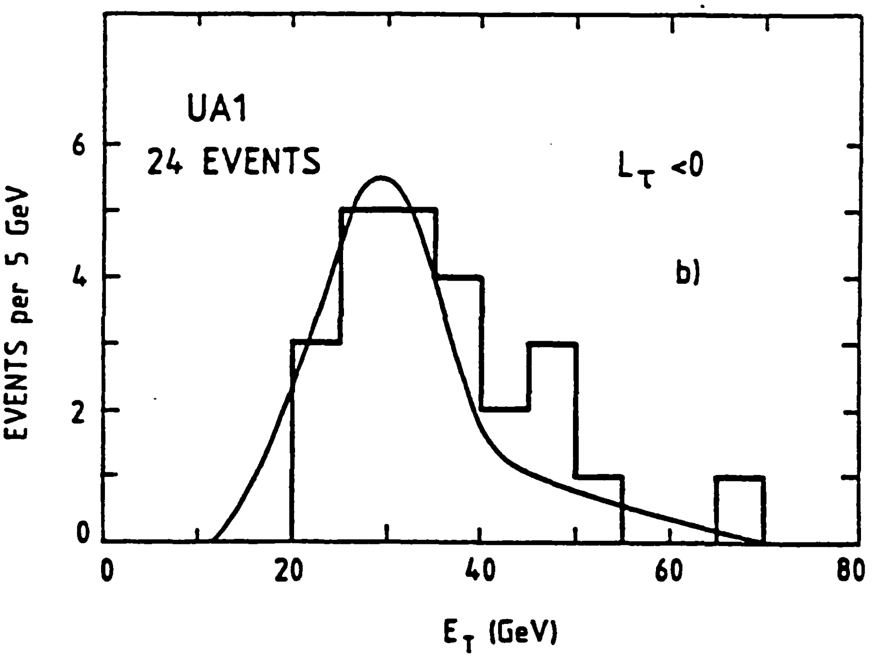

Figure (5.17) : E_T^{jet} *(for the highest* E_T *jet) distribution for the non-τ data sample(histogram). The curve shows the Monte Carlo prediction.*

Process	4σ–Data sample events	non – τ data sample events
W --> $e\nu$, $e\mu$ W --> $\tau\nu$ --> leptons	3.6	2.0
W/Z ---> heavy flavours	<0.1	< 0.1
Z --> $\tau\tau$	0.5	0.1
Z --> $\nu\nu$ (for three neutrino species)	7.4	7.1
W --> $\tau\nu$ --> $\nu\nu$ + hadrons	36.7	8.0
PP ---> cc, bb	0.2	0.2
Jet fluctuation	3.8	3.4
TOTAL	52.2	20.8
DATA	56	24
The errors on the total contributions		
Monte Carlo statistical error	2.5	2.0
PTW error	6.4	4.6
Systematic error	3.6	1.1

Table (5.1) : *Predicted contributions to the 4σ data sample from processes producing large missing transverse energy. Also shown are the numbers contributing to the $L_\tau < 0$ data sample.*

CHAPTER 6

MASS LIMITS ON THE SUPERSYMMETRIC PARTICLES

6.1 INTRODUCTION

In the past few years, there has been a tremendous effort [26] [48] to construct and to explore the phenomenological implications for N=1 supergravity models. This work has gained renewed interest with the discovery of anomaly-free superstring theories [49], which may possibly yield a candidate for a unified description of gravitational and Yang-Mills interactions. It has been shown[50] that their compactifications to four dimensions can lead to an N=1 supergravity theory in the low-energy limit.

Most supergravity models incorporate the existence of a conserved discrete symmetry called R parity (see chapter 1). The Standard Model particles : the fermions, higgs and gauge bosons are R even while their supersymmetric partners are R odd. The consequences of this are that the lightest supersymmetric particle is stable and all the supersymmetric particles decay into it plus one or several R even particles. Thus the nature of the lightest supersymmetric particle is crucial to the expected experimental signatures for the supersymmetric processes. The lightest supersymmetric particle is expected to be electrically and colour neutral and will therefore have a very small interaction cross section, of the same order as the neutrino cross section. As a result it will escape detection and carry away missing energy.

The scalar masses are expected to be ~100 GeV and in supergravity models with $M_{\gamma} \ll M_W$ there arise mass eigenstates W and Z in the gauge-higgs-fermion sector possessing the same internal quantum numbers as the W and the Z bosons but which are lighter [51] than the corresponding boson. If the photino is assumed to be the lightest supersymmetric particle (cosmologically favoured) then signatures for supergravity most readily accessible come from the decay into gauginos pairs of the intermediate vector bosons :

$$W \longrightarrow \tilde{W}\tilde{\gamma},\ \tilde{W}\tilde{Z}$$

$$Z \longrightarrow \tilde{W}^{+}\tilde{W}^{-}$$

The winos and the zinos subsequently decay via the processes :

$$\tilde{W} \longrightarrow l\nu\tilde{\gamma} \quad \text{or} \quad q\bar{q}'\tilde{\gamma}$$

$$\tilde{Z} \longrightarrow l\bar{l}\tilde{\gamma} \quad \text{or} \quad q\bar{q}\tilde{\gamma}$$

This results in events which are characterised by multijet and/or multi-lepton topologies with missing transverse energy.This analysis will , however, concentrate on the hadronic decay modes leading to the jets + missing transverse energy signature.
As yet no evidence has been found for the existence of supersymmetric partners for the ordinary particles. All the experimental searches have led to limits on the masses of these particles, which are summarised in table (6.1).

6.2 THE SUPERSYMMETRIC MODEL

The Model used is that of Baer et. al[52] , it incorporates the following principle assumptions :

- conservation of R - parity.

- The couplings of the gauge and higgs fermions to the electroweak gauge bosons are completely determined by $SU(2)_L \times U(1)_Y$ and supersymmetry. The gauge and higgs fermions of the same charge mix to form the mass eigenstates once $SU(2)_L \times U(1)_Y$ is broken.

- The lightest supersymmetric particle is taken to be the photino. Intially a massless photino is assumed but variation of the limits with a massive photino is also investigated.

- The vacuum expectation values of the two higgs fields that occur in all minimal supersymmetry models are taken to be equal (v=v'). This results in the squarks and sleptons being degenerate in mass.

6.2.1 PRODUCTION OF THE GAUGINOS

Figure(6.1) shows the lowest order Feynman diagrams that contribute to gaugino pair production at hadron colliders. The diagrams 6.1g and 6.1h have a very low cross section (< 1 pb for $M_{\tilde{q}} > 100$ GeV) and can be ignored. The t-channel squark exchange processes 6.1b, 6.1c, 6.1e, 6.1f can also be ignored. The cross-sections for the production of $\tilde{W}\tilde{\gamma}$, $\tilde{W}\tilde{W}$, $\tilde{W}\tilde{Z}$ have dominant contributions from W, Z resonance production, diagrams 6.1a and 6.1d are the only ones that significantly contribute.
The gaugino production cross-sections can then be easily calculated using the measured W --> eν and Z --> e^+e^- rates. These cross-sections are calculated as follows :

$$\sigma.B\,(W \longrightarrow \tilde{W}\tilde{\gamma}) = \frac{\sigma_W^{tot}\,.\,\Gamma\,(W \longrightarrow \tilde{W}\tilde{\gamma})}{\Gamma_W^{tot}} \qquad (6.1)$$

now since

$$\sigma.B\,(W \longrightarrow e\nu) = \frac{\sigma_W^{tot}\,.\,\Gamma\,(W \longrightarrow e\nu)}{\Gamma_W^{tot}} \qquad (6.2)$$

one obtains for the W —> $\tilde{W}\tilde{\gamma}$, $\tilde{W}\tilde{Z}$ processes

$$\sigma.B\,(W \longrightarrow \tilde{W}\tilde{\gamma}, \tilde{W}\tilde{Z}) = \sigma.B\,(W \longrightarrow e\nu)\,.\,\frac{\Gamma\,(W \longrightarrow \tilde{W}\tilde{\gamma}, \tilde{W}\tilde{Z})}{\Gamma\,(W \longrightarrow e\nu)} \qquad (6.3)$$

also for the process $Z \longrightarrow \tilde{W}^+ \tilde{W}^-$

$$\sigma.B\,(Z \longrightarrow \tilde{W}^+\tilde{W}^-) = \sigma.B\,(Z \longrightarrow e^+e^-).\frac{\Gamma\,(Z \longrightarrow \tilde{W}^+\tilde{W}^-)}{\Gamma\,(Z \longrightarrow e^+e^-)} \qquad (6.4)$$

Where $\sigma.B\,(W \longrightarrow e\,\nu)$ and $\sigma.B\,(Z \longrightarrow e^+e^-)$ are taken from measurements at UA1, and are 0.63 and 0.074 respectively, while $\Gamma\,(W \longrightarrow e\,\nu)$ and $\Gamma(Z \longrightarrow e^+e^-)$, the partial widths of the W and the Z, are taken to be 0.22 and 0.087 respectively from electroweak theory.

The partial width of the W, Z into a pair of gauginos is given by [53],

$$\Gamma\,(X \longrightarrow \tilde{\alpha}\tilde{\beta}) = \frac{1}{3}M_X\,\alpha\sqrt{\lambda\,(1, X_{\tilde{\alpha}}, X_{\tilde{\beta}})}\;\Big\{\,(g_V^2 + g_A^2)\Big[1 - \frac{1}{2}X_{\tilde{\alpha}} - \frac{1}{2}X_{\tilde{\beta}} - \frac{1}{2}(X_{\tilde{\alpha}} - X_{\tilde{\beta}})^2\Big] + 3\,(g_V^2 - g_A^2)\,(X_{\tilde{\alpha}}X_{\tilde{\beta}})^{1/2}\Big\} \qquad (6.5)$$

Where the process $X \longrightarrow \tilde{\alpha}\,\tilde{\beta}$ can be $W \longrightarrow \tilde{W}\tilde{\gamma}$, $\tilde{W}\tilde{Z}$ or $Z \longrightarrow \tilde{W}^+\,\tilde{W}^-$, and

$$X_{\tilde{\alpha}} = \Big[\frac{m_{\tilde{\alpha}}}{M_X}\Big]^2, \quad X_{\tilde{\beta}} = \Big[\frac{m_{\tilde{\beta}}}{M_X}\Big]^2$$

$$\lambda\,(1, X_{\tilde{\alpha}}, X_{\tilde{\beta}}) = 1 + X_{\tilde{\alpha}}^2 + X_{\tilde{\beta}}^2 - 2X_{\tilde{\alpha}} - 2X_{\tilde{\beta}} - 2X_{\tilde{\alpha}}X_{\tilde{\beta}} \qquad (6.6)$$

$$\text{and } \alpha = \frac{1}{128}\,.$$

and g_V and g_A are the vector and axial-vector couplings of the gauginos $\tilde{\alpha}$, $\tilde{\beta}$ to the gauge bosons.

The couplings can be obtained from the gaugino part of the full lagrangian. This takes the general form :

$$L_{gaugino} = eX_{\mu} \{ g_V \tilde{\beta} \gamma^{\mu} \tilde{\alpha} + g_A \tilde{\beta} \gamma^{\mu} \gamma^{5} \tilde{\alpha} \} \qquad (6.7)$$

for each process $X \longrightarrow \tilde{\alpha}\, \tilde{\beta}$,

The specific form is given in appendix(A) together with all the general expressions for the couplings. All the couplings can be evaluated completely in terms of two free parameters : the mass of the wino and the mass of the photino.

In the massless photino scenario the masses of the lighter wino and zino states are given by :

$$m_{(-)} = \left| \left(m_1^{(0)\,2} + M_W^2 \right)^{1/2} - m_1^{(0)} \right| \qquad (6.8)$$

$$\mu_{(-)} = \left| \left(m_1^{(0)2} + M_Z^2 \right)^{1/2} - m_1^{(0)} \right| \qquad (6.9)$$

respectively. Where $m_1^{(0)}$ is defined in appendix(A) and M_W and M_Z are the masses of the intermediate vector bosons.

In the massive photino scenario however the masses of the lighter wino and zino states are given by :

$$M_{\tilde{W}(-)} = \left| \left[\left(m_1 - \frac{\mu_2}{2} \right)^2 + M_W^2 \right]^{1/2} - \left(m_1 + \frac{\mu_2}{2} \right) \right| \qquad (6.10)$$

$$M_{\tilde{Z}(-)} = \mu_{(-)} + \frac{\mu_{(+)}}{\mu_{(+)} + \mu_{(-)}} \left| \mu_2 \cos^2\theta_W + \mu_1 \sin^2\theta_W \right| \qquad (6.11)$$

respectively, where m_1 , μ_1, μ_2, $\mu_{(-)}$ and $\mu_{(+)}$ are defined in appendix(A). The variation of zino mass with wino mass is shown in figure(6.3).

6.2.2 DECAY OF THE GAUGINOS

Figure(6.2) shows the lowest order Feynman diagrams which contribute to the decay of the wino and the zino.When the Sfermions (squarks and sleptons) are heavier than the wino, which is the case under study, it decays into a photino and a pair of light fermions :

$$\tilde{W}^- \longrightarrow \tilde{\gamma} + f + \bar{F} \qquad (6.12)$$

$$\tilde{W}^+ \longrightarrow \tilde{\gamma} + \bar{f} + F \qquad (6.13)$$

Where (f , F) can be either (d,u) , (s,c) or (l,ν_l) with $l = e, \mu, \tau$.
The Decay mode $\tilde{W}^- \longrightarrow \tilde{\gamma}\, b\, t$ is assumed to be forbidden. The Feynman diagrams that contribute to the wino decay are shown in figures (6.2i)-(6.2k).
The zino has three decay modes :

$$\tilde{Z} \longrightarrow \tilde{\gamma} + f + \bar{f} \qquad (6.14)$$

$$\longrightarrow \tilde{W}^- + F + \bar{f} \qquad (6.15)$$

$$\longrightarrow \tilde{W}^+ + \bar{F} + f \qquad (6.16)$$

The decay (6.14) always occurs since the photino is assumed to be light and the other two occur in the supergravity model being used with $m_{\tilde{\gamma}} << M_W$ and v=v', since the wino is always lighter than the zino.
Figures (6.2l) and (6.2m) contribute to the decay $\tilde{Z} \longrightarrow \tilde{\gamma} f \bar{f}$ and the diagrams in figures (6.2n) to (6.2p) contribute to the decay $\tilde{Z} \longrightarrow \tilde{W}^- F \bar{f}$.
The decay $\tilde{Z} \longrightarrow \tilde{\gamma} f \bar{f}$ is allowed for five light quarks and three charged lepton flavours. The $\tilde{Z} \longrightarrow \tilde{W}^- F \bar{f}$ decay is allowed for two light families of quarks (f , F) = (d, u), (s, c) and three light families of leptons (l, ν) . For the wino decay the leptonic branching fraction is 1/9 per lepton flavour for three lepton flavours. For the $\tilde{Z}$ decay, however, unless $m_{\tilde{q}}(\approx m_{\tilde{l}})$ exceeds ≈350 GeV/c^2 the $\tilde{W}$ mode is suppressed relative to the $\tilde{\gamma}$ mode. The $\tilde{Z} \longrightarrow \tilde{W}^- F \bar{f}$ mode has therefore been neglected. So the leptonic branching

fraction for the $\tilde{Z} \longrightarrow \tilde{\gamma} f \bar{f}$ mode is 13% per lepton flavour for three lepton generations.

6.3 SIMULATION OF THE SUPERSYMMETRIC PROCESSES

Since the 4σ - Isolated missing transverse energy data sample was used to derive limits on the supersymmetric processes, only the hadronic decay modes of the wino and the zino were simulated. These tend to produce events that contain a substantial amount of missing transverse energy with associated jet activity and therefore contribute to the 4σ - data sample. The Leptonic decay signal was not considered (a leptonic decay rate is 1/6 of the semi-hadronic decay rate).

In this analysis a modified version of the ISAJET Monte-Carlo program was used to study the properties and to calculate the rates of the supersymmetric processes.

The following processes were simulated :

$$p + \bar{p} \longrightarrow W, Z$$

then :

$$W \longrightarrow \tilde{W}\tilde{\gamma}\,,\ \tilde{W}\tilde{Z} \longrightarrow q\,\bar{q}\,\tilde{\gamma}$$

$$\tilde{W} \longrightarrow q\,\bar{q}'\,\tilde{\gamma}$$

$$\tilde{W} \longrightarrow q\,\bar{q}'\,\tilde{\gamma}$$

and

$$Z \longrightarrow \tilde{W}\ \ \tilde{W}$$

$$\tilde{W} \longrightarrow q\,\bar{q}'\,\tilde{\gamma}$$

$$\tilde{W} \longrightarrow q\,\bar{q}'\,\tilde{\gamma}$$

ISAJET was modified so that the decay of the W or the Z was not according to V-A. Since the winos and the zinos do not have V-A couplings to the intermediate vector bosons, these are set to decay isotropically into the supersymmetric particles. Once the processes $W \longrightarrow \tilde{W}\tilde{\gamma}, \tilde{W}\tilde{Z} \longrightarrow q\bar{q}'\tilde{\gamma}\tilde{\gamma},\ q\bar{q}'q\bar{q}\tilde{\gamma}\tilde{\gamma}$ or $Z \longrightarrow q\bar{q}'q\bar{q}'\tilde{\gamma}\tilde{\gamma}$ are generated , QCD radiation from the initial and final partons is added and the generated quarks, gluons and the spectator beam partons are hadronized. The particles emerging from this process are then decayed according to standard ISAJET. Once this is complete the events are passed through the same UA1 detector and trigger simulation programs as were the physics background Monte-Carlo processes.

The number of events predicted, for each simulated process (see section 6.4), to contribute to the isolated $4\sigma - E_T^{miss}$ sample is then given by

$$N_{process} = \int L\,dt \times \sigma.B(\,process)_{had} \times \left\{\frac{N_{seen}}{N_{Gen}}\right\} \qquad (6.17)$$

Where $N_{process}$ is the number of events for the particular process predicted to contribute to the isolated $4\sigma - E_T^{miss}$ sample.

$\int L\,dt$ is the total integrated luminosity collected by the experiment.

$$\sigma.B(\,process)_{had} = \sigma.B(\,process) \times \frac{2}{3} \quad ,$$

The σ.B(process) is calculated from (6.3) or (6.4) depending on the process, and the appropriate partial widths needed in (6.3) or (6.4) are taken from (6.5) and the appropriate couplings from appendix(A).

The fraction 2/3 is the hadronic branching fraction.

N_{seen} is the number of events seen by the detector and incorporates the trigger and selection efficiencies.

N_{Gen} is the number of events generated for the process.

6.4 RESULTS FOR THE MASSLESS PHOTINO SCENARIO

The couplings in this case simplify and are summarised in table(6.2), see also appendix(A). The cross-sections for the three processes $W \longrightarrow \tilde{W}\tilde{\gamma}$, $\tilde{W}\tilde{Z}$ and $Z \longrightarrow \tilde{W}^+\tilde{W}^-$, for massless photino as a function of the wino mass, were obtained by calculating the partial width in each case. Figure (6.4) shows a plot of the partial width of the $\tilde{W}\tilde{\gamma}$ decay mode of the W normalised to its eν mode. As the wino becomes more massive, the purely vector coupling, g_V, decreases as does the phase space available to the decay. This is reflected in the behaviour of the width. Similar behaviour is shown in figure(6.5) for the $\tilde{W}\tilde{Z}$ width and in figure(6.6) for the normalised $\tilde{W}\tilde{W}$ decay mode of the Z. They are all shown as functions of wino mass.

6.4.1 PROPERTIES OF THE MASSLESS PHOTINO EVENTS

The three processes $\tilde{W}\tilde{\gamma}$, $\tilde{W}\tilde{Z}$ and $\tilde{W}^+\tilde{W}^-$ were generated using the ISAJET Monte-Carlo program. For the wino-photino process 9 samples of 1000 events each were generated for each of the following wino masses : 20, 30, 35, 40,45, 50, 55, 60, 70 GeV/c^2. For the wino-wino process 6 samples of 1000 events were generated for wino masses : 20,30,35, 40, 45, 50 GeV/c^2; and finally for the wino-zino process 5 samples of 1000 events each were generated for the following wino masses : 20, 30, 35, 40, 45 GeV/c^2.We look first at the effects of the trigger cuts on the Monte-Carlo events (a large fraction of events are lost because of not triggering the detector). For low wino masses eg. $M_{\tilde{W}}$ = 20 GeV/c^2 the trigger efficiency is approximately 30%. As the wino mass increases the trigger efficiency increases because of the increasing number of jet triggers. In order to be able to study the effects of the selection cuts and to reduce the excessive amount of simulation time required, a minimium missing transverse energy requirement was imposed on the events before the simulation stage. The events were required to possess $E_T^{miss} > 15$ GeV and $N_\sigma > 2.5$. In figure(6.7) can be seen the E_T^{miss} distribution for the $M_{\tilde{W}}$ = 20 GeV/c^2 and $M_{\tilde{W}}$ = 50 GeV/c^2 wino-photino samples, and in figure(6.8) is shown the N_σ distributions for these two samples. As the wino becomes heavier there is a drop in the missing transverse energy generated in the event. This leads to approximately 55% of the mass of wino 20 GeV/c^2 events passing the minimal E_T^{miss} >15 GeV + $N_\sigma > 2.5$ cut while 47% of the mass of wino 50 GeV/c^2 events pass this cut. With increasing mass of the wino a greater fraction of the events possess a multijet topology ; eg. for mass of wino 20 GeV/c^2 77% of the events are monojets and 17% are multijets while for mass of wino 50 GeV/c^2 67% are monojets and 30% are multijets. The heavier wino tends to decay more isotropically leading to a larger opening angle between the two quark jets. The UA1 jet algorithm then resolves two jets of lower energy. Figure (6.9) shows a softer transverse energy distribution for the trigger jet in the mass of wino 50 GeV/c^2 sample as compared to the mass of wino 20 GeV/c^2 sample. Figure(6.10) shows that these supersymmetric process do not possess a topology similiar to that expected from taus.

For the $\tilde{W}^+\tilde{W}^-$ process there is a different configuration. As the mass of the wino increases from 20 to 50 GeV/c^2 there is an increase in the missing transverse energy, resulting in 25% of the mass of wino 20 GeV/c^2 sample passing the E_T^{miss} >15 GeV + N_σ > 2.5 cut while 43% of the mass of wino 50 GeV/c^2 sample pass the same cut. Figure (6.11)

shows the missing transverse energy for these two samples after the minimal cut has been imposed, and in figure(6.12) is shown the N_σ distributions.
For a light wino, the two winos emerging from the decay of the Z will have relatively higher transverse momentum but are produced more back-to-back. This will decrease the missing transverse energy that the photinos can generate. With increasing wino mass, the subsequent decay of the winos is more isotropic and therefore leads to a greater missing transverse energy and a softer E_T distribution for the trigger jet (see figure(6.13)). The wino-zino process has a similiar topology as the wino-wino process, see figures(6.14), (6.15) and (6.16) for the E_T^{miss}, N_σ and E_T of the highest transverse energy jet, distributions respectively for mass of wino 20 GeV/c^2 and mass of wino 45 GeV/c^2 samples of the wino-zino events.

6.4.2 THE WINO MASS LIMIT FOR THE MASSLESS PHOTINO SCENARIO

The good agreement between the non - tau data sample and the expectations from Standard Model physics processes and the other backgrounds that contribute to this data sample, enables one to set limits on new physics processes that contribute. Since the Monte-Carlo predictions in the region of $E_T^{jet} > 40$ GeV are plagued by large uncertainties from the tail of the P_T^W distribution and since the supersymmetry events predominantly populate the $E_T^{jet} < 40$ GeV region, only those events having jets with transverse energy less than 40 GeV are considered when deriving a limit for the wino mass.
In the 4σ - isolated missing transverse energy data sample with $L_\tau < 0$ (the non- tau data sample) and $E_T^{jet} < 40$, there are 17 events. The physics background Monte-Carlo simulated processes predict $17.8 \pm 3.7 \pm 1.0$ events , the first error is statistical and the second is the systematic one. Table(6.3) contains the contributions from the individual physics processes that contribute to the $L_\tau < 0 + E_T^{jet} < 40$ GeV sample along with the statistical and systematic errors. Table(6.4) contains the total contributions from the three supersymmetric processes under study, and in table(6.5) are the shown individual contributions from these processes.
A polynomial was fitted to the rates for the nine wino masses generated, in order to allow a calculation of the rates in the mass range from 20 GeV/c^2 to 70 GeV/c^2. This is shown in figure(6.17) and the rates for the three individual processes are shown in figure(6.17). The errors were extrapolated similarly.
Using the statistical method described in appendix(B), the total background physics and the total supersymmetry rates as a function of wino mass we derive a limit on the wino mass of (47 ± 2) GeV/c^2 .

After inclusion of the systematic errors the lower limit on the mass of the wino for a massless photino is :

$$M_{\tilde{W}} > 45 \ \mathrm{GeV}/c^2 \qquad (90\% \ \mathrm{CL})$$

This drops to 42 GeV/c^2 at 95% CL.

6.5 RESULTS FOR THE MASSIVE PHOTINO SCENARIO

To explore the possibility of the existence of a massive photino and to investigate its effects on the wino mass limit, further samples were generated. For a photino of mass 10 GeV/c^2, five samples of 1000 events each were generated at wino masses : 20, 35, 40, 50 and 60 GeV/c^2 V. For a photino mass of 20 GeV/c^2 five samples of 1000 events each were generated at wino masses : 30, 35, 40, 50 and 60 GeV/c^2. Where possible, all three supersymmetric processes were generated for each wino mass. Finally, six samples of 2000 events each were generated for wino masses : 10, 20, 25, 30, 35, 40 with the photino mass lower by 3 GeV/c^2 than the wino mass. For the calculation of the events rates the appropriate couplings are taken from appendix (A). These are a function of the mass of the wino and the mass of the photino. In figures (6.4), (6.5) and (6.6) can be seen how the normalised width changes for all three supersymmetric processes with increasing photino mass. In figure(6.4) the normalised width, for low wino masses, decreases with increasing photino mass, because of a sharp decrease in the vector coupling, g_V, for low wino masses. In figure(6.5) it can be seen that the $\tilde{W}\tilde{Z}$ partial width of the W decreases rapidly, as the photino becomes heavier. Even though g_V increases with wino mass, the limited phase space available for the decay of the W into a wino-zino pair, since the mass of the zino increases rapidly with photino mass(for massless photino and mass of wino 40 GeV/c^2 the zino mass is 48 GeV/c^2, while for a photino of mass 20 GeV/c^2 and a wino of mass 40 GeV/c^2 the mass of the zino rises to 73 GeV/c^2 , see figure(6.3)), ensures that this normalised width is negligible for a photino mass of 20 GeV/c^2 and the generated wino masses.

6.5.1 PROPERTIES OF THE MASSIVE PHOTINO EVENTS

To effect a reduction in the time required for simulation and as an aid to the study of the selection cuts, a minimal selection cut of E_T^{miss} >15 GeV + N_σ > 2.5 was applied to all these samples.

For the process in which a W decays to a wino-photino pair, as the mass of the photino increases it is emitted with a smaller transverse momentum and will therefore be able to generate less missing transverse energy. This is reflected in the fact that for the mass of wino 20 GeV/c^2 and massless photino sample, 55% of the events pass the minimal E_T^{miss} >15 GeV + N_σ > 2.5 cut while for the mass wino 20 GeV/c^2 and mass of photino 17 GeV/c^2 sample only 14% do. Also figure(6.18) shows a softer missing transverse energy distribution for the mass of wino 20 GeV/c^2 and mass of photino 17 GeV/c^2 sample. The N_σ distribution is shown in figure(6.19). For the heavier photino samples the transverse momentum of the wino will be reduced from the decay of the W and this will result in a softer distribution for the transverse energy of the trigger jet, as can be seen in figure(6.20).

For the wino-wino process, as the mass of the photino increases again the missing transverse energy in the events will decrease. This can be seen in figure(6.21) showing the missing transverse energy distributions . With increasing photino mass the decay of the wino into two quarks and a photino will become more isotropic in the laboratory frame, resulting in less events failing the back-to-back cuts : 70% of the mass of wino 20 GeV/c^2 and massless photino sample fail these cuts while 35% of the mass of wino 20 GeV/c^2 and mass of photino 17 GeV/c^2 fail. The transverse energy of the trigger jet falls with increasing photino mass, see figure(6.23).

We were unable to set a limit using the samples in which the wino-photino were of nearly equal mass, because with such a massive photino the E_T^{miss} cuts preferentially selected events resulting from Ws with large P_T^W. This can be seen in figures(6.24) and (6.25), which show the P_T^W spectrum before and after an E_T^{miss} cut for one sample. This resulted in the events having associated with them a prohibitively large error from the uncertainty in the P_T of the Ws.

6.5.2 THE WINO MASS LIMIT FOR THE MASSIVE PHOTINO SCENARIO

Table(6.6) contains the total predicted events rates contributing to the non-tau data sample from the three supersymmetric processes; $W \longrightarrow \tilde{W}\tilde{\gamma}$, $\tilde{W}\tilde{Z}$ and $Z \longrightarrow \tilde{W}^+\tilde{W}^-$ for a photino of mass 10 GeV/c^2, while table(6.7) contains the individual contributions of these supersymmetric processes.

A polynomial was again fitted for the five wino masses and figure(6.26) shows the event rates for the mass of photino 10 GeV/c^2 as a function of wino mass, shown also are the rates for each supersymmetric process separately.

Table(6.8) contains the total predicted event rates for the mass of photino 20 GeV/c^2 samples from all the supersymmetric processes, and table(6.9) contains the breakdown for each supersymmetric process.

Again by utilising the statistical method detailed in appendix(B), we derive a limit on the wino mass for a photino of mass 10 GeV/c^2 :

$$M_{\tilde{W}} > 33 \ \mathrm{GeV}/c^2 \qquad\qquad (90\%\ \mathrm{CL})$$

It is found that the event rates for the mass of photino 20 GeV/c^2 samples are too low to be able to set a limit in that case.

6.6 LIMITS ON THE MASSES OF THE SUPERSYMMETRIC PARTNERS OF THE QUARKS AND GLUONS

In most supersymmetric models, the supersymmetric partners of the quarks and gluons (squarks and gluinos respectively) are pair produced in proton-antiproton interactions with cross-sections which are calculable within perturbative QCD and which range (for $\sqrt{s}$ = 630 GeV) from 0.1-100 nb for masses in the range 20-70 GeV/c^2 [48],[54]. The squarks and gluinos then decay into final states containing the lightest supersymmetric particle, which in this analysis is assumed to be a photino. The photino is assumed to be stable and to be very weakly interacting. It will, as a result, escape detection.

If the gluino mass is greater than the squark mass, the production mechanism that predominates is $P\bar{P} \longrightarrow \tilde{q}\,\tilde{q} + X$, with the squarks each decaying to a quark and a photino. The final state will, therefore, contain two quarks and two photinos. This will result in an event with two jets and large missing transverse energy.

If, on the other hand, the gluino is less massive than the squark, the dominant production mechanism is $P\bar{P} \longrightarrow \tilde{g}\,\tilde{g} + X$, with each gluino decaying to $q\,q\,\tilde{\gamma}$ and the final state will contain four quark jets and a large missing transverse energy. If the squark or gluino mass is large, the photinos and quarks emerging from the decays of the squarks and gluinos will be at large angles with respect to the original squark or gluino direction.

These supersymmetric processes will therefore be more isotropic than events from the Standard Model sources of missing transverse energy (eg. $P\bar{P} \longrightarrow b\bar{b} + X$, $b \longrightarrow c\,e\,\nu$), which produce events with a back-to-back topology).

6.6.1 THE DATA SAMPLE

The data sample that was used to define the Isolated 4σ -missing transverse energy sample in chapter 5, is also used here. The selection criteria used are the same as those described in section(5.4), except that now it is required that there be at least two jets in the event and the previous cuts against back-to-back topologies are replaced by the requirement that the azimuthal angle between the two highest transverse energy jets be less than 140^0 [13].

A total of 4 events passed all the selection cuts of which three contain exactly two jets (with jet $E_T > 12$ GeV) and one contains three jets. Figure(6.27) shows the distribution in $\Delta\phi$ of the selected events (the histogram) before the application of the final $\Delta\phi < 140^0$ requirement. This distribution is strongly peaked towards $\Delta\phi = 180^0$, i.e. the highest transverse energy jets in the event are usually produced back-to-back in azimuth. These topologies are expected from jet fluctuation background (events which contain an apparent missing transverse energy arising from fluctuations in the calorimeter response to jets) and heavy flavour production.

6.6.2 THE STANDARD MODEL BACKGROUND

The expected contributions to the $\Delta\phi < 140^0$ multijet sample from conventional processes and from jet fluctuation background were evaluated using the ISAJET Monte-Carlo program together with a full simulation of the UA1 detector including hardware triggers. The known sources of large transverse momentum prompt neutrinos, i.e. W decays ($W \longrightarrow e\nu, \mu\nu, \tau\nu$), Z^0 decays ($Z^0 \longrightarrow \nu\bar{\nu}, c\bar{c}, b\bar{b}$) and semi-leptonic decays of heavy quarks, are considered. The number of events generated for each physics process corresponds to approximately 10 times the integrated luminosity. The $\Delta\phi$ distribution computed from the Monte-Carlo events (before applying the $\Delta\phi < 140^0$ cut) is shown in figure(6.27) as the dashed curve.

The total predicted number of events passing all the selection cuts is $5.2 \pm 1.9 \pm 1.0$ in good agreement with the 4 observed events. Table(10) shows the contributions from each of the Standard Model processes.

6.6.3 THE SUPERSYMMETRIC MODEL

The ISAJET Monte-Carlo with full simulation of the UA1 detector was again used to evaluate the expected rates of events from squark and gluino production passing the above selection criteria.

It has been assumed that the photino is the lightest supersymmetric particle and initially it is taken to be massless (the effect on the results of a massive photino is investigated). The u, d, s, c and b squarks are assumed to be degenerate in mass, and the left- and right-handed squarks have equal mass (the t-squark is ignored). Processes involving the supersymmetric partners of the W, Z and Higgs bosons or of the known leptons are not considered. The model used thus contains two free parameters : the masses of the squark and the gluino.

Only squark masses greater than 20 GeV/c^2 were considered because of the existence of limits from $e^+ e^-$ experiments [55] which yielded $M_{\tilde{q}} > 21.5$ GeV/c^2, and gluino masses greater than 4 GeV/c^2 because of a limit from a BEBC beam-dump experiment [56] which yielded $M_{\tilde{g}} > 3\text{-}4$ GeV/c^2 .

Events were generated for a wide range of squark and gluino masses and passed through the same selections programs as the data. All hard scattering processes of order $\alpha_s^{\,2}$ ($P\bar{P} \longrightarrow \tilde{g}\tilde{g}, \tilde{q}\tilde{q}, \tilde{g}\tilde{q}$) and $\alpha\alpha_s$ ($P\bar{P} \longrightarrow \tilde{g}\tilde{\gamma}, \tilde{q}\tilde{\gamma}$) were included in the calculation, which uses the matrix elements given in ref. [57]. Gluon bremsstrahlung from initial- and final-state partons (including squarks and gluinos) is included in the ISAJET program. Squarks and gluinos are decayed according to two- or three-body phase space. The decay modes used are taken from ref [54] and are :

if $M_{\tilde{g}} > M_{\tilde{q}}$ then: $\tilde{q} \longrightarrow q\tilde{\gamma}, \tilde{g} \longrightarrow \bar{q}\tilde{q}$

and if $M_{\tilde{q}} > M_{\tilde{g}}$ then: $\tilde{g} \longrightarrow \bar{q}q\tilde{\gamma}$
$\tilde{q} \longrightarrow q\tilde{g}$ branching ratio r/(1+r)
$\tilde{q} \longrightarrow q\tilde{\gamma}$ branching ratio 1/(1+r)

where $r = (4\,\alpha_s / 3\,\alpha\, e_q^{\,2})\,(1 - M_{\tilde{g}}^{\,2} / M_{\tilde{q}}^{\,2})^2$.

The main characteristics of the predictions of the supersymmetry model can be most easily seen by considering the two limiting cases : a) where the gluino mass becomes large so that $\tilde{q}\,\tilde{q}$ production dominates , and b) where the squark mass is large and $\tilde{g}\,\tilde{g}$ production dominates. Figure(6.28) shows the predicted event rate for infinitely large gluino mass. The event rate is dominated by $\tilde{q}\,\tilde{q}$ production. It can be seen that the event rate drops away with increasing squark mass as the cross-section falls. As the mass of the squark decreases the resulting missing transverse energy distribution becomes softer, the acceptance of the selection criteria thus falls. It can be seen that the fall in acceptance begins to win over the increasing cross-section as the mass of the squark falls below ~ 30 GeV/c^2.

In figure(6.29) is shown the predicted event rate for infinitely large squark mass. For large gluino masses the rate is dominated by direct gluino pair production ($P\bar{P} \longrightarrow \tilde{g}\tilde{g}$). For this process, as in the case of $\tilde{q}\tilde{q}$ production, the falling acceptance starts to win over the rising cross-section as the mass falls below ~ 30 GeV/c^2, and the resulting event rate would not allow us to exclude the existence of light gluinos. However, the contribution from indirect gluino pair production ($P\bar{P} \longrightarrow g\,X$, $g \longrightarrow \tilde{g}\tilde{g}$), where a gluon fragments into a $\tilde{g}\tilde{g}$ pair was evaluated. The contribution from this process is shown as a dashed curve in figure (6.29).

6.6.4 RESULTS

Figure (6.30) shows the 90% C.L. limit on the squark mass as a function of gluino mass. We find $M_{\tilde{q}} > 45$ GeV/c^2 (independently of gluino mass) and $M_{\tilde{g}} > 53$ GeV/c^2 (independently of squark mass) at the 90% CL. If $M_{\tilde{q}} = M_{\tilde{g}} = M$ we find $M > 75$ GeV/c^2 at 90% CL. In the computation of these limits all the statistical and systematic errors on the data and the Monte-Carlo calculations were taken into account. The limit on the gluino mass must be slightly qualified to take into account the effect of the gluino lifetime. For lifetimes greater then ~ 10^{-10} s, a significant fraction of the produced gluinos will reach the calorimeter before decaying, resulting in a loss of the missing transverse energy signature. Concerning the possibility of a massive photino, it is found that the predicted event rate is not appreciably reduced until the mass of the photino exceeds ~20 GeV/c^2, after which it drops rapidly. For a photino mass of 20 GeV/c^2, for example, the expected event rates are reduced by ~10%, corresponding to a reduction in the squark and gluino mass limits ~2-3 GeV/c^2.

Sparticle	Lower limit GeV/c^2	C.L %	Experiment
$\tilde{\gamma}$	10	90	ASP
$\tilde{Z}$	31	95	CELLO
$\tilde{W}$	22.5	95	JADE
	45	90	UA2
$\tilde{\nu}$	10.8	90	MAC
$\tilde{e}$	32	90	UA1
	30	90	UA2
	58	90	ASP
$\tilde{\mu}$	21	95	JADE
$\tilde{q}$	45	90	UA1
$\tilde{g}$	53	90	UA1
	58	90	UA2

Table (6.1) : *Current limits on the masses of supersymmetric particles.*

Process	g_V	g_A
$\tilde{W}\tilde{\gamma}$	$\sin^2\gamma_{(0)}$	0
$\tilde{W}\tilde{Z}$	$\frac{N_1}{\sqrt{2}}\{2\sin\gamma_{(0)}\cot\theta_W\frac{M_Z}{\mu_-}-\frac{\cos\gamma_{(0)}}{\sin\theta_W}\}$	0
$\tilde{W}^+\tilde{W}^-$	$-\cot\theta_W\{1-\frac{1}{2}\sec^2\theta_W\cos^2\gamma_{(0)}\}$	0

Table (6.2) : *The simplified couplings, in the massless photino scenario, for the three processes that contribute to gaugino pair production.*

process	events	statistical error		systematic error			
		M.C.	PTW	E.Scale	Jet-fluctuation	H.Flavour	-B.Ratio
W/Z (3 Species)	7.08	1.31	2.28	0.05			
W—>tau—>Hadrons	7.14	0.90	0.95	0.46			0.50
PP —> Heavy Flavour	0.21	0.72		0.02		0.21	
Jet-Fluctuation	3.38	0.60			0.68		
TOTAL	17.81	1.85	3.23	0.53	0.68	0.21	0.50
DATA	17						

Table (6.3) : *The predicted contributions from standard physics processes to the $L_\tau < 0$ and $E_T^{jet} < 40$ Gev data sample.*

Mass of wino (Gev/c^2)	Total number of events	Total M.C error	Total PTW error	Total E.S error
20	29.92	2.5	2.14	2.58
30	20.13	1.62	1.68	1.72
35	16.79	1.34	1.81	1.23
40	17.54	1.53	1.73	1.18
45	9.37	0.83	1.67	0.57
50	3.88	0.41	0.36	0.29
55	3.22	0.35	0.33	0.20
60	1.68	0.19	0.16	0.13
70	0.49	0.05	0.04	0.04

Table (6.4) : *The total expected contributions to the* $L_\tau < 0$ *and* $E_T^{jet} < 40$ *Gev data sample from the wino-photino, wino-zino and wino-wino supersymmetric processes in the massless photino scenario.*

$M_{\tilde{W}}$	wino - photino process				wino - wino process				wino - zino process			
GeV/c^2	Events	PTW error	Energy scale error	M C Stat error	Events	PTW error	Energy scale error	M C Stat error	Events	PTW error	Energy scale error	M C Stat error
20	23.43	1.64	1.93	1.88	1.87	0.199	0.189	0.765	4.62	0.30	0.46	1.46
30	14.69	0.99	1.28	1.22	3.12	0.22	0.31	0.78	2.32	0.47	0.13	0.73
35	12.26	1.17	0.92	1.11	2.99	0.49	0.19	0.67	1.53	0.14	0.12	0.32
40	12.32	1.12	0.91	1.05	5.0	0.59	0.25	1.12	0.22	0.02	0.02	0.04
45	7.34	0.86	0.43	0.75	2.0	0.31	0.14	0.37	0.03	0.002	0.002	0.005
50	3.85	0.36	0.29	0.41	0.03	0.003	0.002	0.007				
55	3.22	0.33	0.20	0.35								
60	1.68	0.16	0.13	0.19								
70	0.49	0.04	0.04	0.05								

Table (6.5) : *The expected contributions from each of the three supersymmetric processes contributing to the* $L_\tau < 0$ *and* $E_T^{jet} < 40$ *Gev data sample for the massless photino scenario.*

Mass of wino (Gev/c^2)	Total number of events	Total M.C error	Total PTW error	Total E.S error
20	13.58	2.42	2.55	0.52
35	8.46	0.89	1.28	0.47
40	10.46	0.95	1.22	0.74
50	5.47	0.61	0.69	0.35
60	3.1	0.34	0.35	0.20

Table (6.6) : *The total expected contributions to the $L_\tau < 0$ and $E_T^{jet} < 40$ Gev data sample from the wino-photino, wino-zino and wino-wino supersymmetric processes when the mass of the photino is 10 Gev/c^2.*

$M_{\tilde{W}}$	wino - photino process				wino - wino process				wino - zino process			
GeV/c^2	Events	PTW error	Energy scale error	M C Stat error	Events	PTW error	Energy scale error	M C Stat error	Events	PTW error	Energy scale error	M C Stat error
20	6.59	1.22	0.21	0.80	0.61	0.04	0.06	0.35	6.38	1.28	0.24	2.25
35	7.11	0.80	0.44	0.78	1.28	0.46	0.03	0.43	0.08	0.02	0.005	0.02
40	8.91	0.98	0.63	0.88	1.55	0.24	0.11	0.36	0.002	0.0002	0.0002	0.0005
50	5.41	0.69	0.35	0.61	0.06	0.007	0.004	0.01				
60	3.05	0.35	0.20	0.34								

Table (6.7) : *The expected contributions from each of the three supersymmetric processes with a photino of mass 10 Gev/c^2, contributing to the $L_\tau < 0$ and $E_T^{jet} < 40$ Gev data sample .*

Mass of wino GeV/c^2	Total number of events	Total M.C error	Total PTW error	Total E.S error
30	5.52	0.86	3.40	0.03
35	3.98	0.80	0.98	0.06
40	4.40	0.64	0.81	0.22
50	2.00	0.28	0.21	0.15
60	1.30	0.17	0.19	0.07

Table (6.8) : *The total expected contributions to the* $L_\tau < 0$ *and* $E_T^{jet} < 40$ *Gev data sample from the wino-photino, wino-zino and wino-wino supersymmetric processes when the mass of the photino is 20 Gev/*c^2.

$M_{\tilde{W}}$	wino - photino process				wino - wino process				wino - zino process			
GeV/c^2	Events	PTW error	Energy scale error	M C Stat error	Events	PTW error	Energy scale error	M C Stat error	Events	PTW error	Energy scale error	M C Stat error
30	3.38	0.78	0.03	0.62	2.07	2.60	0.0003	0.60	0.069	0.02	0.0000	0.028
35	2.57	0.54	0.06	0.48	1.42	0.45	0.0003	0.63				
40	2.47	0.50	0.01	0.42	1.92	0.31	0.13	0.48				
50	1.95	0.20	0.14	0.28	0.07	0.009	0.005	0.01				
60	1.30	0.19	0.07	0.17								

Table (6.9) : *The expected contributions from each of the three supersymmetric processes with a photino of mass 20 Gev/*c^2*, contributing to the* $L_\tau < 0$ *and* $E_T^{jet} < 40$ *Gev data sample .*

W/Z processes (excluding tau)	1.17 ± 1.02 ± 0.23
Heavy flavour (b and c) processes	1.98 ± 0.84 ± 1.01
tau —> hadrons	1.87 ± 0.80 ± 0.34
Jet fluctuations	0.14 ± 0.13 ± 0.04
Total	5.2 ± 1.9 ± 1.0

Table (6.10) : *Predicted numbers of events from Standard Model processes, passing all selection criteria, together with statistical and systematic errors.*

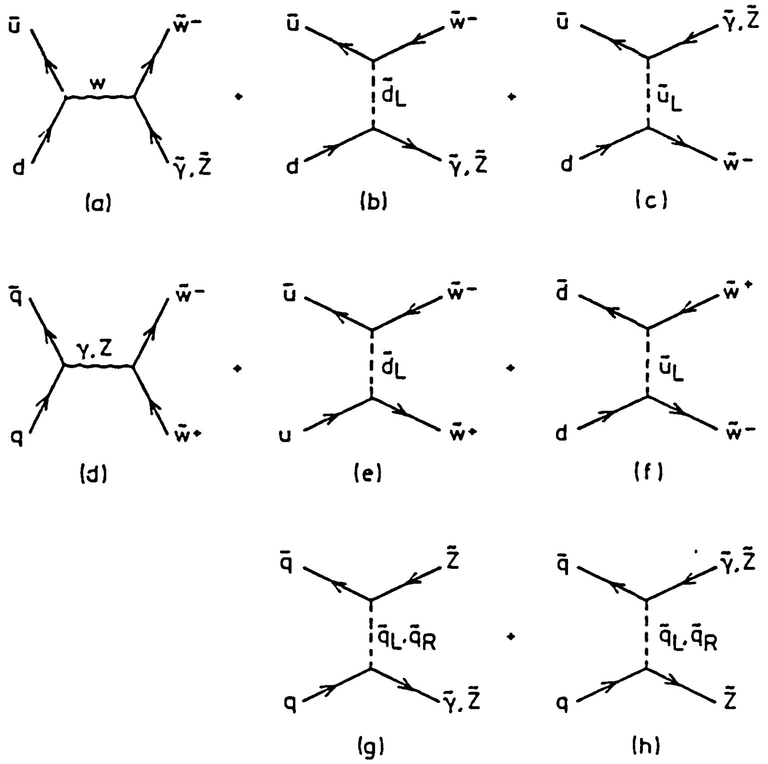

Figure (6.1) : *The lowest-order Feynman diagrams which contribute to gaugino pair production at hadron colliders.*

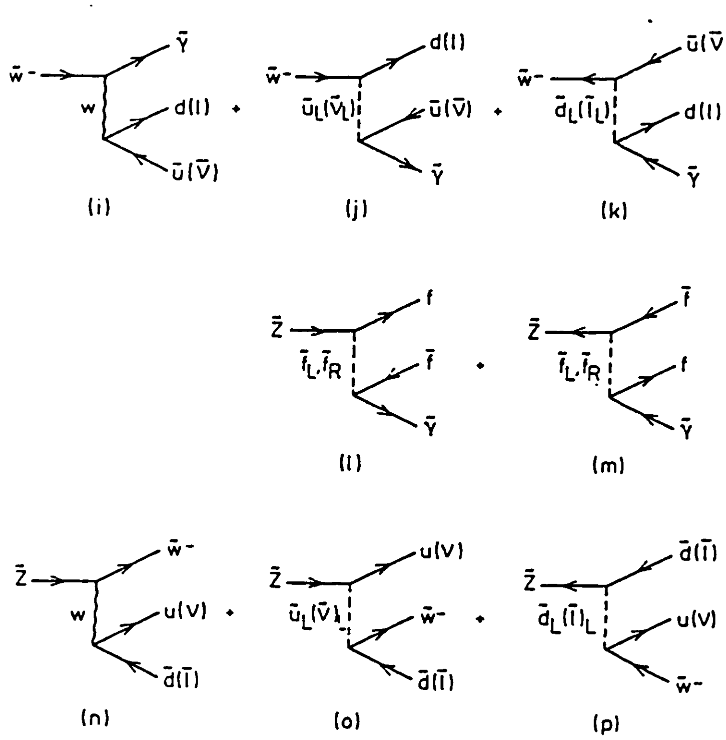

Figure (6.2) : *The lowest order Feynman diagrams which contribute to the decay of the gauginos.*

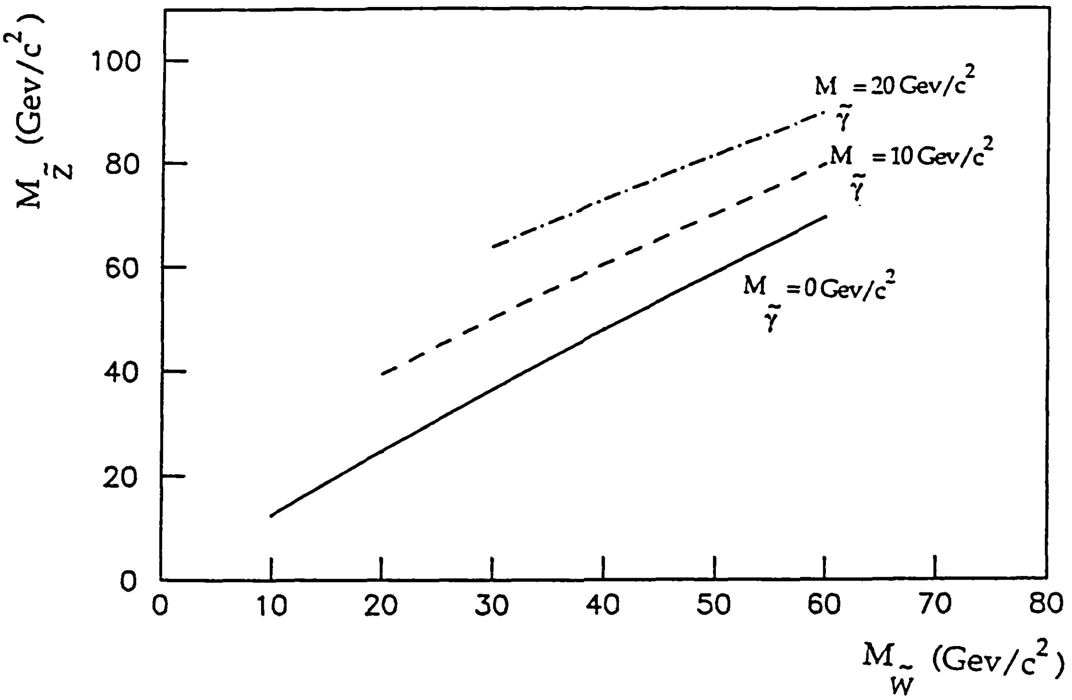

Figure (6.3) : *The variation of the zino mass as a funcction of the wino mass for three values of photino mass.*

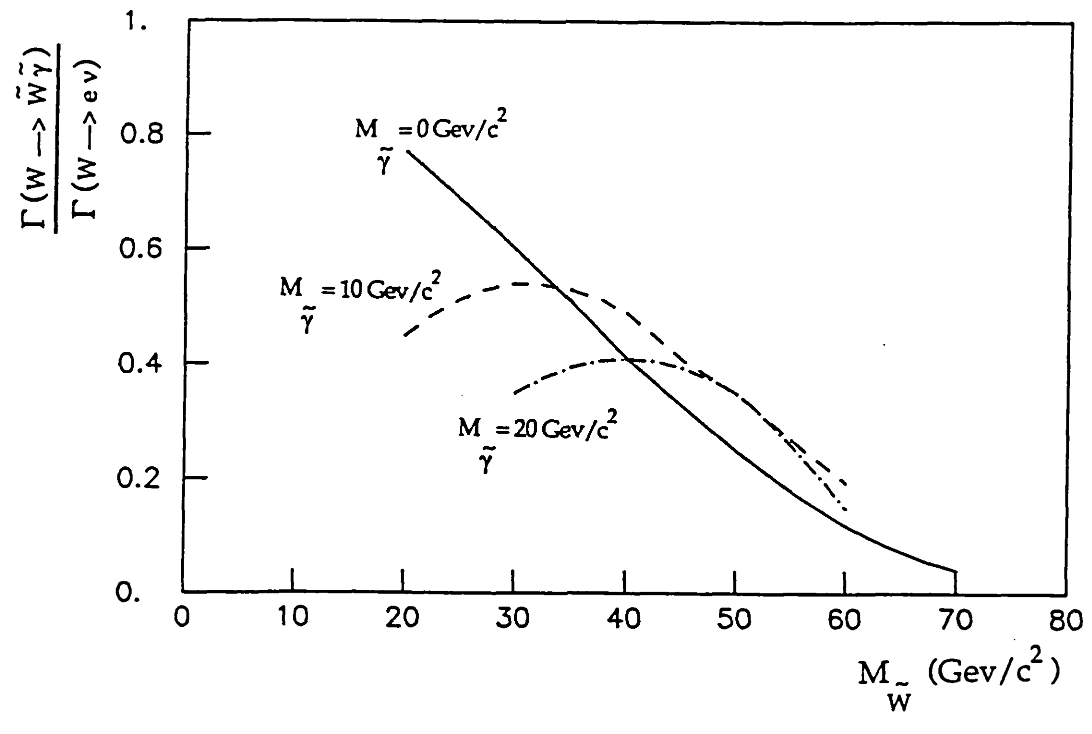

Figure (6.4) : *The ratio of the partial width of the W into a wino-photino pair to the partial width of the electron decay mode of the W. Variation with photino mass is also shown.*

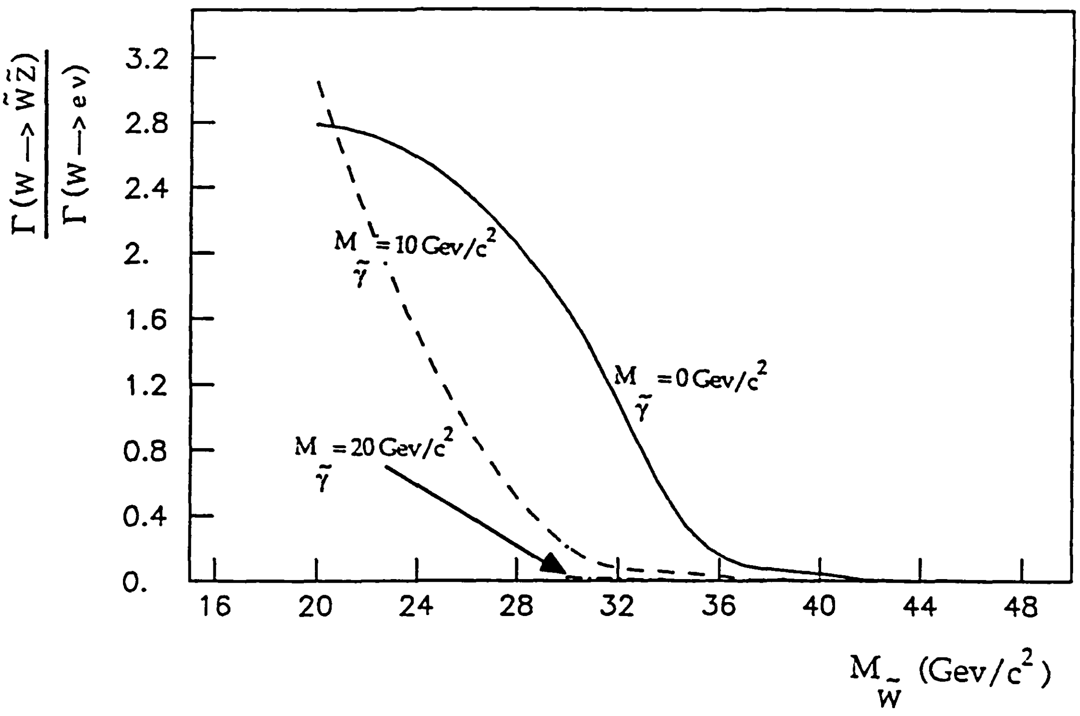

Figure (6.5) : *The ratio of the partial width of the W into its wino-zino decay channel to its electron-neutrino decay mode. Variation with photino mass is also shown.*

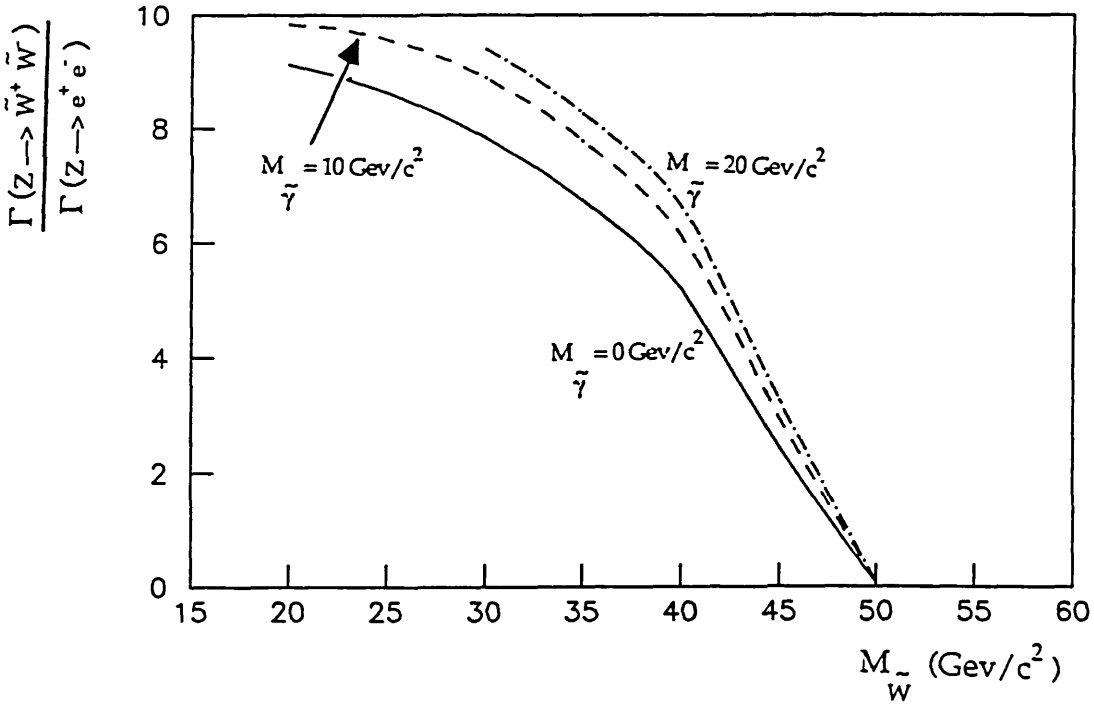

Figure (6.6) : *The ratio of the partial width of the Z into its wino-wino decay channel to its electron decay mode. Variation with photino mass is also shown.*

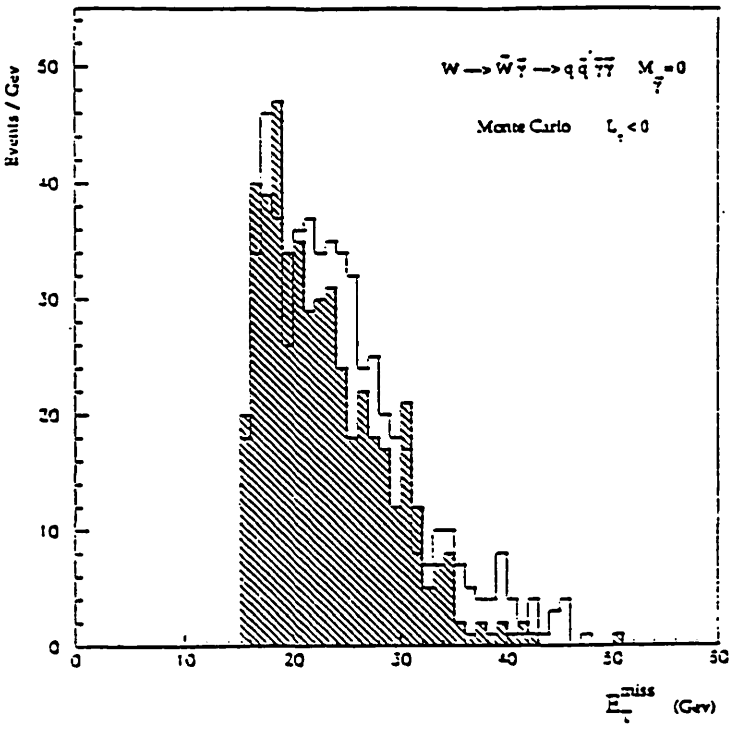

Figure (6.7) : *E_T^{miss} distribution for wino-photino events, with E_T^{miss} > 15 Gev and N_σ>2.5 for wino masses of 50 Gev/c^2(shaded histogram) and 20 Gev/c^2. The photino is massless.*

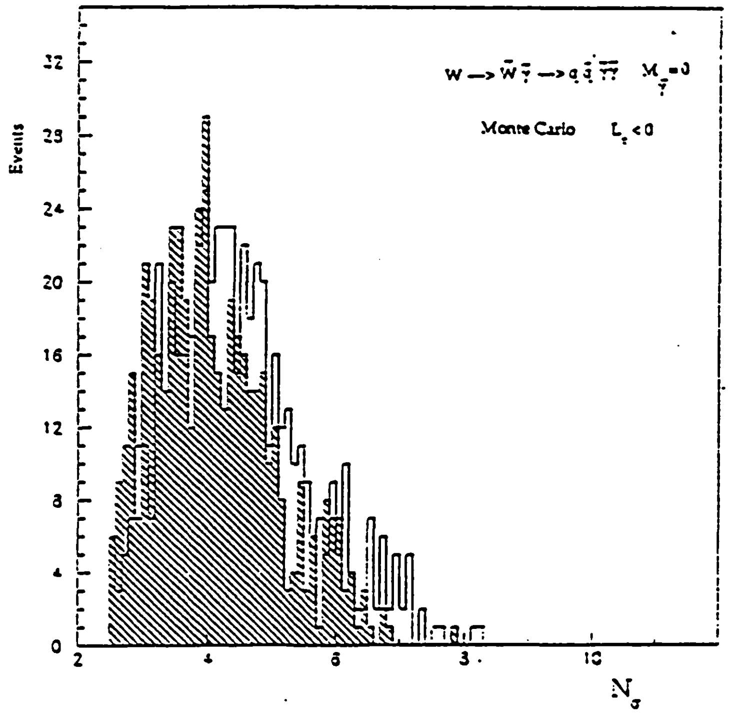

Figure (6.8) : *N_σ distribution for wino-photino events, with E_T^{miss} > 15 Gev and N_σ>2.5 for wino masses of 50 Gev/c^2(shaded histogram) and 20 Gev/c^2. The photino is massless.*

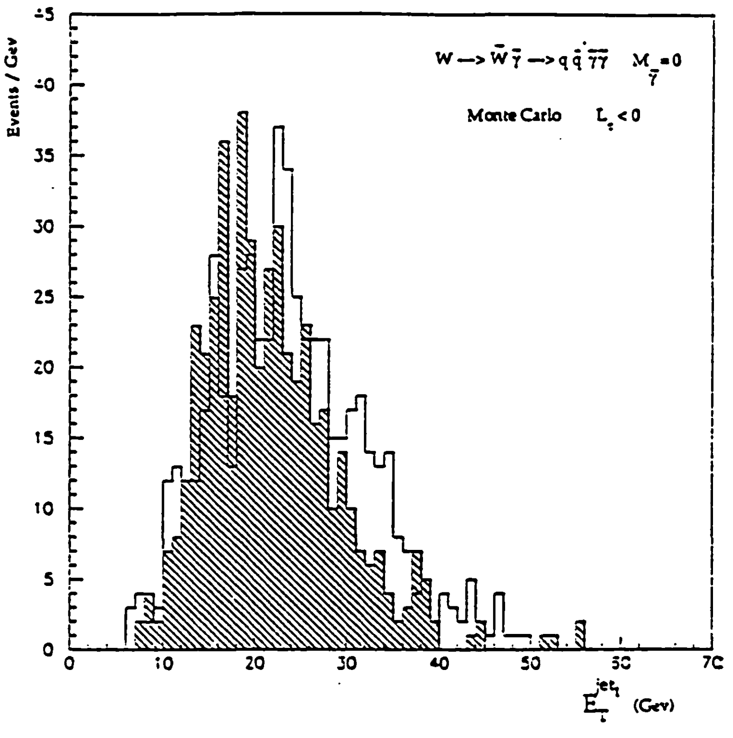

Figure (6.9) : E_T^{jet}(*for the highest* E_T *jet in the event) distribution for wino-photino events, with* E_T^{miss} > *15 Gev and* N_σ>*2.5 for wino masses of 20 Gev/c*^{2}*(shaded histogram) and 50 Gev/c*^{2}*. The photino is massless.*

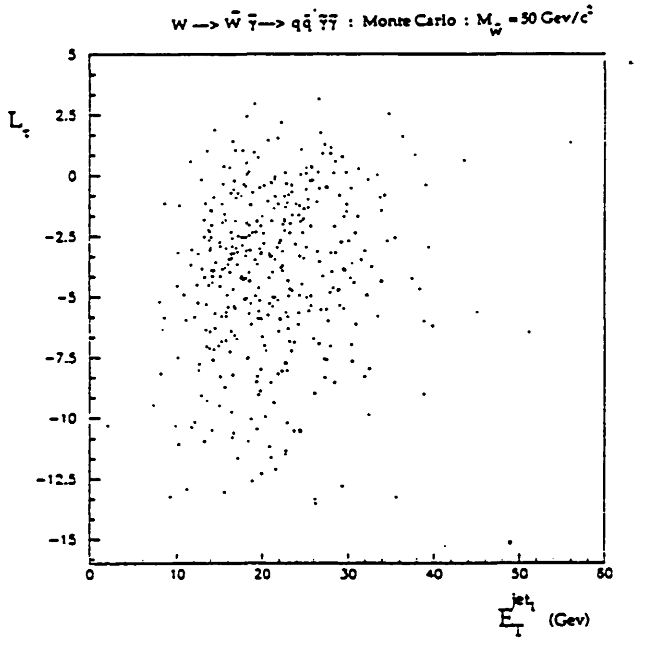

Figure (6.10) : *Scatter plot of* L_τ *versus* E_T^{jet} *of the highest* E_T *jet, for the wino-photino Monte Carlo events with mass of wino 50 Gev/c*^{2} *and a massless photino.*

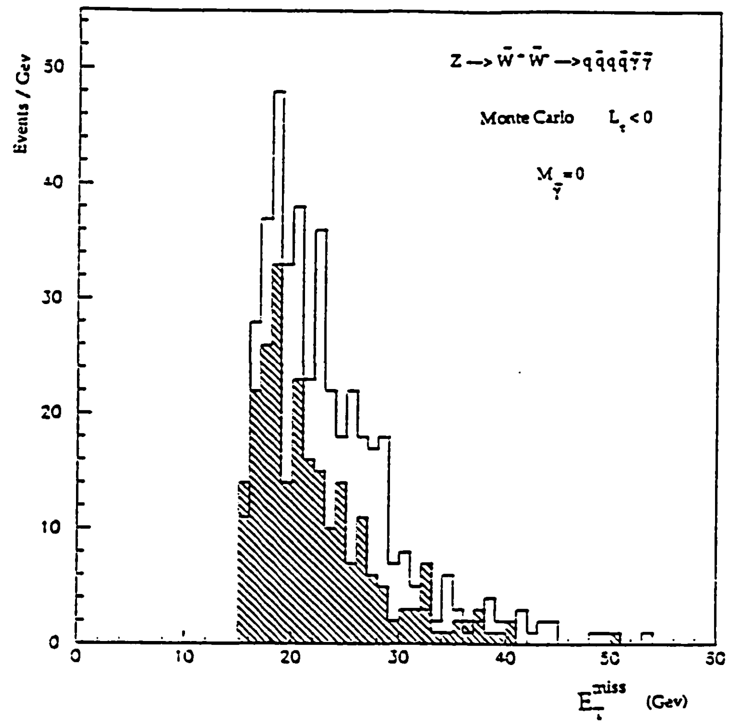

Figure (6.11) : $E_T{}^{miss}$ *distribution for wino-wino events, with* $E_T{}^{miss} > 15$ *Gev and* $N_\sigma > 2.5$ *for wino masses of 20 Gev/c²(shaded histogram) and 50 Gev/c². The photino is massless.*

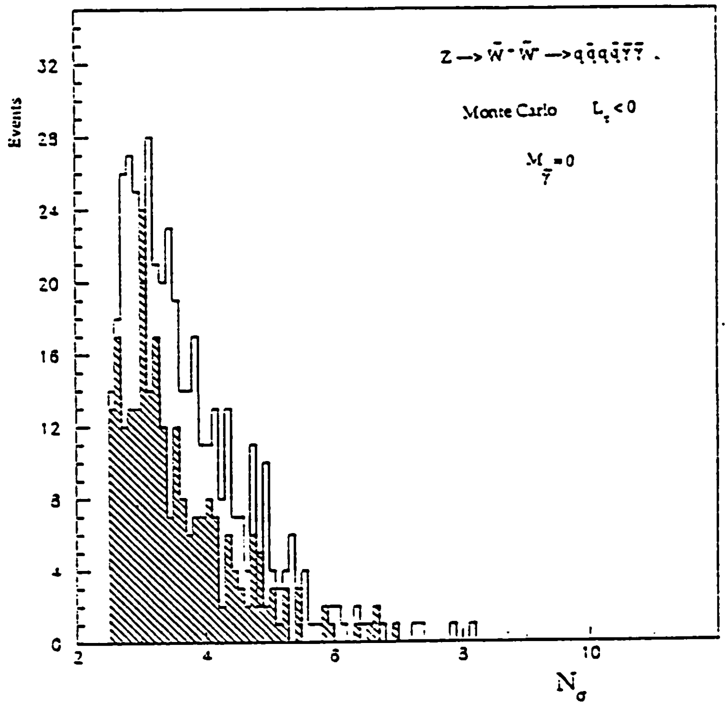

Figure (6.12) : N_σ *distribution for wino-wino events, with* $E_T{}^{miss} > 15$ *Gev and* $N_\sigma > 2.5$ *for wino masses of 20 Gev/c²(shaded histogram) and 50 Gev/c². The photino is massless.*

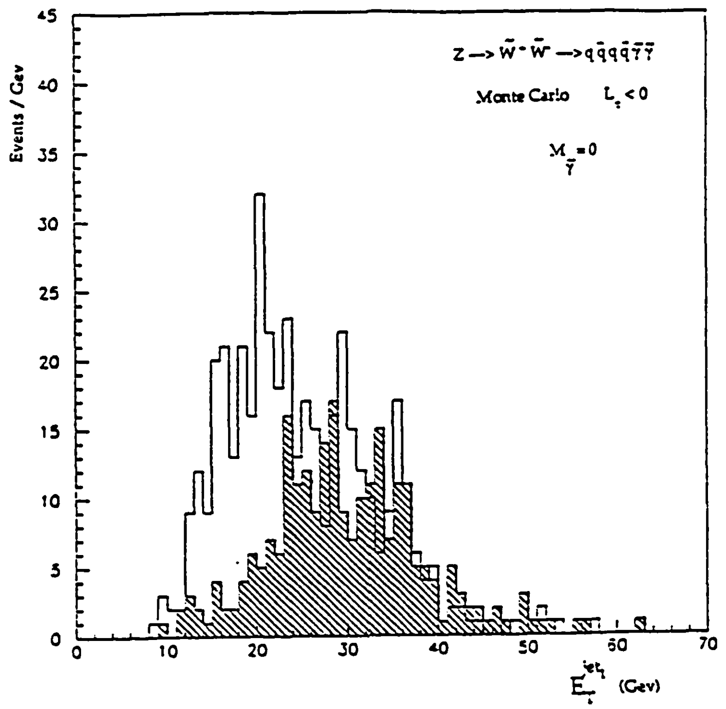

Figure (6.13) : E_T^{jet}*(for the highest* E_T *jet in the event) distribution for wino-wino events, with* E_T^{miss} *> 15 Gev and* N_σ*>2.5 for wino masses of 20 Gev/c*^{2}*(shaded histogram) and 50 Gev/c*^{2}*. The photino is massless.*

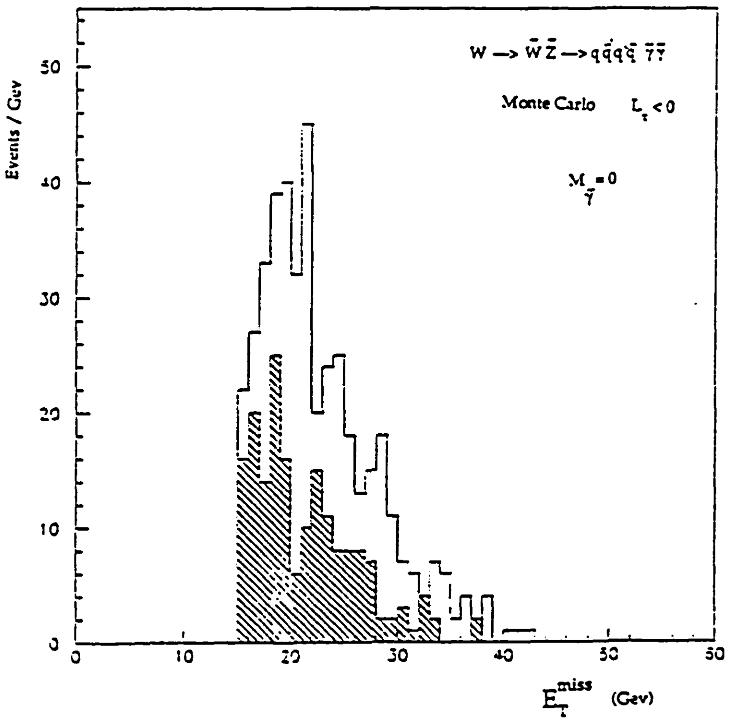

Figure (6.14) : E_T^{miss} *distribution for wino-zino events, with* E_T^{miss} *> 15 Gev and* N_σ*>2.5 for wino masses of 20 Gev/c*^{2}*(shaded histogram) and 45 Gev/c*^{2}*. The photino is massless.*

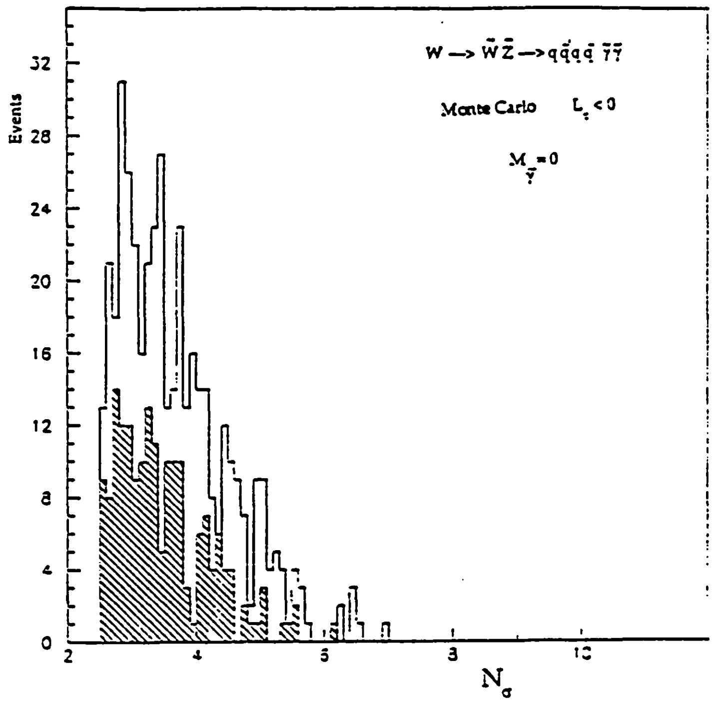

Figure (6.15) : N_σ *distribution for wino-zino events, with* E_T^{miss} > *15 Gev and* N_σ>*2.5 for wino masses of 20 Gev/*c^2*(shaded histogram) and 45 Gev/*c^2*. The photino is massless.*

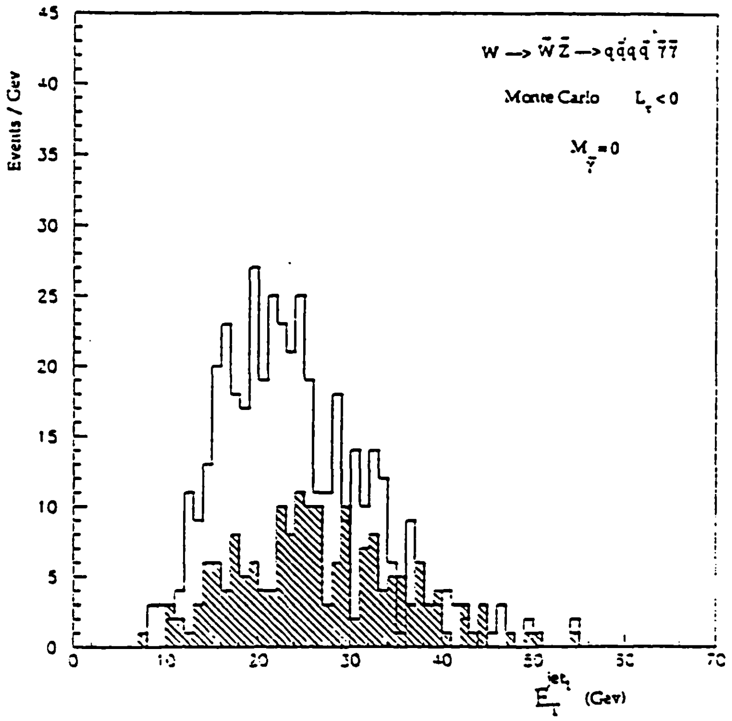

Figure (6.16) : E_T^{jet}*(for the highest* E_T *jet in the event) distribution for wino-zino events, with* E_T^{miss} > *15 Gev and* N_σ>*2.5 for wino masses of 20 Gev/*c^2*(shaded histogram) and 45 Gev/*c^2*. The photino is massless.*

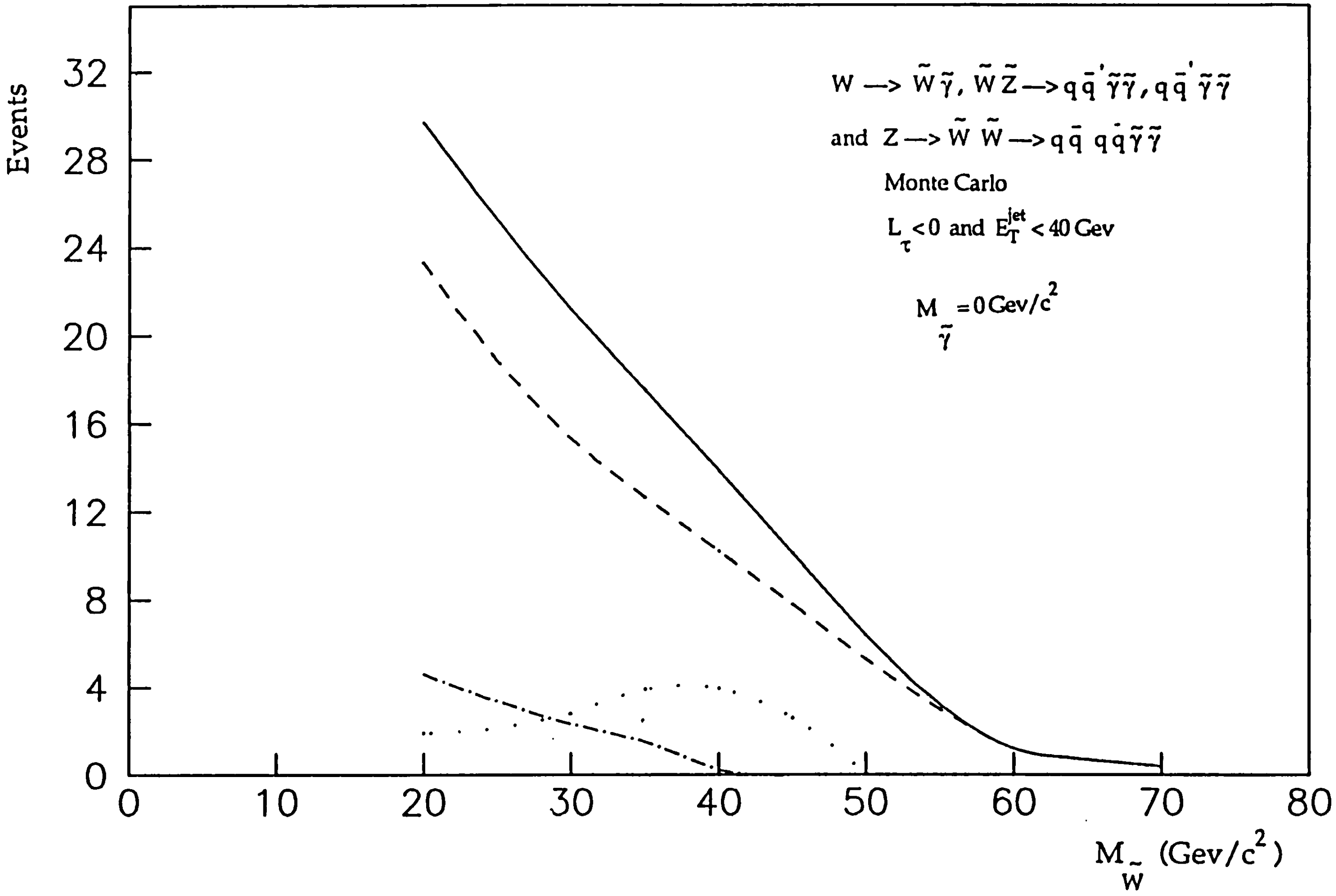

Figure (6.17) : *Predicted rates of isolated 4σ events with $L_\tau < 0$ and $E_T^{jet} <$ 40 Gev from the supersymmetric decays of the intermediate vector bosons, as a function of the wino mass. The total rate is shown as the solid curve. The wino-photino(dashed), wino-zino(dot-dash) and wino-wino(dotted) rates are also shown. The photino is massless.*

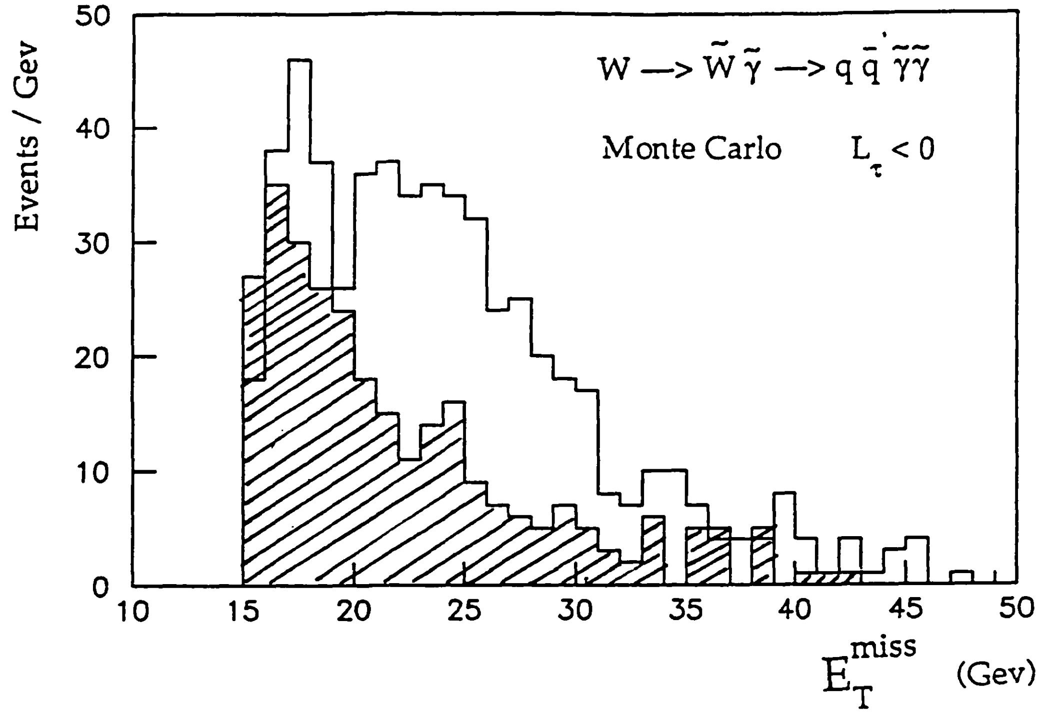

Figure (6.18) : *E_T^{miss} distribution for wino-photino events with $E_T^{miss} >$ 15 Gev/c^2 and $N_\sigma > 2.5$ for massless photino and for photino of mass 17 Gev/c^2(shaded histogram). The wino mass in both cases is 20 Gev/c^2.*

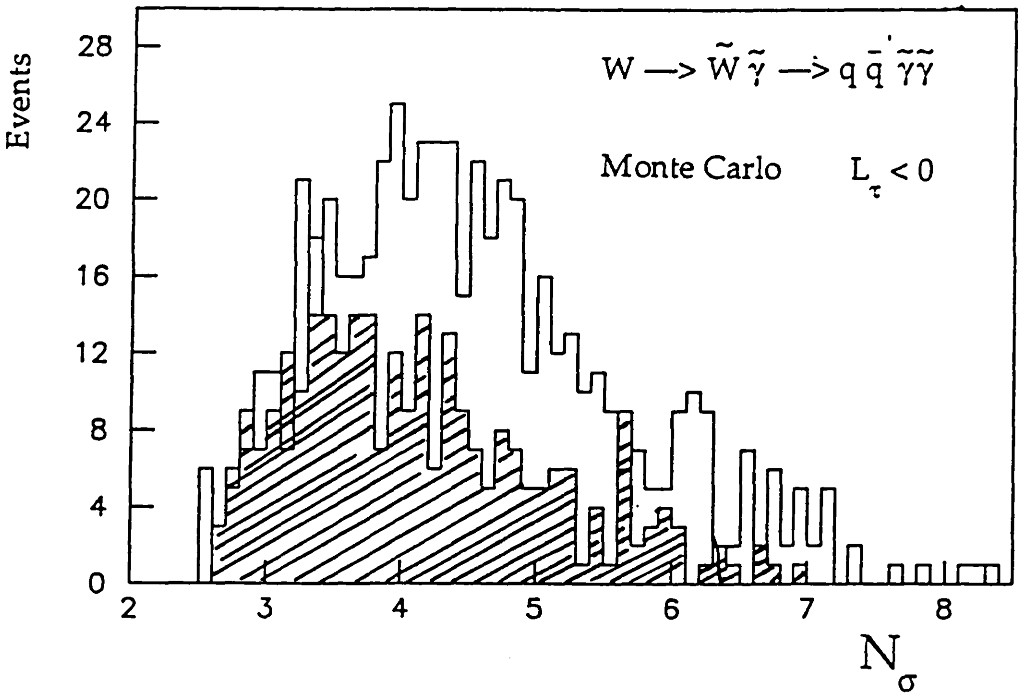

Figure (6.19) : *N_σ distribution for wino-photino events with $E_T^{miss} > 15$ Gev/c^2 and $N_\sigma > 2.5$ for massless photino and for photino of mass 17 Gev/c^2(shaded histogram). The wino mass in both cases is 20 Gev/c^2.*

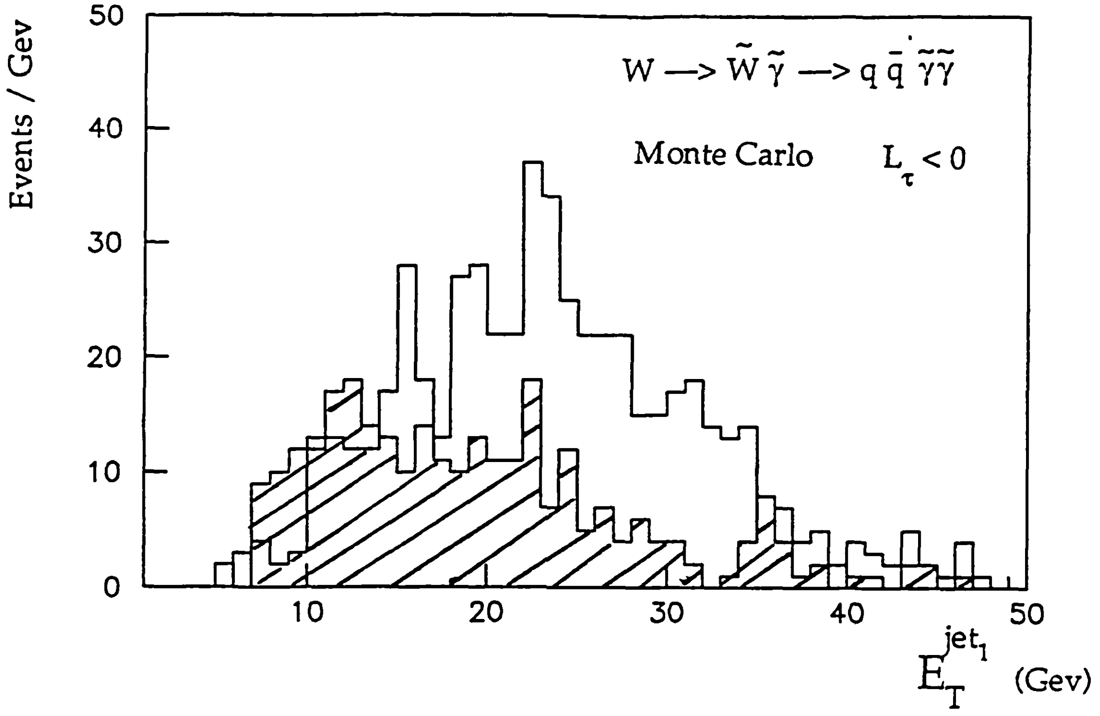

Figure (6.20) : E_T^{jet}*(for the highest* E_T *jet in the event) distribution for wino-photino events with* $E_T^{miss} > 15$ *Gev/c*^{2} *and* $N_\sigma > 2.5$ *for massless photino and for photino of mass 17 Gev/c*^{2}*(shaded histogram). The wino mass in both cases is 20 Gev/c*^{2}.

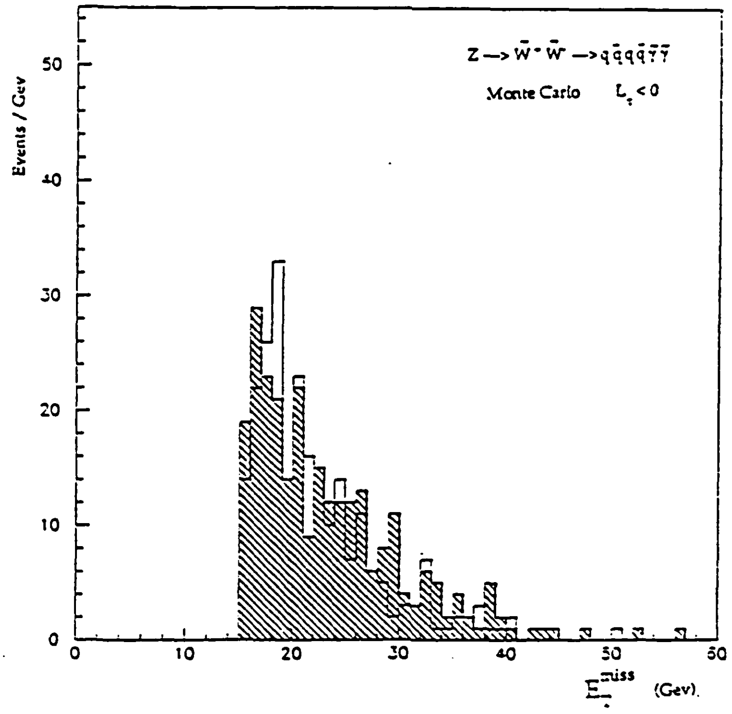

Figure (6.21) : E_T^{miss} *distribution for wino-wino events with* $E_T^{miss} > 15$ *Gev/c*^{2} *and* $N_\sigma > 2.5$ *for massless photino and for photino of mass 17 Gev/c*^{2}*(shaded histogram). The wino mass in both cases is 20 Gev/c*^{2}.

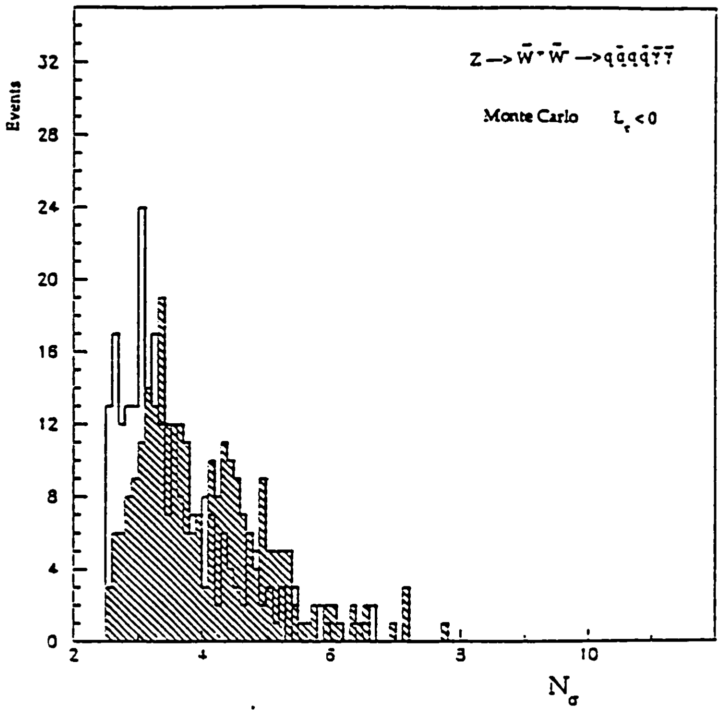

Figure (6.22) : *N_{σ} distribution for wino-wino events with $E_T^{miss} > 15$ Gev/c^2 and $N_{\sigma} > 2.5$ for massless photino and for photino of mass 17 Gev/c^2(shaded histogram). The wino mass in both cases is 20 Gev/c^2.*

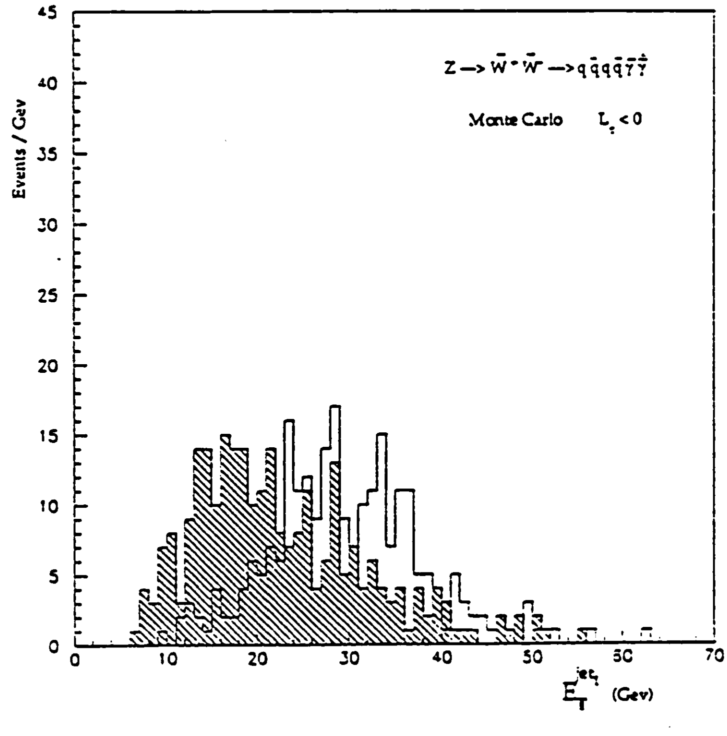

Figure (6.23) : *E_T^{jet}(for the highest E_T jet in the event) distribution for wino-wino events with $E_T^{miss} > 15$ Gev/c^2 and $N_{\sigma} > 2.5$ for massless photino and for photino of mass 17 Gev/c^2(shaded histogram). The wino mass in both cases is 20 Gev/c^2.*

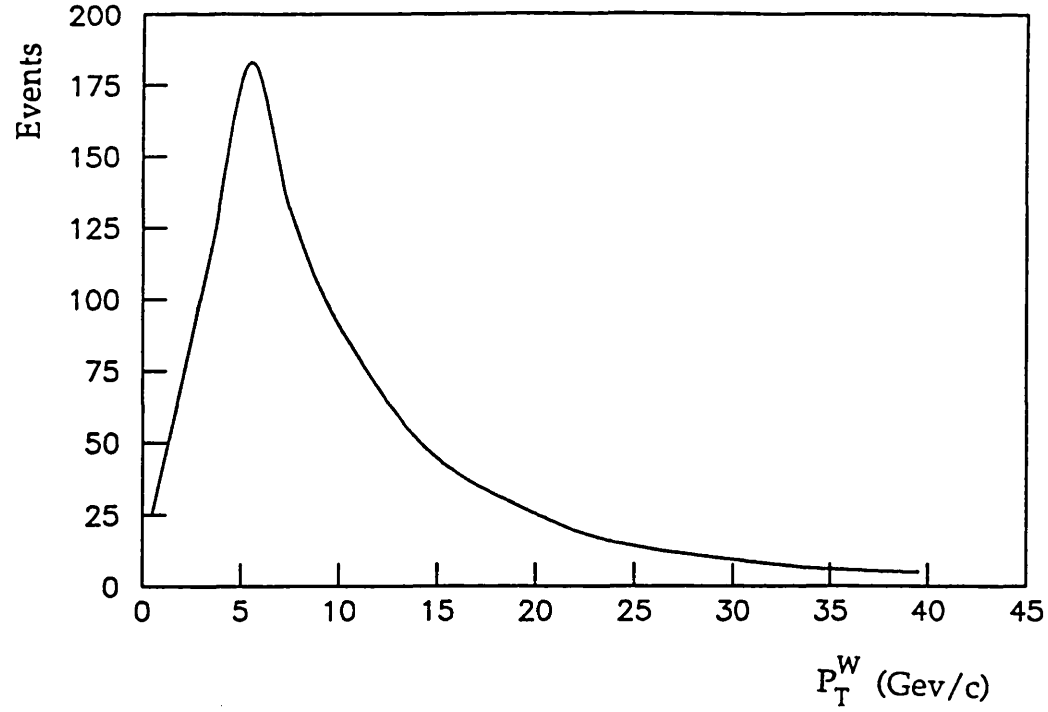

Figure (6.24) : *The P_T spectrum of the W for the mass of wino 20 Gev/c^2 and mass of photino 17 Gev/c^2 wino-wino sample before any cuts are applied.*

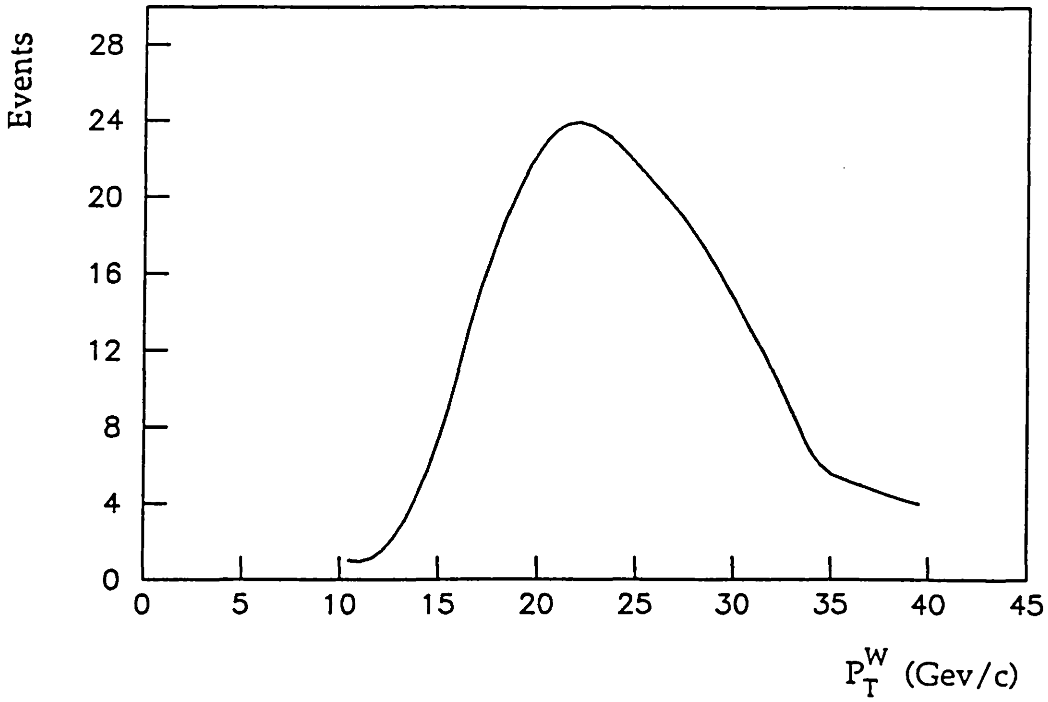

Figure (6.25) : *The P_T spectrum of the W for the mass of wino 20 Gev/c^2 and mass of photino 17 Gev/c^2 wino-wino sample after the requirement E_T^{miss} > 15 Gev is made.*

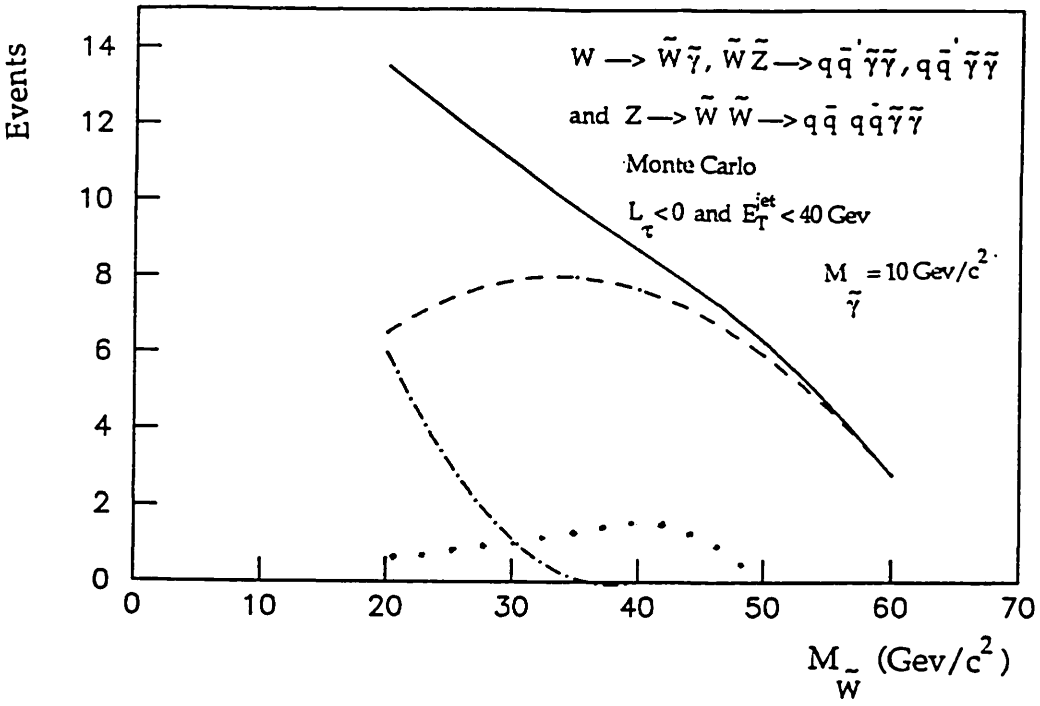

Figure (6.26) : *Predicted rates of isolated* 4σ *events with* $L_\tau < 0$ *and* $E_T^{jet} <$ *40 Gev from the supersymmetric decays of the intermediate vector bosons, as a function of the wino mass. The total rate is shown as the solid curve. The wino-photino(dashed), wino-zino(dot-dash) and wino-wino(dotted) rates are also shown. The mass of the photino is* $10 Gev/c^2$.

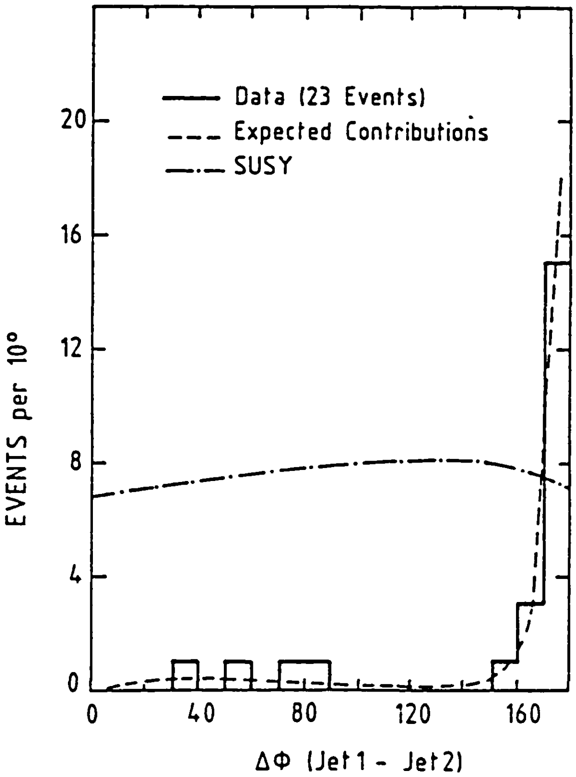

Figure (6.27) : *Azimuthal angle between the two highest transverse energy jets in each event,* $\Delta\phi$, *for data(histogram), Monte Carlo of Standard Model processes(solid curve), and for squark pair production at* $m_q = 60$ Gev/c^2.

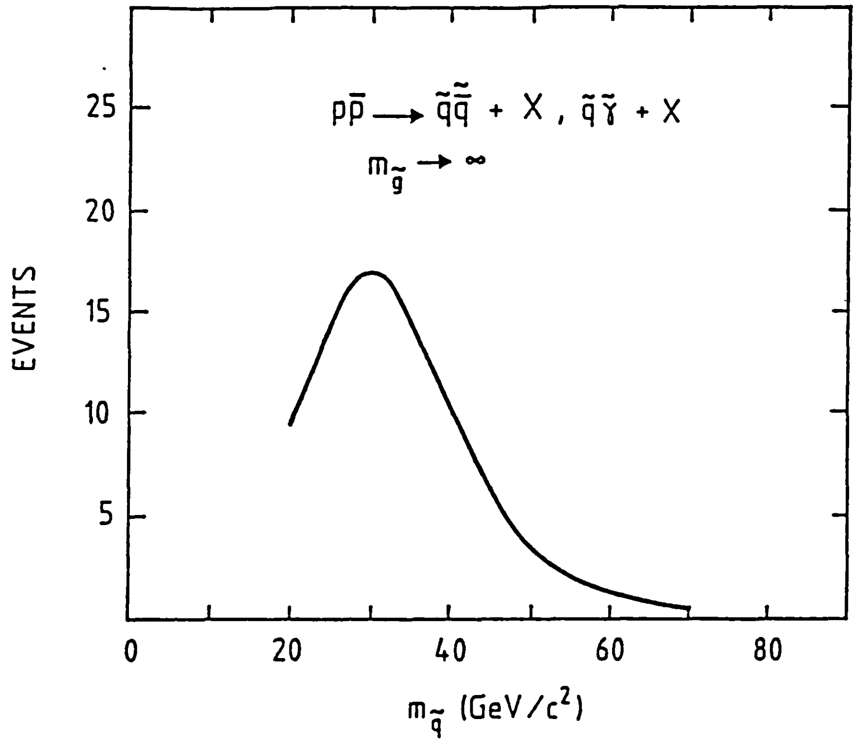

Figure (6.28) : *predicted number of events passing all selection cuts from the supersymmetry Monte Carlo as a function of the squark mass as the gluino mass becomes infinitely large.*

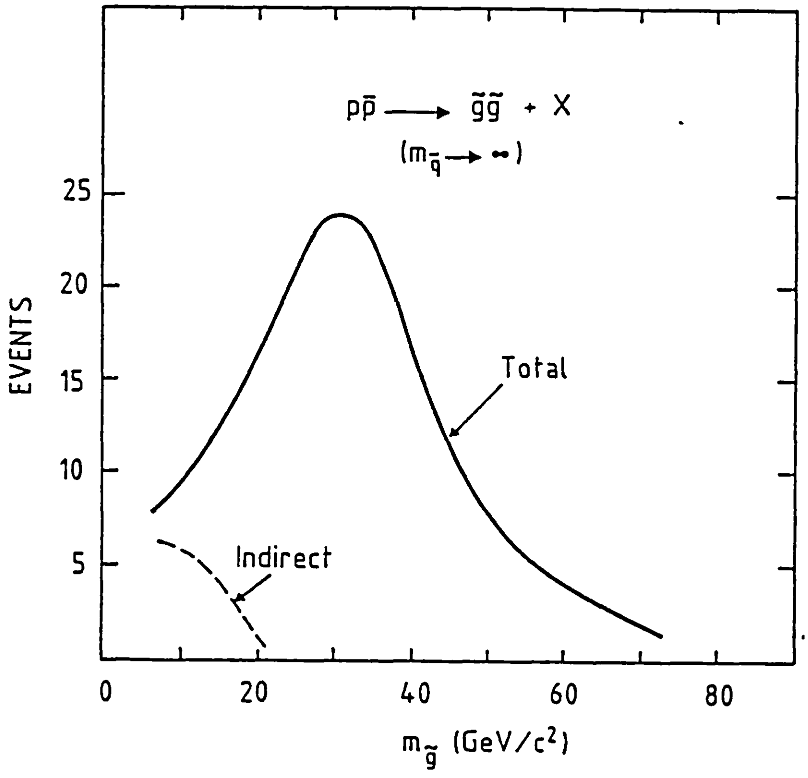

Figure (6.29) : *predicted number of events passing all selection cuts from the supersymmetry Monte Carlo as a function of the gluino mass as the squark mass becomes infinitely large.*

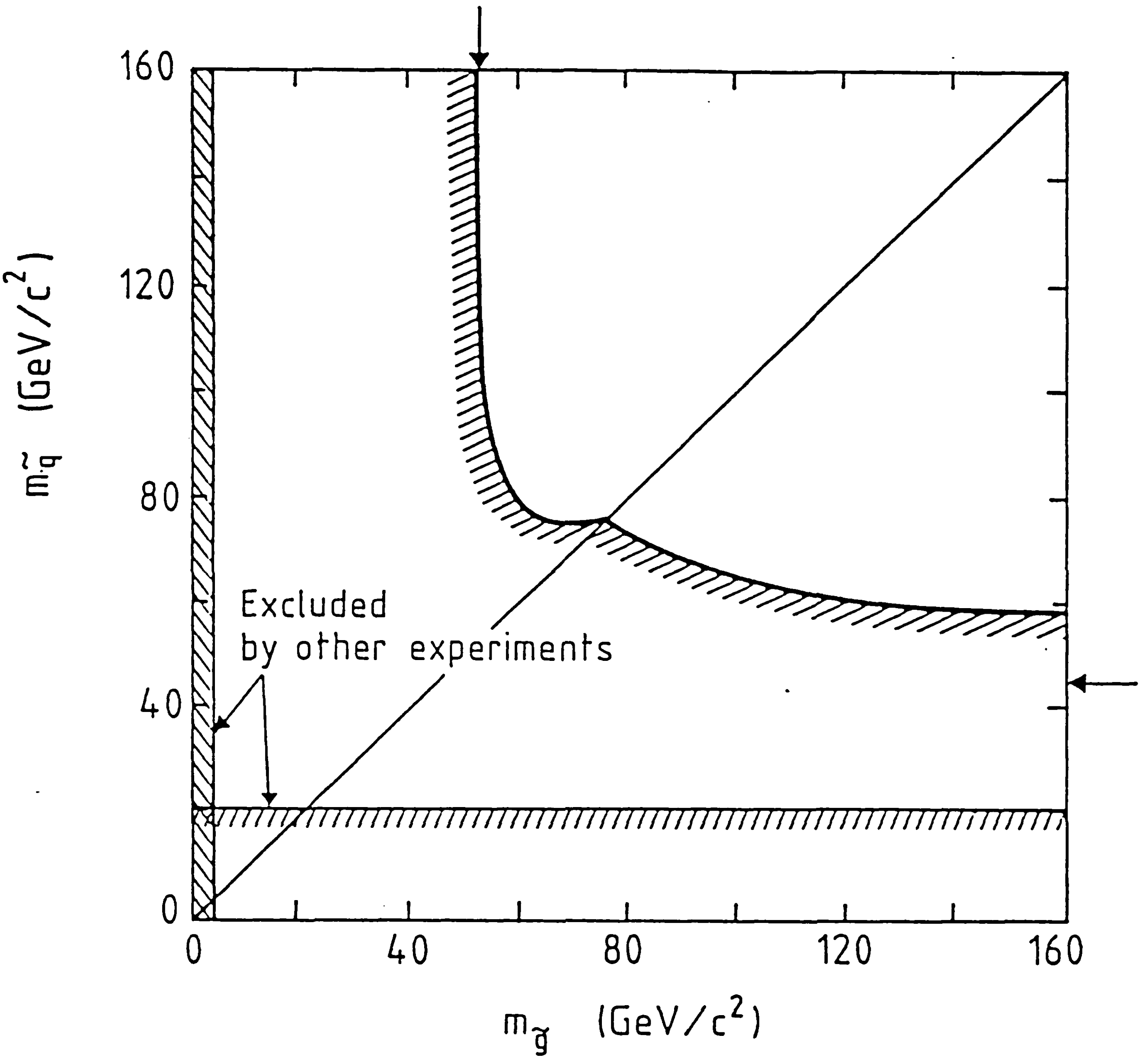

Figure (6.30) : *Limits (at 90% C.L.) on squark and gluino masses derived from the large missing transverse energy multijet sample. The arrows indicate the asymptotic values of the 90% C.L. contour as the squark and gluino masses become infinitely large.*

CHAPTER 7

CONCLUSIONS

The analysis of events with large missing transverse energy in proton-antiproton collisions is a powerful method to test the Standard Model and to search for new physics processes. An inclusive selection of events with large missing transverse energy was performed by the UA1 experiment at CERN, on the data recorded during the data-taking periods in 1983, 1984, 1985. This selection yielded a sample of 56 events containing one or more hadronic jets produced in association with large missing transverse energy. Of these 56 events,53 are mono-jets and three are dijet events. There are no events with three or more jets ($E_T^{jet} > 12$ GeV). This data sample, called the isolated 4σ- data sample, was then used to search for evidence of supersymmetric decays of the intermediate vector bosons.

In order to study the physics origin of the events in the above data sample, Monte Carlo methods were used to simulate missing transverse energy events from all known Standard Model processes. The measured rates of $W^{\pm}$ and Z^0 production in UA1 and heavy flavour cross-sections were used to calculate the expected event rates. A total contribution of $52.2 \pm 6.9 \pm 3.6$ events is predicted (the first error is statistical and the second one is systematic) is found to agree well with the observed 56 events.

As the largest contribution to the isolated 4σ- sample comes from the decay of the W into a tau lepton and a neutrino, where the tau decays semi-hadronically into hadrons and a neutrino, and as this process is considered to be a background in the search for supersymmetric processes,a tau-likelihood variable (L_τ) is constructed by utilising the known properties of jets arising from the semi-hadronic decays of tau leptons. The requirement $L_\tau < 0$ separates out the tau signal and leaves 24 events which constitute the non-τ sample. The expectation from Standard Model processes is 20.8 $\pm$ 5.0 $\pm$ 1.1 events. The rates and properties of the non-τ sample are consistent with expectations from the Standard Model.

If the supersymmetric partners of the intermediate vector bosons, the wino and the zino, exist then the decays $W \longrightarrow \tilde{W}\tilde{\gamma}$, $\tilde{W}\tilde{Z} \longrightarrow q\bar{q}'\tilde{\gamma}\tilde{\gamma}$, $q\bar{q}'q\bar{q}\tilde{\gamma}\tilde{\gamma}$ and $Z \longrightarrow \tilde{W}^{+}\tilde{W}^{-} \longrightarrow \bar{q}'q\,q\,\bar{q}'\tilde{\gamma}\tilde{\gamma}$ will produce events with one or more jets in association with large missing transverse energy and will consequently contribute to the isolated 4σ - sample. The expected rates depend on the mass of the wino and the mass of the photino. These processes usually have $L_{\tau} < 0$ and $E_T^{jet} < 40$ GeV/c^2 for the highest E_T jet in the event. To place a limit on the mass of the wino, the data sample with $L_{\tau} < 0$ and $E_T^{jet} < 40$ GeV/c^2 was used. This data sample contains 17 events compared to 17.8 $\pm$ 3.7 $\pm$ 1.0 events predicted for conventional physics processes.

In the massless photino scenario, we derived a limit; $m_{\tilde{W}} > 45$ GeV/c^2 (90% CL). As the mass of the photino rises to 10 GeV/c^2 this limit drops to $m_{\tilde{W}} > 33$ GeV/c^2 (90% CL). For mass of photino 20 GeV/c^2 the event rate is too low to be able to set a limit.

A further selection, requiring there to be two or more jets in each event and replacing the isolation cuts of the non-τ sample by the requirement that the difference $\Delta\phi$ in azimuthal angle between the two highest transverse energy jets satisfies $\Delta\phi < 140^0$, was carried out to enable a search to be made for the production and decay of the supersymmetric partners of the quarks and the gluons. This sample was referred to as the $\Delta\phi < 140^0$ multijet data sample and comprised four events of which three contained exactly two jets ($E_T^{jet} > 12$ GeV) and one contained three jets. The Standard Model expectation for this selection is 5.2 $\pm$ 1.9 $\pm$ 1.0 events, which agrees well with the 4 events observed.

Expected event rates for selected values of squark and gluino masses were calculated using Monte Carlo methods. Assuming the photino to be massless we find $m_{\tilde{q}} > 45$ GeV/c^2 (90% CL), independently of gluino mass and $m_{\tilde{g}} > 53$ GeV/c^2 (90% CL), independently of squark mass. For equal squark and gluino masses we find a limit $m_{\tilde{q}} = m_{\tilde{g}} = 75$ GeV/c^2 (90% CL). These results are insensitive to photino masses of up to approximately 20 GeV/c^2.

APPENDIX A

THE SPECIFIC FORM OF THE GAUGINO LAGRANGIAN AND THE COUPLINGS

The specific form for the gaugino lagrangian is taken from the supersymmetric model of Baer, Hagiwara and Tata [52] . It has the following particular form :

$$\begin{aligned} L_{\text{gaugino}} = {} & e\, \tilde{W} \gamma^{\mu} \tilde{W} A_{\mu} - e \cot\theta_W\, \tilde{W} \gamma^{\mu} (x_c - y_c \gamma_5)\, \tilde{W} Z_{\mu} \\ & + [\, \tilde{W} \gamma^{\mu} (iA + B\gamma_5) \tilde{\gamma} W_{\mu} + \tilde{W} \gamma^{\mu} (iC + D\gamma_5) \tilde{Z} W_{\mu} \\ & + \text{H.C} \,] \qquad \text{(A.1)} \end{aligned}$$

Where

$$x_c = 1 - \frac{1}{4} \sec^2\theta_W (\cos^2\gamma_L + \cos^2\gamma_R) \qquad \text{(A.2)}$$

$$y_c = \frac{1}{4} \sec^2\theta_W (\cos^2\gamma_R - \cos^2\gamma_L) \qquad \text{(A.3)}$$

$$A = g \sin\theta_W \left\{ \frac{\sin^2\gamma_L + \sin^2\gamma_R}{2} \right\} + \left\{ \frac{g}{\sqrt{2}} N_1 f_- + \sqrt{2}\, g N_1 f_+ \frac{M_Z}{\mu_-} \cos\theta_W \right\} \varepsilon_1 \qquad \text{(A.4)}$$

$$B = ig\sin\theta_W \left\{\frac{\sin^2\gamma_R - \sin^2\gamma_L}{2}\right\} + \left\{\frac{g}{\sqrt{2}} N_2 f_- + \sqrt{2}\, g\, f_+ \frac{M_Z}{\mu_+}\cos\theta_W\right\} \varepsilon_2 \qquad (A.5)$$

$$C = \left\{\frac{g}{\sqrt{2}} N_1 f_- + \sqrt{2}\, g N_1 f_+ \frac{M_Z}{\mu_-}\cos\theta_W\right\} - g f_+ \sin\theta_W\, \varepsilon_1 \qquad (A.6)$$

$$D = \left\{\frac{g}{\sqrt{2}} N_2 f_- - \sqrt{2}\, g N_2 f_+ \frac{M_Z}{\mu_+}\cos\theta_W\right\} \delta \qquad (A.7)$$

Also $g = e / \sin^2\theta_W$, where θ_W is the electroweak mixing angle and e is the positron charge.

$$\varepsilon_1 = \sqrt{2}\, N_1 \frac{M_Z}{\mu_-^2} \sin\theta_W \cos\theta_W (\mu_2 - \mu_1) \qquad (A.8)$$

$$\varepsilon_2 = -\sqrt{2}\, N_2 \frac{M_Z}{\mu_+^2} \sin\theta_W \cos\theta_W (\mu_2 - \mu_1) \qquad (A.9)$$

$$\delta = \frac{2 N_1 N_2}{\mu_+ + \mu_-} (\mu_2 \cos^2\theta_W + \mu_1 \sin^2\theta_W) \qquad (A.10)$$

$$N_{1,2} = \left\{\frac{\mu_- , \mu_+}{2(\mu_+ + \mu_-)}\right\}^{\frac{1}{2}} \qquad (A.11)$$

μ_- and μ_+ are the masses of the light and the heavy zinos respectively, in the massless photino scenario.
Where μ_- is given by the expression :

$$\mu_- = (m_1^{(0)\,2} + M_Z^2)^{\frac{1}{2}} - m_1^{(0)} \qquad (\text{A.12})$$

in which M_Z is the mass of the Z boson ($m_1^{(0)}$ is defined below).
Also μ_+ is related to μ_- by the expression :

$$\mu_+ = \frac{M_Z^2}{\mu_-} \qquad (\text{A.13})$$

The mass of the photino is given by the expression :

$$m_{\tilde{\gamma}} = | \mu_2 \sin^2\theta_W + \mu_1 \cos^2\theta_W | \qquad (\text{A.14})$$

and

$$\mu_1 = \frac{5}{3} \tan^2\theta_W \, \mu_2 \qquad (\text{A.15})$$

using (A.14) and (A.15) one obtains

$$|\mu_2| = \frac{3}{8} \frac{m_{\tilde{\gamma}}}{\sin^2\theta_W} \qquad (\text{A.16})$$

($\mu_2 < 0$). The mass of the low mass wino eigenstate is given by :

$$m_- = \left| \left[(m_1 - \frac{\mu_2}{2})^2 + M_W^2 \right]^{\frac{1}{2}} - (m_1 + \frac{\mu_2}{2}) \right| \qquad (\text{A.17})$$

Treating the masses of the wino and the photino as two free parameters and fixing their values, then using (A.16) and (A.17) one obtains :

$$m_1 = \left\{ \frac{M_W^2 - m_-^2 - m_- \mu_2}{2\,(m_- + \mu_2)} \right\} \qquad (A.18)$$

When the photino has a non-zero mass. (A.18) yields $m_1^{(0)}$ - the superscript denoting the massless photino case.

For the scenario under investigation in this thesis, $v = v'$ which implies $\gamma_L = \gamma_R = \gamma$, $f_+ = \sin\gamma$ and $f_- = -\cos\gamma$ and also :

$$\tan\alpha = \frac{v'}{v} = 1 \qquad (A.19)$$

This yields :

$$\tan\gamma = \left\{ \frac{2M_W\,(2m_1 - |\mu_2|)}{(4m_1^2 - |\mu_2|^2) - \sqrt{(4m_1^2 - |\mu_2|^2)^2 + 4M_W^2\,(4m_1^2 + |\mu_2|^2 - 4m_1\,|\mu_2|)}} \right\}$$

$$(A.20)$$

So all needed couplings can be worked out in terms of two free parameters - the mass of the wino and the mass of the photino.

Comparison of (6.8) with (A.1) and using (A.2) through to (A.20) one obtains the following couplings :

$$g_V^{(W \to \tilde{W}\tilde{\gamma})} = \sin^2\gamma + \frac{N_1}{\sqrt{2}} \left\{ 2\sin\gamma \cot\theta_W \frac{M_Z}{\mu_-} - \frac{\cos\gamma}{\sin\theta_W} \right\} \varepsilon_1 \qquad (A.21)$$

Where ε_1 is given by:

$$\varepsilon_1 = \sqrt{2}\, N_1 \frac{M_Z}{\mu_-^2} \sin\theta_W \cos\theta_W \,(1 - \frac{5}{3}\tan^2\theta_W)\,\mu_2 \qquad (A.21a)$$

$$g_A^{(W \to \tilde{W}\tilde{\gamma})} = -\frac{N_2}{\sqrt{2}} \left\{ 2\sin\gamma \cot\theta_W \frac{M_Z}{\mu_+} + \frac{\cos\gamma}{\sin\theta_W} \right\} \varepsilon_2 \qquad (A.22)$$

Where ε_2 is given by :

$$\mathcal{E}_2 = -\sqrt{2}\, N_2 \frac{M_Z}{\mu_+^2} \sin\theta_W \cos\theta_W \left(1 - \frac{5}{3} \tan^2 \theta_W \right) \mu_2 \tag{A.22a}$$

$$g_V^{(Z \to \tilde{W}^+ \tilde{W}^-)} = -\cot\theta_W \left\{ 1 - \frac{1}{2} \sec^2 \theta_W \cos^2 \gamma \right\} \tag{A.23}$$

$$g_A^{(Z \to \tilde{W}^+ \tilde{W}^-)} = 0 \tag{A.24}$$

$$g_V^{(W \to \tilde{W} \tilde{Z})} = -\sin\gamma\, \mathcal{E}_1 + \frac{N_1}{\sqrt{2}} \left\{ 2 \sin\gamma \cot\theta_W \frac{M_Z}{\mu_-} - \frac{\cos\gamma}{\sin\theta_W} \right\} \tag{A.25}$$

$$g_A^{(W \to \tilde{W} \tilde{Z})} = -\frac{N_2}{\sqrt{2}} \left\{ 2 \sin\gamma \cot\theta_W \frac{M_Z}{\mu_+} + \frac{\cos\gamma}{\sin\theta_W} \right\} \delta \tag{A.26}$$

Where δ is given by :

$$\delta = \frac{2\, N_1 N_2}{\mu_+ + \mu_-} \left(\cos^2 \theta_W + \frac{5}{3} \tan^2 \theta_W \sin^2 \theta_W \right) \mu_2 \tag{A.26a}$$

APPENDIX B

THE STATISTICAL METHOD USED TO DERIVE MASS LIMITS

The statistical method used to derive the mass limits is described in this appendix. In the derivation of each mass limit, one has a number N_D of events observed in the data sample. Then by the use of Monte-Carlo methods, one calculates the number of events from standard model processes that are expected to contribute to this data sample D, and the mean expected number of events is denoted by μ_B. This expectation is regarded as background. Again by the employment of Monte-Carlo methods the supersymmetric process, upon which one would like to set a limit, is generated and the mean expected number of these signal events is denoted μ_S. μ_B and μ_S are positive and real numbers. N_S and N_B are defined as the number of signal and background events, respectively, expected in the data sample D. They are positive, real integers governed by Poisson distributions :

$$P(N_B, \mu_B) = \frac{1}{N_B!} e^{-\mu_B} \mu_B^{N_B} \qquad (N_B = 0, 1, 2, ...) \qquad \text{(B.1)}$$

$$P(N_S, \mu_S) = \frac{1}{N_S!} e^{-\mu_S} \mu_S^{N_S} \qquad (N_S = 0, 1, 2, ...) \qquad \text{(B.2)}$$

So $P(N_B, \mu_B)$ yields the probability of observing a number N_B of events given that the mean expected number of background events is μ_B.

The total number of events expected N_T, is given by $N_T = N_B + N_S$. This number N_T has to be compared with the number observed N_D, for the derivation of a limit.

Since the number N_T is the sum of two independent Poisson processes, it too is distributed according to a Poisson, with a mean $\mu_T = \mu_B + \mu_S$. However, μ_S and μ_B have statistical and systematic errors associated with them and when these are taken into account in constructing a probability distribution function for N_T, the resulting distribution is no longer a Poisson distribution.

The mean μ_B, is governed by the Gaussian distribution :

$$G(\mu_B) = C \exp\left[\frac{-(\mu_B - \mu_B^{mc})^2}{2(\sigma_B^{mc})^2}\right] \qquad \text{(B.3)}$$

Where $\mu_B{}^{mc}$ and $\sigma_B{}^{mc}$ are the expected mean and the associated statistical error obtained from the standard physics Monte-Carlos, and C is an arbitrary normalisation constant. The number N_S, of expected signal events obeys the Poisson distribution (B.2) and the mean μ_S is governed by a Gaussian distribution similiar to (B.3), with $\mu_S{}^{mc}$ and $\sigma_S{}^{mc}$ as the expected mean and the associated statistical error, respectively, calculated from the Monte-Carlo for the signal supersymmetric process.
The total number of events $N_T = N_B + N_S$, is then governed by the Poisson distribution :

$$P(N_T, \mu_T) = \frac{1}{N_T!} e^{-\mu_T} \mu_T^{N_T} \qquad (N_T = 0, 1, 2, ...) \qquad \text{(B.4)}$$

Where μ_T is governed by the Gaussian distribution :

$$G(\mu_T) = F \exp\left[\frac{-(\mu_T - \mu_T^{mc})^2}{2(\sigma_T^{mc})^2}\right] \qquad \text{(B.5)}$$

Where $\mu_T{}^{mc} = \mu_B{}^{mc} + \mu_S{}^{mc}$ and :

$$\sigma_T^{mc} = \sqrt{(\sigma_B^{mc})^2 + (\sigma_S^{mc})^2} \qquad \text{(B.6)}$$

And F is an arbitrary normalisation constant. By using the known values of $\mu_T{}^{mc}$ and $\sigma_T{}^{mc}$, one calculates a random μ_T according to the Gaussian distribution (B.5). This value of μ_T is then inserted into (B.4) and a random N_T is calculated according to that Poisson distribution. Now since $\mu_S{}^{mc}$ and $\sigma_S{}^{mc}$ can be determined for any value of the wino mass, N_S and therefore N_T can be calculated as a function of wino mass. For each wino mass, a distribution of N_T (e.g. 10000 values of N_T) is generated. This is like a set of N_T distributions from performing the same (Monte-Carlo) experiment many times for each wino mass. That particuliar value of the mass of the wino which results in an N_T distribution with $N_T > N_D$ more than 90% of the time (e.g. 9000 values of N_T, where $N_T > N_D$), is the desired 90% CL lower bound on the mass of the wino.

The errors ; σ_B and σ_S used in the calculation of the limits are statistical errors. A limit that is obtained by performing the above calculations is regarded as the central value of the limit. The effect of systematic errors is included by a repetition of the same calculation, first using the mean expected events plus systematic errors and then using the mean expected events less systematic errors. The result can then be expressed as the central value of the limit $\pm\ \delta(\text{sys})$, where $\delta(\text{sys})$ is the difference between the central value of the limit and the values calculated including systematic errors.

REFERENCES

[1] S. Van der Meer, CERN ISR-PO internal report 72-31 (1972)
S. Van der Meer, 'Stochastic cooling and the accumulation of antiprotons', Rev. Mod. Phys, 57(1985) 3

[2] G. Arnison et al. (UA1 collaboration), *Experimental observation of isolated large transverse energy electrons with associated missing energy at* $\sqrt{s} = 540$ *Gev* ,
Phys. Lett. 122B (1983) 103.

[3] G. Arnison et al. (UA1 collaboration), *Experimental observation of lepton pairs of invariant mass around 95 Gev/*c^2 *at the CERN SPS collider,*
Phys. Lett. 126B (1983) 398.

[4] G. Arnison et al. (UA1 collaboration), *observation of the muonic decay of the charged IVBs,* Phys. Lett. 134B (1984) 469.

[5] C. Albajar et al. (UA1 collaboration), *Search for* B^0 - B^0 *oscillations at the CERN proton - antiproton collider,* Phys. Lett. 186B (1987) 247.

[6] G. Arnison (UA1 collaboration), *Observation of jets in high transverse energy events at the CERN proton - antiproton collider,* Phys. Lett. 123B (1983) 115.

[7] C. Albajar et al. (UA1 collaboration), *Events with large missing transverse energy at the CERN collider :* $W \rightarrow \tau \nu$ *decay and test of* τ-μ-e *universality at* $Q^2 = m_W{}^2$,
Phys. Lett. 185B (1987) 233.

[8] C. Albajar et al. (UA1 collaboration), *Search for new heavy quarks at the CERN proton - antiproton collider,* Z. Phys. C37 (1988) 505.

[9] G. Arnison et al. (UA1 collaboration), Phys. Lett. 122B (1983) 103.

[10] G. Arnison et al. (UA1 collaboration), Phys. Lett. 134B (1984) 469.

[11] G. Arnison et al. (UA1 collaboration), Phys. Letts. 139B, 115(1984)

[12] C. Albajar et al. (UA1 collaboration), *events with large missing transverse energy at the CERN collider : search for the decays of* W^+ *into heavy leptons and of* Z^0 *into non-interacting particles,* Phys. Lett. 185B (1987) 24.

[13] C. Albajar et al. (UA1 collaboration), *events with large missing transverse energy at the CERN collider : mass limits on supersymmetric particles ,*
Phys. Lett. 198B (1987) 261.

[14] See for example, F. Halzen and A. Martin, *Quarks and leptons* , (John Wiley and sons inc.).
C. Quigg, *Gauge theories of the strong, weak and electromagnetic interactions* , (Benjamin/Cummings, Reading, Massachusetts, 1983).
L. Okun, *Leptons and quarks,* (North Holland, Amsterdam, 1981).

[15] P. A. M. Dirac, *The quantum theory of the electron,* Proc. Roy. Soc. A117 (1928) 160.

[16] Original papers by these authors can be found in, *Selected papers on quantum electrodynamics,* Edited by J. Schwinger (Dover publications, New York, 1958).

[17] E. P. Wigner, *Group theory,* (Academic press, New York, 1959).

[18] M. Gell-Mann and Y. Ne'eman, *The eightfold way,* (Benjamin, New York, 1964).

[19] M. Gell-Mann , *A schematic model of baryons and mesons,* Phys. Lett. 8, (1964) 214,
G. Zweig, *An SU(3) model for strong interaction symmetry and its breaking,* CERN preprint 8409/Th. 412, (1964) (unpublished).
G. Zweig, *Symmetries in elementary particle physics,* Edited by A. Zichichi (Academic press, New York, 1965).

[20] S. L. Glashow, *Partial symmetries of weak interactions,* Nucl. Phys. 22 (1961) 579.
S. Weinberg, *A model of leptons,* Phys. Rev. Lett. 19 (1967) 1264.
A. Salam and J. C. Ward, *Electromagnetic and weak interactions,* Phys. Lett. 13 (1964) 168.

[21] J. Blietscham et al., *Determination of the neutral to charged current inclusive cross-section ratio for neutrino and antineutrino interactions in the Gargamelle experiment,* Nucl. Phys. B118 (1976) 218.
C. Y. Prescott et al., *Parity non-conservation in inclusive electron scattering,* Phys. Lett. 77B (1978) 347.
See also [2] and [3].
P. Bagnaia et al., *Evidence of* $Z^0 \rightarrow e^+ e^-$ *at the CERN PP collider,* Phys. Lett. 129B (1983) 130.
M. Banner et al., *Observation of single isolated electrons of high transverse momentum in events with missing transverse energy at the CERN PP collider,* Phys. Lett. 122B (1983) 476.

[22] Y. A. Golfond and E. P. Likhtman, *Extension of the algebra of Poincare group generators and violation of P invariance ,* JETP Letters 13 (1971) 323.

[23] D. V. Volkov and V. P. Akulov, *Is the neutrino a Goldstone particle,* Phys. Lett. 46B (1973) 109.

[24] J. Wess and B. Zumino, *A lagrangian model invariant under supergauge transformations,* Phys. Lett. 49B (1974) 52

[25] F. Fayet, *Higgs model and supersymmetry,* Il Nuovo Cimento, Vol 31A, 4 (1976) 626.

[26] R. Nath, R. Arnowitt and A. Chamseddine, *Applied N=1 supergravity ,* ICPT series in Theor. Physics (World Scientific, Singapore, 1984), Vol1.
H. Haber, G. L. Kane, *The search for supersymmetry : probing physics beyond the Standard Model,* Phys. Rep. 117 (1985) 75.

[27] D. Nitz et al., Univ. of Michigan preprint UM HE 86-16 (1986).

[28] J. Ellis et al., Nucl. Phys. B238 (1984) 453.

[29] C. Rubbia, P. McIntyre and D. Cline, *Producing massive neutral intermediate vector bosons with existing accelerators,* in the proc. of the International Neutrino Conference, Aachen (1976) 683.

[30] UA1 Collaboration, *A 4Π solid angle detector for the SPS used as a proton - antiproton collider at centre of mass energy of 540 Gev,* CERN/SPSC/ 78-06 (1978).

[31] M. Banner et al. (UA2 Collaboration), *proposal to study proton - antiproton interactions at 540 Gev CM energy,* CERN/SPSC/ 78-08 (1978).
B. Aubert et al. (UA3 Collaboration), *Search for magnetic monopoles,* CERN/SPSC/ 78-15 (1978).
M. Battiston et al. (UA4 collaboration), *The measurement of elastic scattering and of the total cross section at the CERN PP collider,* CERN/SPSC/ 78-105 (1978).
M. G. Albrow et al. (UA5 collaboration), *An investigation of proton - antiproton events at 540 Gev CM energy with a streamer chamber detection system,* CERN/SPSC/ 78-70 (1978).

[32] M. Barranco laque et al., *The construction of the central detector for an experiment at the CERN PP collider,* NIM 176 (1980) 175.

[33] F. Sauli, *Principles of operation of multiwire proportional and drift chambers,* CERN 77-09 (1977).

[34] C. Cochet et al., *The central electromagnetic Calorimetry in UA1,* NIM A243 (1986) 45.

[35] B. Aubert et al., NIM 176 (1980) 195.

[36] M. J. Corden et al., Physica Scripta 25 (1982), 11.
M. J. Corden et al., Physica Scripta 25 (1982), 5.
M. J. Corden et al., Rutherford Appleton Lab. Report RAL-83-116 (1983).

[37] K. Eggert et al., *Large area drift chambers for a muon detector at the PP collider,* NIM 176 (1980) 217.

[38] A. Astbury et al., Rutherford Appleton Lab. Report RAL-84-025 (1984).
H. Lehmann and H. Reithler, UA1/TN 81-20 (1981).
G. Hilgers et al., UA1/TN 81-22 (1981).

[39] R. Bock, E. Pagiola and J. Zoll, *HYDRA systems manual,* CERN publications, (1 march 1972).

[40] G. Arnison et al. (UA1 Collaboration), Nuovo Cimento Lett. 44 (1985) 1.

[41] T. P. Shah and K. Sumorok, UA1/TN 83-55 (1983).

[42] F. Page and S. Protopopescu, *ISAJET 5.20 : A Monte Carlo generator for PP and PP interactions,* BNL 38034 (1986).

[43] M. Corden et al., UA1/TN 83-62 (1983).
F. Bernasconi et al., UA1/TN 83-86 (1983).
F. Bernasconi et al., UA1/TN 85-06 (1985).
A. Honma et al., UA1/TN 85-10 (1985).
C. Albajar et al., UA1/TN 86-31 (1986).

[44] W. Ruckstuhl et al., Phys. Rev. Lett. 56 (1986) 2132.
G. Matteazzi et al., Phys. Rev. Lett. 52 (1984) 1869.
I. Beltrami et al., Phys. Rev. Lett. 54 (1985) .
W. W. Ash et al., Phys. Rev. Lett. 556 (1985) 2118.

[45] C. Albajar et al. (UA1 Collaboration), *Production of W's with a large Transverse momentum at the CERN proton - antiproton collider,* Phys. Lett. 193B (1987) 389.

[46] UA1/TN 86-26 (1986).
UA1/TN 86-45 (1986).
UA1/TN 86-69 (1986).
UA1/TN 86-79 (1986).

[47] G. Altarelli et al., Z. Phys. C27 (1985) 617.
G. Alterelli et al., Nucl. Phys. B246 (1984) 12.

[48] S. Dawson, E. Eichten and C. Quigg, *Search for supersymmetric particles in hadron-hadron collisions,* Phys. Rev. D31 (1985) 1581.
J. Ellis and H. Kowalski, Nucl. Phys. B259 (1985) 109.
E. Reya and D. Roy, Phys. Lett. 116B (1986) 223.

[49] M. Green and J. Schwartz, Phys. Lett. 149B (1984) 117.

[50] P Candelas, H. Horowitz, A. Strominger and E. Witten, Nucl. Phys. B258 (1985) 46.
E. Witten, ibid. B258 (1985) 75.

[51] Chamseddine, Arnowitt and Nath, Phys. Rev. Lett. 49 (1982) 970.
S. Weinberg, Phys. Rev. Lett. 50 (1983) 387.

[52] H. Baer, K. Hagiwara and X. Tata, *Gauginos as a signal for supersymmetry at* $P\bar{P}$ *colliders,* Phys. Rev. D35 (1987) 1598.

[53] V. Barger, R. W. Robnitt, W. y. Keung and R. J. N. Phillips, *Supersymmetric decay widths of weak bosons,* Phys. Rev. D28 (1983) 2912.

[54] R. Barnett, H. Haber and G. Kane, Nucl. Phys. B267 (1986) 625.

[55] B. Naroska, Phys. Rep. 148 (1987) 67.
H. I. Bererd et al., DESY preprint 87-013 (1987).

[56] A. Cooper-Sarker et al., Phys. Lett. 166B (1985) 212.

[57] Dawson, Eichten and Quigg in ref [48].

[58] M. Mohammadi , *Search for decays of* W^+ *into fourth generation leptons,* Univ. of Wisconsin Thesis (1987).